BORNEO SCIENCE
THE JOURNAL OF SCIENCE & TECHNOLOGY

EDITORIAL BOARD

Journal homepage: https://jurcon.ums.edu.my/ojums/index.php/borneo-science

Borneo Science is a biannual, peer-reviewed scholarly journal that publishes original research and review articles across all disciplines of science and technology. Established in 1995, the journal functions as an interdisciplinary platform for the dissemination of rigorously conducted scientific research of regional and global relevance.
The journal prioritizes, but is not limited to, the following subject areas: *Earth and Planetary Sciences; Chemical, Physical and Materials Sciences; Mathematical Sciences; Agriculture and Biological Sciences; and Environmental Sciences.*

Borneo Science is committed to upholding the highest standards of academic integrity, transparency, and ethical publishing. The journal provides an international forum for researchers to communicate valid and original findings, encouraging critical inquiry and scholarly debate that contribute meaningfully to scientific advancement.

VOLUME 47, ISSUE 1 (MARCH 2026)

BORNEO SCIENCE
THE JOURNAL OF SCIENCE & TECHNOLOGY

Journal homepage: https://jurcon.ums.edu.my/ojums/index.php/borneo-science

CONTENT
KANDUNGAN

RESEARCH ARTICLE

BORNEO SCIENCE
THE JOURNAL OF SCIENCE & TECHNOLOGY

Journal homepage: https://jurcon.ums.edu.my/ojums/index.php/borneo-science

STUDENTS' LEARNING PERFORMANCE EVALUATION USING FUZZY LOGIC

Suriana Lasaraiya*[1] and Suzelawati Zenian[2]

[1] Preparatory Centre for Science and Technology, Universiti Malaysia Sabah, UMS, Malaysia.
[2] Faculty of Science and Technology, Universiti Malaysia Sabah, UMS, Malaysia.

***Correspondence:**
suriana@ums.edu.my

Received: 5 May 2025
Revised: 29 December 2025
Accepted: 29 December 2025
Published online:
1 March 2026

Doi:
10.51200/bsj.v47i1.6353

Keywords:
Fuzzy inference; fuzzy logic; fuzzy number; fuzzy rules; triangular membership function

ABSTRACT. *In Malaysia, students' performance at school, foundation, and university levels is traditionally assessed using a classical evaluation method, which aggregates scores from various assessments, such as assignments and exams, and assigns grades based on predefined thresholds (e.g., A, A-, B+, B). This study evaluates the mathematics performance of foundation students using a fuzzy logic approach and compares it with the conventional classical grading method. A Mamdani-type fuzzy inference system was developed using three input variables, that is, assignment, midterm, and final examination scores, and one output variable, namely students' performance grade. All variables were modeled using triangular membership functions, and a total of 12 fuzzy if-then rules were constructed based on common academic grading practices. The centroid defuzzification method was applied to obtain crisp performance scores. The proposed model was tested using data from 49 foundation students at the Preparatory Centre for Science and Technology, Universiti Malaysia Sabah. The results indicate that while extreme performances remain consistent across both methods, the fuzzy logic approach provides a more nuanced evaluation for borderline cases, leading to differences in grade classification for several students. These findings suggest that fuzzy logic offers a more flexible and informative alternative to classical grading systems in educational assessment. This study aims to analyze the differences between the classical and fuzzy logic methods, highlighting the potential benefits or limitations of adopting fuzzy logic in educational assessments.*

INTRODUCTION

Enhancing students' learning performance is a fundamental objective in educational systems. To achieve this, a fair and comprehensive evaluation system is essential to ensure all students receive equitable assessments. Traditionally, educational performance is measured numerically based on examination grades. The most common method involves summing the total marks from various assessments, including assignments, midterm exams, and final exams, to determine students' grades. However, this classical approach often relies on rigid scoring criteria, which may not accurately reflect students' true abilities and learning progress.

The fuzzy evaluation method in fuzzy logic has been shown to be effective for assessing student academic performance, as highlighted by Biswas (1995), Chang and Sun (1993), and Law (1996). Their research demonstrated that the fuzzy logic approach offers several advantages over traditional evaluation methods. Semerci (2004) introduced an experimental method utilizing fuzzy logic to explore its impact on student achievement. This study laid the groundwork for understanding how fuzzy logic could influence educational outcomes. Building on this, Saleh and Kim (2009) proposed a method for evaluating student performance using fuzzy logic. Their approach involved fuzzification and defuzzification processes based on the difficulty, importance, and complexity of questions, which proved to be straightforward and yielded fair and accurate results.

Gokmen *et al*. (2010) found that fuzzy logic assessment effectively classified students' learning groups by adapting to their individual characteristics and real-time performance. It was as accurate as the traditional t-score method, making it a viable alternative for educational evaluations. Sripan and Suksawat (2010) propose a study on students' learning assessment by fuzzy logic. Their study concludes that fuzzy logic provides a strong framework for personalized student assessment in computer disciplines, improving educational outcomes by accommodating diverse learning styles and enabling tailored instructional strategies. Petrudi *et al*. (2013) also introduced a new performance evaluation method using fuzzy logic systems. In this study, they consider three aspects of an academic course: exam 1, theoretical exam 2, and practical exam 3. The results indicated that the fuzzy logic method could effectively evaluate students' learning levels in real-time, outperforming the t-score method in terms of accuracy and consistency.

Meanwhile, Yadav *et al*. (2014) introduce a new fuzzy expert system for evaluating students' academic performance using fuzzy logic techniques. Unlike the rigid classical method, the proposed system offers greater flexibility and reliability. Their comparison of the classical method with Fuzzy-1, Fuzzy-2, and the proposed system shows that the new fuzzy expert system is more effective for assessing student performance. Patel *et al*. (2014) developed a fuzzy logic-based expert system that assists the process of decision-making of students' performance evaluation within a data grid environment. Barlybayev *et al.* (2016) describe a technology for online training and assessment that focuses on qualitatively evaluating student competence without relying on formulas for calculating performance. Electronic university tutors assign grades and maintain records, providing an easy way to calculate students' average progress. It emphasizes the importance of considering the type and value of assessments and their overall impact on performance.

Lee *et al.* (2019) propose using a fuzzy modelling approach to consider these performance predictors and predict student performance at the start of a semester. Early predictions enable adjustments and interventions in course design to achieve the desired learning outcomes. Wen and Liu (2021) offer a more transparent and equitable approach to assessing student performance. It enhances the current system by providing a clearer analysis of how students' scores relate directly to the attributes of each question. This method helps to better reflect the intended teaching design and objectives behind each question. Tengku Petra and Ab. Aziz (2021) proposes a fuzzy expert system that significantly aids in investigating and analyzing student performance. Their study demonstrates the flexibility of fuzzy logic, highlighting its ability to assign different weightages to attributes based on the specific needs and requirements of educational institutions. Additionally, the system allows for further refinement of fuzzy rules and membership functions to optimize the results of fuzzy controllers. Dokare *et al.* (2021) showed the difference between the traditional approach and the inference in assessing the student's performance. Fuzzy logic facilitates the creation of systems with complex, human-like logical abilities. It can handle data representing subjective or ambiguous human thoughts, allowing computers to process information that is neither entirely true nor false, akin to human thinking. This model can thus be employed to improve evaluation systems in educational institutions, enabling better tracking of performance and monitoring of individual growth over time.

Kumar and Singh (2023) modelled students' performance using fuzzy logic. However, in this study, they are comparing the results obtained while using type-I fuzzy and type-2 fuzzy in the model. Jan *et al.* (2023) focus on using the artificial intelligence (AI) technique of fuzzy logic to develop a student monitoring system based on the Outcome-Based Education (OBE) system for quality education. We identified three key factors from the literature: direct assessment, indirect assessment, and stress. Stress has been added as an additional factor to gain more insight into student monitoring. This approach highlights student stress and aims to provide a comprehensive view of academic performance. The latest study was done by Loan *et al.* (2024). In this study, they employ a combination of fuzzy logic and hierarchical linear regression to analyze students' performance. The findings in this study revealed the following: 1) There are differences in students' performance between traditional and fuzzy evaluation methods; 2) The learning method has an impact on students' fuzzy grades; 3) Students studying online do not perform better than those studying onsite. In this paper, a fuzzy logic approach is employed to assess students' performance in Mathematics, focusing on scoring and grading. The evaluation utilizes three key input variables: scores from assignments, midterm exams, and final exams. A total of 12 fuzzy rules are established to implement the fuzzy logic model.

Although numerous studies have applied fuzzy logic to student performance evaluation, many focus primarily on proposing fuzzy models without clearly detailing their inference structure, rule justification, or membership function parameters. Furthermore, limited studies provide a direct comparison using real foundation-level mathematics data while explicitly addressing borderline grading issues inherent in classical assessment methods. This creates a gap in terms of transparent methodological reporting and practical implementation in foundation mathematics courses.

Therefore, the objectives of this study are to develop a Mamdani fuzzy inference system for evaluating foundation students' mathematics performance using assignment, midterm, and final examination scores, construct and justify a 12-rule fuzzy rule base using triangular membership functions and finally to compare the grades obtained using the classical grading method and the fuzzy logic approach, with particular emphasis on borderline performance cases. This study contributes by providing a fully specified fuzzy inference framework, including membership function definitions, rule justification, and defuzzification procedures, applied to real academic data at the foundation level.

MATERIALS AND METHODS

Fuzzy logic, introduced by Zadeh in 1975 through his work on fuzzy sets, offers a mathematical framework to express linguistic variables, vagueness, and uncertainty. Unlike traditional binary logic, fuzzy logic handles non-digital, continuous systems without crisp boundaries, making it effective for representing knowledge and human reasoning. This approach uses variables such as "Low," "High," and "Normal" to capture degrees of truth, rather than simple "Yes/No" or "True/False" values. Data within fuzzy sets are represented by membership functions, where the degree of belongingness to a set is expressed as a value between 0 and 1. A higher membership value indicates a stronger association with a particular set, as described by Timothy (2004) and Zimmermann (2001).

This research focuses on the fuzzy inference system (FIS), a common application of fuzzy logic and set theory. FIS is a rule-based system that utilizes if-then rules, which are derived from human knowledge and experience, to process linguistic variables like "poor," "average," and "good." These rules enable FIS to handle vague systems effectively. Sen & Cenkci (2009) note that fuzzy sets can be characterized by various membership functions; in this study, we use a triangular membership fuzzy number $\mu = (\gamma, \alpha, \beta)$ with $\alpha > 0$ and $\beta > 0$, as illustrated by Zadeh (1965) in Equation 1.

$$\mu_\mu(x) = \begin{cases} \dfrac{x-\gamma}{\alpha} + 1, & \gamma - \alpha \le x \le \gamma \\ \dfrac{\gamma - x}{\beta} + 1, & \gamma \le x \le \gamma + \beta \\ 0, & \text{otherwise} \end{cases} \tag{1}$$

The model follows five main stages,

1. Data Collection:
   Gather raw scores from assignments, midterm exams, and final exams.

2. Fuzzification:
   The fuzzification of students' scores was performed by incorporating input variables and their corresponding membership functions into fuzzy sets. In this study, the input variables consist of assignment scores, midterm exam scores, and final exam scores, while the output variable represents the students' performance grade. Both input and output variables are modelled using triangular membership functions as shown in Figures 1, 2, 3, and 4.

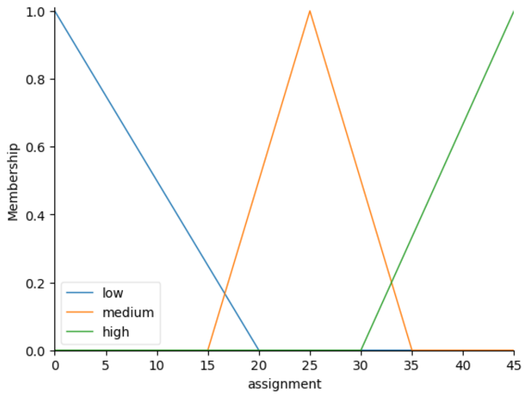

Figure 1. Membership function of the input variable for the assignment.

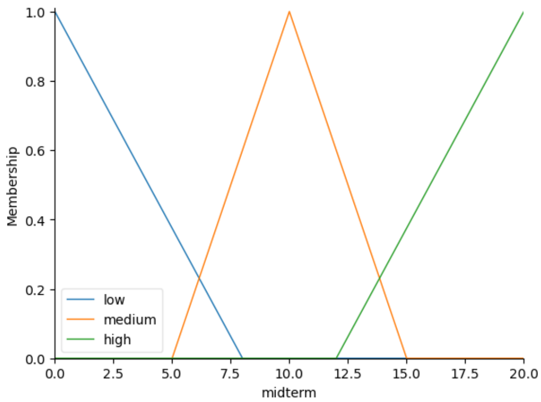

Figure 2. Membership function of the input variable for the midterm.

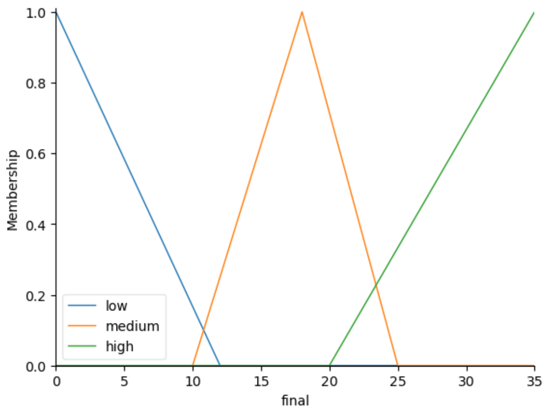

Figure 3. Membership function of the input variable for the final term.

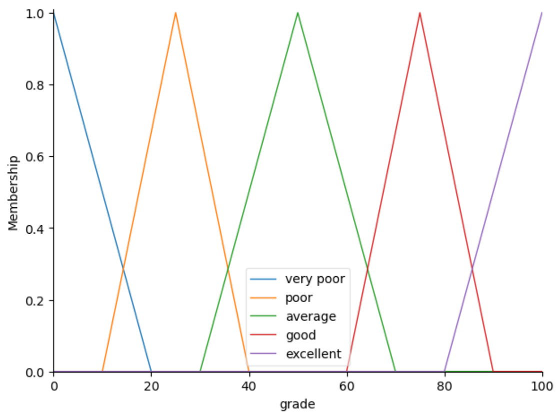

Figure 4. Membership function of output variables for student performance grades.

3. Rule Application:
   The fuzzy inference system was constructed by defining a set of rules that govern how the input variables (Assignment, Midterm, Final Term) combine to produce an output (Final Grade). A total of 12 rules were defined, capturing all possible combinations of inputs across the three linguistic terms. The rules were designed to reflect common grading practices, ensuring that students with consistently low scores received lower grades, while those with higher scores were rewarded accordingly. These rules, known as If-Then rules, are based on the works of Altrock (1995) and Semerci (2004). These rules were carefully designed to account for different performance scenarios, ensuring that the grading system was fair and accurate. Although three input variables with three linguistic terms each could theoretically produce 27 rules, this study adopts 12 dominant rules to

represent realistic and pedagogically meaningful grading scenarios. Redundant and impractical combinations, such as simultaneously high assignment performance with consistently poor examination results, were excluded. The selected rules focus on dominant performance patterns commonly observed in foundation-level mathematics assessments, thereby improving interpretability while maintaining adequate decision coverage.

4. Defuzzification:
Transform the fuzzy output into a crisp performance value. The membership interval is shown in Table 1. The defuzzification process was carried out using the centroid method, which is the most widely used method in fuzzy systems due to its effectiveness in capturing the center of the area under the curve. This method provided a crisp output that represented the final grade for each student. The crisp value is obtained and calculated as Equation 2.

$$z^* = \frac{\int \mu_c(z) \times z \times dz}{\mu_c(z) \times dz} \tag{2}$$

Table 1: The if-then rules assign for the input variables.

Output Variables	Input Variables		
	Assignment	**Midterm**	**Final term**
Very Poor (VP)	Low	Low	Low
Poor (Po)	Low	Low	Medium
Average (Av)	Medium	Medium	Medium
	High	Medium	Medium
	High	Medium	Low
	High	Low	Low
	High	Low	Medium
Good (Go)	High	Medium	Medium
	High	Medium	High
	High	High	Medium
	High	Low	Medium
Excellent (Ex)	High	High	High

Source: (If-then Rules as in Altrock (1995) and Semerci (2004))

5. Comparison and Analysis:
Compare the fuzzy logic results with traditional grading methods and analyze the differences.

Table 2. Output variables in the fuzzy logic system according to the membership function (Performance)

Linguistic Expression	Symbol	Interval
Very Poor	VP	[0, 0, 20]
Poor	Po	[10, 25, 40]
Average	Av	[30, 50, 70]
Good	Go	[60, 75, 90]
Excellent	Ex	[80, 100, 100]

RESULTS AND DISCUSSION

Table 3 presents the scores obtained by 49 foundation students in three key assessments: the assignment, midterm examination, and final term examination. Additionally, the table includes the final marks each student achieved, along with their corresponding grades. This comprehensive data provides a clear overview of the students' performance across different evaluation components, offering insight into their overall academic achievements for the semester. To validate the fuzzy logic system, the grades obtained through the fuzzy logic method were compared with those derived from the classical grading system.

In classical students' evaluation performance, the grading relies on a fixed threshold for assigning grades. For example, if a student's total score is 65, they may get a "B," while a score of 64 could result in a "B-," even though the difference in their performance is very minimal. In this case, sometimes the students on the borderline between two grades are not captured. Meanwhile, in fuzzy logic, this system evaluates students' performance better by considering the degree of membership to the different grade categories, where, in this case, for example, excellent, good, average, poor, and very poor. For example, a student with a score of 65 might have a grade "B" but with more nuanced reflection of their performance (e.g., 60.6), where this student might be closer to "B-".

Table 3. The input variables and the grade comparison by the classic method and fuzzy logic.

Student	Input variables			Grade comparison		Student	Input variables			Grade comparison	
	A	M	F	C	Fu		A	M	F	C	Fu
Stud 1	40.5	13.7	14.5	B	B-	Stud 26	40.5	11.7	17.5	B+	B-
Stud 2	41.1	8.0	15.5	B	B-	Stud 27	41.0	10.7	28.5	A	A-
Stud 3	40.8	6.8	12.5	B-	B-	Stud 28	40.6	11.0	15.5	B	B-
Stud 4	39.6	3.7	9.5	C	C	Stud 29	41.0	10.0	13.5	B	B-
Stud 5	40.5	10.0	27.5	A-	A-	Stud 30	40.6	8.3	20.0	B	B-
Stud 6	40.8	19.3	28.0	A	A-	Stud 31	37.2	4.3	4.0	C-	C
Stud 7	40.5	3.7	10.5	C+	C+	Stud 32	37.2	16.3	20.5	A-	A-
Stud 8	41.1	11.3	14.5	B	B-	Stud 33	41.0	13.3	30.0	A	A-
Stud 9	41.5	16.3	20.0	A-	A-	Stud 34	41.0	5.3	19.5	B	B-
Stud 10	39.6	10.3	12.5	B-	B-	Stud 35	41.1	6.3	16.5	B-	B-
Stud 11	39.1	5.3	5.0	C	C	Stud 36	40.8	4.3	15.0	B-	B-
Stud 12	41.5	3.7	5.0	C	C	Stud 37	41.0	5.0	1.5	C-	C
Stud 13	39.6	9.0	12.5	B-	B-	Stud 38	40.5	13.7	21.0	A-	B-
Stud 14	40.6	4.0	8.5	C	C	Stud 39	37.2	5.3	4.5	C-	C
Stud 15	41.5	9.3	14.0	B	B-	Stud 40	41.1	8.3	14.0	B-	B-
Stud 16	39.6	12.7	25.0	A-	A-	Stud 41	40.5	2.0	5.5	C-	C
Stud 17	40.8	6.0	2.0	C-	C	Stud 42	40.6	11.0	23.5	A-	B-
Stud 18	41.0	6.8	5.5	C	C	Stud 43	37.2	7.7	10.0	C+	C
Stud 19	40.5	8.3	9.5	C+	C	Stud 44	40.5	7.7	9.5	C+	C
Stud 20	40.6	15.3	20.0	A-	A-	Stud 45	40.6	10.0	15.5	B	B-
Stud 21	40.5	18.0	26.5	A	A	Stud 46	41.5	13.7	21.0	A-	B-
Stud 22	40.5	4.0	10.5	C+	C+	Stud 47	39.6	1.0	3.5	C-	C
Stud 23	40.8	13.0	20.0	B+	B-	Stud 48	40.5	6.0	18.5	B	B-
Stud 24	37.2	7.7	7.0	C	C	Stud 49	41.5	6.8	10.0	C+	C
Stud 25	37.2	8.3	26.0	B+	A-						

Source: Mathematics Course File, Semester 2, Session 2023/2024.
(Stud – Student; A - Assignment ; F – Final Term ; C – Classical ; Fu – Fuzzy Logic)

Evaluation using fuzzy logic shows the potential benefit in the student assessment as it provides a more flexible evaluation, especially for those marks that are close to the grade boundary. For example, in Table 3, Student 16 or Student 23 obtained a more accurate reflection of their performance under the fuzzy grading system. This is good in capturing small differences in student performance that are not noticed in the classical way. In addition, with fuzzy logic, students who might narrowly miss a grade cutoff in the classical system, such as Student 17 (C in classical, C in fuzzy), receive grades that more accurately reflect their capabilities without the harsh consequences of a cutoff. By avoiding sudden shifts in grades, fuzzy logic reduces the instances where students feel unfairly rewarded or penalized based on slight differences in their scores. Besides that, the fuzzy logic approach evaluates student performance based on degrees of membership across multiple grade categories (Very Poor, Poor, Average, Good, and Excellent), rather than relying on fixed cut-off values. This allows borderline cases to be assessed more gradually, avoiding abrupt grade transitions. As observed in Table 3, several students experienced grade adjustments under the fuzzy logic system, particularly those whose scores were close to conventional grade boundaries. This indicates that the fuzzy approach is more sensitive to small variations in performance that are not captured by the classical grading method.

The results further show that students with consistently high or consistently low performance generally retained the same grades under both evaluation methods. For example, students such as Student 6 (high performance) and Student 47 (low performance) received identical grades using both classical and fuzzy evaluations. This suggests that the impact of the fuzzy logic approach is more pronounced for borderline and mid-range performances, while extreme cases remain largely unaffected. Overall, these findings demonstrate that fuzzy logic provides a more flexible and informative assessment framework by reducing sudden grade changes and offering smoother transitions between grade categories. However, one limitation of this approach is the increased complexity in interpreting fuzzy output values, which may be less intuitive for educators and students accustomed to traditional letter grades. Therefore, appropriate guidelines or conversion schemes may be required to support the practical implementation of fuzzy-based grading systems.

However, there are a few limitations that need to be considered as well. For example, the grade obtained by Student 6 is A in both classical and fuzzy. The example is shown by Student 47, whose grade is C- in both classical and fuzzy as well. This shows that fuzzy logic might have less impact on the students' marks with extreme scores. Besides that, adopting fuzzy logic is the potential complexity in interpreting the results. Unlike the clear-cut "A," "B," or "C" grades in the classical system, fuzzy grades (e.g., 60.5) might seem less intuitive for students and educators accustomed to discrete letter grades. There may need to be a guideline to help interpret these nuanced scores.

CONCLUSION

This study's comparison of the classical grading method with fuzzy logic revealed that fuzzy logic offers a more nuanced and flexible evaluation of student performance. Unlike the classical method, which relies on fixed cutoffs and may overlook subtle differences in student capabilities, the fuzzy logic approach accounts for the degree to which students meet each performance criterion. While fuzzy logic can enhance fairness and accuracy, it may require additional support and understanding from educators and students to fully realize its benefits. This results in a more detailed and accurate reflection of their abilities. The fuzzy logic system's ability to handle uncertainties and subjective assessments makes it a valuable alternative in educational settings. The findings suggest that adopting fuzzy logic in educational assessments could enhance the accuracy of performance evaluations, though further research may be needed to address potential challenges in its implementation. While this study does not introduce a new fuzzy algorithm, it provides a transparent and fully specified implementation of a Mamdani fuzzy inference system for foundation-level mathematics assessment, supported by real institutional data.

ACKNOWLEDGEMENT

The authors gratefully acknowledge the support provided by the Preparatory Centre for Science and Technology (PPST), Universiti Malaysia Sabah, throughout this study.

REFERENCES

Zadeh, L.A. 1975. *The Concept of a Linguistic Variable and Its Application to Approximate Reasoning-III*. Information Sciences, 9(1): 43–80.

Biswas, R. 1995. An application of fuzzy sets in students' evaluation. *Fuzzy Sets and Systems*, 74(2): 187-194.

Altrock, V.C. 1995. Fuzzy Logic Application in Europe, In J. Yen, R. Langari, & L. A. Zadeh (Eds). *Industrial Applications of Fuzzy Logics and Intelligent Systems*, Chicago: IEEE Press

Chang, D.F. & Sun, C.M. 1993. Fuzzy assessment of learning performances of junior high school students. *In Proceedings of the 1993 1st National Symposium on Fuzzy Theory and Applications*, 1-10.

Law, C.K. 1996. Using fuzzy numbers in educational grading system. *Fuzzy Sets and Systems*, 83(3), 311-323.

Zimmermann, H.J. 2001. *Fuzzy Set Theory and Its Applications*. London. Kluwer Academic Publisher.

Semerci, C. 2004. The influence of fuzzy logic theory on students' achievement. *The Turkish Online Journal of Educational Technology TOJET*, 3(2:9): 56-61.

Timothy, J.R. 2004. *Fuzzy Logic with Engineering Applications*. Chichester, West Sussex. UK: McGraw-Hill, Inc.

Saleh, I. & Kim, S.I. 2009. A fuzzy system for evaluationg students' learning achievement. *Journal of Expert Systems with Application*, 36: 6236-6243.

Sen, C.G. & Cenkci, D. 2009. An integrated approach to determination and evaluation of production planning performance criteria. *Journal of Engineering and Natural Science*, 27: 4-5.

Gokmen, G., Akinci, T.C., Tektas, M., Onat, N., Kocyigit, G. & Tektas, N. 2010. Evaluation of students performances in laboratory applications using fuzzy logic. *Procedia Social and Behavioral Science* 2: 902-209.

Sripan, R. & Suksawat, B. 2010. Propose of fuzzy logic-based students' learning assessment. *International Conference on Control, Automation and Systems*. 414-417.

Petrudi, S.H.J., Pirouz, M. & Pirouz, B. 2013. Application of fuzzy logic for performance evaluation of academic students. *13th Iranian Conference on Fuzzy Systems (IFSC).*

Yadav, R.S., Soni, A.K. & Pal, S. 2014. A study of academic performances evaluation using fuzzy logic techniques. *International Conference on "Computing for Sustainable Global Development*, 54-59.

Patel, S., Sajja, P. & Patel, A. 2014. Fuzzy logic-based expert system for students' performance evaluation in data grid environment. *International Journal of Scientific & Engineering Research*, 5(1): 36-40.

Barlybayev, A., Sharipbay, A., Ulyukova, G., Sabyrov, T., & Kuzenbayev, B. 2016. Students' Performance by Fuzzy Logic. *Procedia Computer Science,* 102, 98-105.

Lee, S.H., The, C.S. & Barawi, M.H. 2019. Predicting students' course performance based on learners' characteristics via fuzzy modelling approach. *International Advanced Science Engineering Information Technology*, 9(6): 1944-1949.

Wen, S. & Liu, D. 2021. Students' learning performance evaluation using a new fuzzy inference system. *2nd International Conference on Artificial Intelligence and Education*, 650-656.

Tg. Petra, T.Z. & Ab. Aziz, M.J. 2021. Analysing Student performance in higher education using fuzzy logic evaluation. *International Journal of Scientific & Technology Research*, 10(1): 322-327.

Dhokare, M., Teje, S., Jambukar, S. & Wangikar, V. 2021. Evaluation of academic performance of students using fuzzy logic. 978-982.

Kumar, P. & Singh, G. 2023. Modelling student's performance evaluation using fuzzy logic techniques. *International Journal of Creative Research Thought (IJCRT),* 2320-2882.

Jan, N.U., Naqvi, S. & Ali, Q. 2023. Using fuzzy logic for monitoring students' academic performance in higher education. *Engineering Proceedings*. 46 (21) doi: https://doi.org/10.3390/engproc2023046021.

Loan, D.T.T., Tho, N.H., Nghia, N.N., Chien, V.D. & Tuan, T.A. 2024. Analyzing students' performance using fuzzy logic and hierarchical linear regression. *I.J. Modern Education and Computer Science,* 1: 1-10.

RESEARCH ARTICLE

BORNEO SCIENCE
THE JOURNAL OF SCIENCE & TECHNOLOGY

Journal homepage: https://jurcon.ums.edu.my/ojums/index.php/borneo-science

IMPACT OF SORGHUM GRAIN INCLUSION IN PELLET ON FEED INTAKE, GROWTH PERFORMANCE, AND BLOOD METABOLIC PROFILE OF MUSCOVY DUCKS

Rosesyaqirah Baiduri Abd Razak[1], Mohammad Mijanur Rahman[2*], Nurhanan Abdul Rahman[1], Md Safiul Alam Bhuiyan[2], and Mohamad Asrol Kalam[2]

[1]Faculty of Agro-Based Industry, Universiti Malaysia Kelantan, Jeli 17600, Kelantan, Malaysia.
[2]Livestock Production Programme, Faculty of Sustainable Agriculture, Universiti Malaysia Sabah, Mile 10, Sg. Batang, 90000, Sandakan, Sabah, Malaysia.

[*]Correspondence:
mijanur.r@ums.edu.my

Received: 8 August 2025
Revised: 6 January 2026
Accepted: 6 January 2026
Published online:
1 March 2026

Doi:
10.51200/bsj.v47i1.6693

Keywords:
Blood metabolic profile; Feed intake; Growth performance; Muscovy duck; *Sorghum bicolour*

ABSTRACT. *The rising cost and limited availability of conventional feed have driven the search for sustainable and economical alternatives. Sorghum grain (Sorghum bicolour), with a nutritive value comparable to maize, is considered a suitable substitute in poultry diets. This study evaluated the effects of sorghum grain inclusion in duck pellets on feed intake, growth performance, and blood profile. Thirty unsexed ducks, approximately 21 days old, were assigned to two groups: one fed sorghum-based pellets (treatment) and the other fed commercial pellets (control). Over six weeks, feed intake, growth, and blood parameters were assessed. Ducks fed the sorghum-enriched pellets showed significantly ($p<0.05$) better growth, with higher body weight (1298.0 vs. 953.3 g/bird) and daily weight gain (30.9 vs. 22.7 g/day/bird). They also had a lower, though not significant ($p>0.05$), feed conversion ratio (4.9 vs. 6.9). There were no significant differences and no adverse effects on blood biochemistry profiles. In conclusion, incorporating sorghum grain into duck pellets improves growth performance and positively influences blood profiles.*

INTRODUCTION

Poultry play a vital role in agriculture and food production, contributing significantly to sustainability. They are efficient converters of feed into meat or eggs and help recycle nutrients through soil, manure, and feed, supporting sustainable farming systems. Compared to ruminants, poultry emit minimal methane, a potent greenhouse gas, making their production relatively climate-friendly (Zisis *et al.*, 2023). This environmentally conscious aspect is enhanced by practices such as reducing fossil fuel use, improving feed production, and using poultry manure as crop fertiliser.

Feed type is a critical factor in sustainable poultry production. Conventional poultry diets primarily rely on grains and pulses, particularly maize and soybeans. However, sustainable agricultural practices like no-till farming, crop rotation, and cover cropping help sequester carbon in the soil. Moreover, innovative feeding strategies, such as using by-products like fruit pulp, cull crops, or insects reared on agricultural waste, enhance sustainability by promoting nutrient recycling (Ababor *et al.*, 2023).

Despite Malaysia's strong self-sufficiency in broiler and egg production, the country remains heavily dependent on imported feed ingredients, especially maize and soybean meal, making the poultry sector vulnerable to global supply disruptions and price fluctuations (Ashraf & Abd. Rahman, 2022; Jamaludin *et al.*, 2023). The recent surge in feed costs, exacerbated by events such as the COVID-19 pandemic, has further challenged the sustainability and profitability of poultry production (Elleby *et al.*, 2020). In response, researchers have turned to cultivating sorghum (*Sorghum bicolour*) domestically as an alternative to maize. Sorghum, a drought-resistant cereal crop in the Poaceae family, is adaptable to warm climates and shows high genetic and phenotypic diversity (Chakrabarty *et al.*, 2022; Kamal *et al.*, 2023). It is well-suited for Malaysia's climate and can be grown on marginal lands (Nazmi *et al.*, 2022). Low-tannin varieties now available reduce anti-nutritional effects and improve digestibility in poultry (Selle & Ravindran, 2007). Nutritionally, sorghum is similar to maize, rich in starch, protein, lipids, and phenolic compounds (Stefoska-Needham *et al.*, 2015). It also has potential uses in functional foods and bioethanol production (Szambelan *et al.*, 2020). This study evaluated the inclusion of sorghum grain in duck pellets and its effects on feed intake, growth performance, and blood biochemistry, offering insights into its viability as a sustainable and cost-effective feed alternative for the poultry industry.

MATERIALS AND METHODS

Study Site

The study was conducted at Pondok Al Jaafar in Gua Tempurung, 31600 Gopeng, Perak, Malaysia. The site experiences both wet and dry seasons, with mean temperatures ranging from a minimum of 23 °C to a maximum of 34 °C. The experimental animals used were locally sourced crossbred unsexed Muscovy ducks (*Cairina moschata*), approximately 7 days of age. The ducks were acclimatised to their new environment for 14 days and fed a commercial starter pellet diet appropriate for the early growth stage before the feeding trial began.

Ration Formulation

The diets were formulated using Winfeed 2.8 software (Table 1). The control diet consisted of commercial feed with maize and soybean meal as its primary ingredients. In the treatment diet, sorghum grain was substituted entirely for maize. All diets were balanced to meet the nutrient requirements of growing ducks (Hakem *et al.*, 2025). Starter and grower pellets contained more crude fibre compared to commercial pellets.

Table 1. Composition of experimental diets for ducks.

Ingredients	Commercial grower pellet⁺	Starter pellet (%)	Grower pellet (%)
Sorghum grain	-	43.1	45.0
Soybean meal	-	20.0	12.2
Fish meal	-	6.5	4.1
Rice bran	-	9.0	14.0
Palm kernel meal	-	7.3	10.8
Limestone	-	0.3	0.5
Salt	-	0.3	0.5
Palm oil	-	8.5	6.0
Molasses	-	4.0	5.5
Vitamin premix	-	0.5	0.7
Mineral premix	-	0.5	0.7
Nutritive value (%, dry matter basis)			
Dry matter	89.20	89.80	89.92
Crude protein	18.97	21.6	17.99
Crude fibre	5.68	8.07	8.67
Ether extract	1.12	4.49	4.18
Ash	5.46	4.97	5.27
Metabolisable energy (kcal/kg)*	2956	2923	2767

*calculated from secondary data (Yusoff *et al.,* 2005); ⁺, not given because of business privacy.

After sorghum grain was procured from a local supplier, it was ground using a hammer mill to achieve a uniform particle size suitable for pellet production. The ground sorghum was then mixed with other ingredients in an industrial mixer to ensure homogeneity, critical for providing balanced nutrition to the ducks. The feed mixture was pelletised using a pelletising machine, forming cylindrical pellets. These pellets were then dried in a dehydrator to reduce their moisture content, thereby enhancing their quality and shelf life. The prepared feed was stored in vacuum-sealed containers to maintain freshness. During pelletising, the temperature was maintained below 70 °C to minimise heat damage to heat-sensitive nutrients such as lysine and vitamins. Drying was carried out at 60 °C until the moisture content reached about 10 – 12%, ensuring nutrient preservation while maintaining pellet durability.

Experimental Design

All ducks were evenly distributed into two dietary groups. The control group consisted of 15 ducks (9 males and 6 females), while the treatment group consisted of 15 ducks (9 males and 6 females). Each group was divided into three replicates of five ducks per replicate (3 males and 2 females). The ducks were randomly allocated to the groups and replicates using a simple randomisation method, where each duck was assigned a number and grouped using a random number generator to avoid selection bias. The sample size (n = 30) was selected based on previous similar feeding trials involving Muscovy ducks, which demonstrated that a minimum of 10–15 birds per group provides sufficient statistical power to detect significant differences in growth and blood parameters (Marzoni *et al.*, 2005; Hakem *et al.*, 2025). This number also reflects practical and ethical considerations related to housing space, resource availability, and animal welfare. The trial lasted for six weeks, after which the ducks were slaughtered for further analysis.

The study employed a twice-daily feeding schedule at 8:00 am and 5:00 pm. The birds were fed their experimental diets on an *ad libitum* basis. Water was provided with free access. The control group of ducks was fed a commercial grower pellet diet throughout the study. The treatment group was fed a starter pellet for the first four weeks, followed by a grower pellet for the final two weeks. The feed and water troughs were thoroughly cleaned to prevent contamination.

Parameters Observed

Ducks were weighed weekly throughout the trial to monitor growth. Daily feed intake was determined by weighing the daily total feed offered and subtracting the leftover feed (dry matter basis). Daily feed and cumulative intakes were recorded. Temperature and humidity were also documented during the experimental period. Average daily weight gain (ADWG) and feed conversion ratio (FCR) were calculated using Equations 1 and 2.

$$\text{ADWG} = (\text{Total Weight}) / 7 \quad (1)$$

$$\text{FCR} = \frac{\text{Daily feed intake (g)}}{\text{Daily body weight gain (g)}} \quad (2)$$

Blood samples were collected during the slaughtering session at the end of the trial. The blood was immediately sent to Medi-Vance Healthcare, Ipoh, Malaysia, for biochemical analysis. Key parameters assessed included haemoglobin levels, red blood cell count, mean corpuscular haemoglobin, white blood cell (WBC) count (neutrophils, lymphocytes, monocytes, and eosinophils), and platelets. These markers provided insights into the ducks' overall health, immune response, and oxygen-carrying capacity. Reference ranges for duck haematological parameters, including WBCs (typically 10–30 × 10^9/L), were used to evaluate abnormalities in the results (Olayemi *et al.*, 2003).

Statistical Analysis

Data were analysed using one-way ANOVA with SPSS statistical software (version 23.0). Post hoc comparisons between treatment means were performed, and differences were considered statistically significant at $p < 0.05$. Results are reported as mean ± standard deviation.

RESULTS AND DISCUSSION

Feed Intake

The weekly feed intake of ducks fed experimental diets varied over the six weeks (Figure 1). In Week 1, the control group consumed significantly ($p<0.05$) more feed (813.3 g/duck) than the treatment group (724.7 g/duck). A similar trend was observed in Week 2, where the control group (838.3 g/duck) again consumed more than the treatment group (795.7 g/duck). In Week 3, feed intake remained significantly higher in the control group (1033 g/duck) than in the treatment group (982 g/duck). However, in Week 4, the treatment group (1049.3 g/duck) surpassed ($p<0.05$) the control group (1008 g/duck). In Weeks 5 and 6, intake differences were not statistically significant ($p>0.05$), with the treatment group slightly ahead. Overall, average feed intake across the six weeks was not significantly affected by the dietary treatment ($p>0.05$), indicating that inclusion of the experimental diet did not adversely affect voluntary feed intake in ducks. On average, the control group consumed 958.4 g/duck, while the treatment group consumed 937.6 g/duck, with no significant difference.

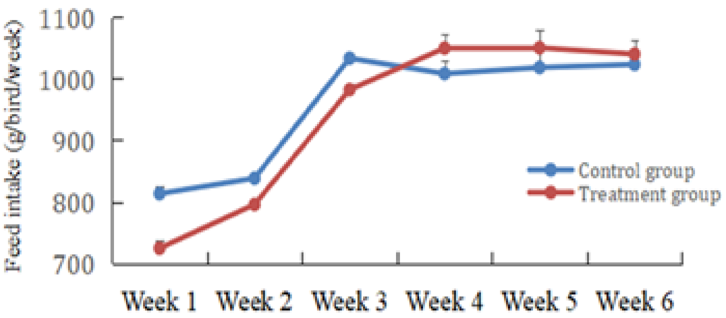

Figure 1. Weekly feed intake (g/bird/week) by ducks during the experimental period.

These results indicate notable variations in feed intake, particularly during the initial weeks. The higher early intake observed in the control group may be related to greater palatability and a more familiar nutrient profile, whereas the experimental diet may have initially reduced acceptance due to differences in flavor, texture, or nutrient composition, such as fiber and energy density. As the trial progressed, the treatment group gradually adapted and achieved comparable intake levels, suggesting improved palatability and physiological adjustment to the diet. This pattern is consistent with Arroyo *et al.* (2016), who highlighted the importance of early digestive and behavioral adaptation when novel feed ingredients are introduced. However, physical feed characteristics such as pellet durability and stability, which can further influence palatability and intake, were not evaluated and should be considered in future research.

Growth Performance

The growth performance data are presented in Table 2. Initial body weights were comparable between groups (control: 346.7 g/duck; treatment: 345.4 g/duck; $p>0.05$). This indicates a uniform starting condition across treatments. By Week 6, ducks fed the treatment diet achieved a significantly ($p<0.05$) higher final body weight (1643.3 g/duck) than those fed the control diet (1300.0 g/duck). Total weight gain and average daily gain were numerically higher in the treatment group (1298.0 g/duck and 30.9 g/day, respectively) than in the control group (953.3 g/duck and 22.7 g/day); however, these differences were not statistically significant (p>0.05). Feed conversion ratio (FCR) was numerically lower in the treatment group (4.9) compared with the control group (6.9), but the difference was not statistically significant (p = 0.144), indicating that the treatment diet did not significantly alter feed efficiency under the present experimental conditions.

Table 2. Growth performance of ducks fed experimental diets.

Parameter	**Control group**	**Treatment group**	***p* - value**
Initial body weight, g/bird	346.70 ± 88.51	345.40 ± 56.18	0.984
Final body weight, g/bird	1300.00 ± 166.67	1643.30 ± 128.97	0.048
Total body weight gain, g/bird	953.30 ± 236.39	1298.00 ± 82.83	0.076
Daily body weight gain, g/bird	22.70 ± 5.63	30.90 ± 1.97	0.076
Feed conversion ratio	6.90 ± 1.95	4.90 ± 0.32	0.144

Weekly Body Weight

Body weight increased steadily in both groups over six weeks (Figure 2). Week 1 weights were nearly identical. In Week 2, the treatment group (589.4 g/bird) tended to exceed the control (361.2 g/bird), but it was not found to be significantly (p>0.05) different. In Week 3, the control group recorded a slightly higher weight (587.1 g/bird). From Week 4 onwards, the treatment group consistently outperformed, culminating in a significantly (p=0.048) higher final weight in Week 6. These results align with overall growth trends, suggesting that ducks fed the treatment diet adapted over time and improved nutrient utilisation, as supported by Arroyo *et al.* (2016).

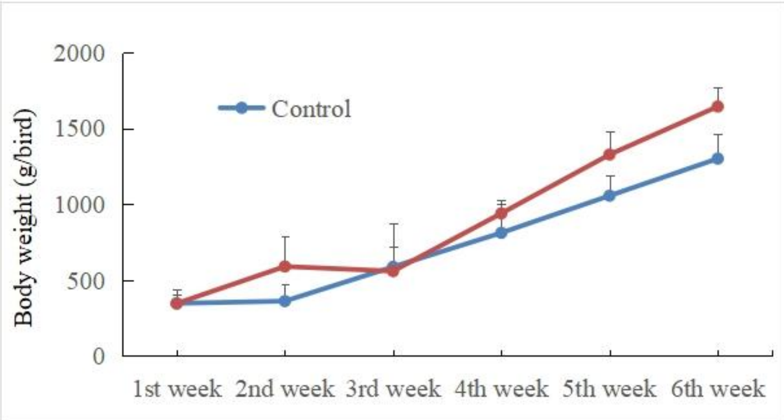

Figure 2. Weekly body weight of ducks fed experimental diets.

Blood Metabolic Profile

The blood metabolic profile (Table 3) revealed no statistically significant (p>0.05) differences between the control and treatment groups. Overall, the results indicate that the treatment diet did not alter blood metabolic profiles and did not exert any adverse physiological effects on the ducks. Although the treatment group showed slightly higher haemoglobin levels, red and white blood cell counts, neutrophils, and lymphocytes, these were not significant (p>0.05). Both groups had WBC counts above the reference range reported by Olayemi *et al.* (2003), which could reflect breed-specific traits, environmental factors, or subclinical responses unrelated to diet. Platelet counts were lower in the treatment group, though not significantly. These findings should be interpreted cautiously, as trends in immune-related values suggest a physiological response, but no definitive conclusions can be drawn. Despite minor numerical variations in some haematological parameters, all measured values remained within physiologically acceptable limits, indicating normal health status. Jerabek *et al.* (2018) similarly reported that dietary changes did not always impact blood biochemistry significantly. The elevated WBC count in the treatment group may indicate subclinical infection, individual variability, or breed-related differences. The high standard deviation in platelet counts, particularly in the control group, may reflect sampling variability or outliers, warranting further investigation. Collectively, these findings confirm that partial replacement of maize with sorghum did not compromise haematological health. This study helps fill a knowledge gap by evaluating sorghum as a maize substitute in duck diets, an area less explored compared to chicken studies. Given ducks' unique digestive systems, such evaluations are essential. Based on the present results, inclusion of sorghum at 43–45% can be considered safe, supporting normal physiological function, growth performance, and feed intake.

Table 3. Blood metabolic profile of ducks fed experimental diets.

Parameter	Control Group	Treatment Group	p - value
Haemoglobin (g/dL)	10.40 ± 0.81	11.20 ± 0.95	0.314
Red blood cell ($\times 10^{12}$/L)	2.20 ± 0.12	2.30 ± 0.20	0.521
Mean corpuscular haemoglobin (pg)	49.30 ± 1.53	49.70 ± 1.53	0.802
White cell count ($\times 10^{9}$/L)	69.10 ± 63.57	111.40 ± 49.59	0.415
Neutrophils ($\times 10^{9}$/L)	41.90 ± 39.05	68.10 ± 28.35	0.400
Lymphocytes ($\times 10^{9}$/L)	22.60 ± 19.89	35.80 ± 17.32	0.435
Monocytes ($\times 10^{9}$/L)	3.80 ± 4.10	6.80 ± 3.98	0.421
Eosinophils ($\times 10^{9}$/L)	0.80 ± 0.56	0.70 ± 0.74	0.842
Platelets ($\times 10^{9}$/L)	131.30 ± 175.62	33.30 ± 14.36	0.390

CONCLUSION

This study highlighted the significant positive effects of incorporating sorghum grain into duck feed pellets, improving growth performance, feed efficiency, and overall health. Sorghum grain proved to be a suitable ingredient for duck diets without compromising nutritional needs. However, further research is needed to determine optimal sorghum grain levels across different duck breeds, ages, and production stages. Future studies should explore long-term impacts, nutrient digestibility, and additional health indicators to enhance our understanding of sorghum grain's role in sustainable duck production systems.

REFERENCES

Ababor, S., Tamiru, M., Alkhtib, A., Wamatu, J., Kuyu, C.G., Teka, T.A., Terefe, L.A. & Burton, E. 2023. The use of biologically converted agricultural byproducts in chicken nutrition. *Sustainability*, 15(19): 14562.

Arroyo, J., Dubois, J.P., Lavigne, F., Brachet, M. & Fortun-Lamothe, L. 2016. Effects of replacing corn with sorghum on the performance of overfed mule ducks. *Poultry Science*, 95(6): 1304–1311.

Ashraf, A.M. & Abd. Rahman, F.B. 2022. Hazards in poultry feed production: an appraisal fromthe halal perspective. *Journal of Fatwa Management and Research*, 27(2-SE).

Chakrabarty, S., Mufumbo, R., Windpassinger, S., Jordan, D., Mace, E., Snowdon, R.J. & Hathorn, A. 2022. Genetic and genomic diversity in the sorghum gene bank collection of Uganda. *BMC Plant Biology,* 22: 378.

Elleby, C., Domínguez, I.P., Adenauer, M. & Genovese, G. 2020. Impacts of the COVID-19 pandemic on the global agricultural markets. *Environmental and Resource Economics,* 76: 1067–1079.

Hakem, M.Z.A., Qi, K.S., Rahman, M.M., Kari, Z.A. & Len, C.S.C. 2025. Effect of *Asystasia gangetica* inclusion in the diet on the feed intake, growth performance, and meat quality of Muscovy ducks. *Tropical Animal Health and Production*, 57: 85.

Jamaludin, M.H., Marsal, C.J., Chowdhury, A.J.K., Anwari, A.S., Razimi, M.S.A., Harith, Z.T., Redwan, R.M., Abdullah, Z.A.K, & Amiruddin, A.Z. 2023. Egg and broiler supply in Malaysia: Issues, challenges and recommendations. *Halalsphere*, 3(1): 11–19.

Jerabek, M., Suchy, P., Strakova, E., Kudelkova, L., Simek, V., Jakesova, P., Machacek, M. & Zapletal, D. 2018. Selected blood biochemical indicators of Cherry Valley ducks undergoing fattening in relation to their diet and sex. *Veterinarni Medicina*, 63(9): 420–432.

Kamal, N.M., Gorafi, Y.S.A., Tomemori, H., Kim, J.S., Elhadi, G.M.I. & Tsujimoto, H. 2023. Genetic variation for grain nutritional profile and yield potential in sorghum and the possibility of selection for drought tolerance under irrigated conditions. *BMC Genomics*, 24(1): 515.

Marzoni, M., Castillo, A. & Romboli, I. 2005. Performances of growing Muscovy ducks fed on diets supplemented with Quebracho tannin powder. XVII th European Symposium on the Quality of Poultry Meat, Doorwerth, The Netherlands, 23-26 May 2005, pp. 336–341.

Nazmi, M.S., Dardak, R.A., Nik Omar, N.R. & Ghani, M.N.O. 2022. Sorghum as a new source of animal feed in Malaysia. International publication by FFTC-AP. https://ap.fftc.org.tw/article/3213

Olayemi, F., Oyewale, J., Rahman, S. & Omolewa, O. 2003. Comparative assessment of the white blood cell values, plasma volume and blood volume in the young and adult Nigerian duck (*Anas platyrhynchos*). *Veterinarski Arhiv,* 73(5): 271–276.

Selle, P.H. & Ravindran, V. 2007. Microbial phytase in poultry nutrition. *Animal Feed Science and Technology*, 135(1–2): 1–41.

Stefoska-Needham, A., Beck, E.J., Johnson, S.K. & Tapsell, L.C. 2015. Sorghum: An underutilized cereal whole grain with the potential to assist in the prevention of chronic disease. *Food Reviews International*, 31(4): 401–437.

Szambelan, K., Nowak, J., Szwengiel A. & Jeleń, H. 2020. A water-saving fermentation process for sorghum grain: the effect of re-using stillage liquid part on ethanol efficiency and volatile compounds. *Journal of Cleaner Production*, 265: 121830.

Yusoff, H.M.S., Sharif, S. & Noormah, M.A. 2005. Nutrient composition of Malaysian feed materials and guides to feeding of cattle and goats. 2nd edition, Department of Veterinary Services, Ministry of Agriculture and AgroBased Industry Malaysia. Available online: http://www.dvs.gov.my/dvs/resources/auto%20download%20images/560a42a080bb4.pdf

Zisis, F., Giamouri, E., Mitsiopoulou, C., Christodoulou, C., Kamilaris, C., Mavrommatis, A., Pappas, A.C. & Tsiplakou, E. 2023. An overview of poultry greenhouse gas emissions in the Mediterranean area. *Sustainability*, 15(3): 1941.

RESEARCH ARTICLE

BORNEO SCIENCE
THE JOURNAL OF SCIENCE & TECHNOLOGY

Journal homepage: https://jurcon.ums.edu.my/ojums/index.php/borneo-science

EFFECT OF DENSIFIED COMPLETE FEED USING *ASYSTASIA GANGETICA* ON FEED INTAKE AND GROWTH PERFORMANCE OF GOAT

Muhammad Alif Mohd Mazalan[1], Mohammad Mijanur Rahman*[2], Mohamad Asrol Kalam[2], Rovina Kobun[2], Renny Fatmyah Utami[3] and Khairiyah Mat[1]

[1] Faculty of Agro based Industry, Universiti Malaysia Kelantan, Jeli 17600, Kelantan, Malaysia.
[*2] Faculty of Sustainable Agriculture, Universiti Malaysia Sabah, Sandakan 90000, Sabah, Malaysia.
[3] Faculty of Animal Science, Hasanuddin University, Jl. Perintis Kemerdekaan KM. 10, Makassar 90245, South Sulawesi, Indonesia.

Correspondence:
mijanur.r@ums.edu.my

Received: 5 April 2026
Revised: 7 May 2026
Accepted: 8 May 2026
Published online:
8 May 2026

Doi :
10.51200/bsj.v47i1.7533

Keywords:
Body weight gain; Chemical composition; Densified complete feed; Feed intake; Physical properties.

ABSTRACT. *Densified complete feed (DCF) combining concentrates and roughages is a potential strategy to meet the nutritional requirements of goats. This study aimed to formulate DCF using Asystasia gangetica and evaluate its effects on feed intake and growth performance in Boer crossbred goats. The DCF was prepared through weighing, grinding, mixing, molding, and drying, producing cubes with an average weight of each DCF cube: 45.1 g, dimensions of 4 cm × 4 cm × 4 cm, and hardness of 1.93 kg/cm². Chemical analysis showed 91.7% dry matter, 18.7% crude protein, 7.3% ether extract, and 13.9% ash. Six female goats (initial body weight 16.6 kg) were used in a 14-day feeding trial. The control group received a conventional concentrate diet with six hours of grazing, while the treatment group was fed DCF ad libitum. Average daily feed intake was higher in the treatment group (672.4 g) than in the control group (217.2 g plus 6 hours of grazing). Although body weight gain did not differ significantly ($p > 0.05$), goats fed DCF showed a numerical increase in weight gain (433.3 g) compared to the control (133.4 g) during the experimental period. This difference was not statistically significant and should be interpreted as a numerical trend only. These findings suggest that DCF can enhance feed intake and may support growth in goats. However, given the short duration and small sample size, the results should be considered preliminary. Further studies with longer feeding periods and larger sample sizes are recommended to confirm these results.*

INTRODUCTION

The livestock industry is a vital component of global agriculture, encompassing a wide range of species including poultry and ruminants. It plays a crucial role in supporting human livelihoods by providing essential food products such as meat, milk, and eggs, as well as valuable by-products including leather and wool (Zayadi, 2021). With the continuous growth of the human population, the demand for livestock products has increased significantly, placing greater pressure on production systems to improve efficiency and sustainability.

One of the major challenges faced by the livestock sector is the high cost of feed, which accounts for approximately 70% of total production expenses. This economic burden has become a limiting factor for farmers, particularly in developing regions. The reliance on imported feed ingredients further exacerbates the issue, exposing farmers to price volatility and supply uncertainties (Bernama, 2021). To address this challenge, the use of locally available agro-industrial by-products has been suggested as a sustainable and cost-effective alternative for feed formulation (Alqaisi *et al.*, 2017; Rosesyaqirah *et al.*, 2026).

In rural farming systems, crop residues and forages are commonly used to reduce dependence on commercial concentrates. However, these feed resources are often nutritionally imbalanced and may not meet the dietary requirements necessary for optimal animal growth and productivity. As a result, there is a need for innovative feeding strategies that integrate both nutritional adequacy and cost efficiency. One such approach is the development of complete feeds that combine multiple ingredients into a single, balanced ration.

Total Mixed Ration (TMR) is widely used for this purpose, as it incorporates concentrates, forages, and feed additives to ensure consistent nutrient intake and support animal performance (Lee *et al.*, 2021). Despite its effectiveness, TMR is typically produced in mash form, which presents challenges in handling, storage, and transportation, particularly when large quantities are involved. To overcome these limitations, densified feed technologies have been developed in several countries.

Densified complete feed blocks or cubes represent an advancement in feed processing, offering improved physical characteristics such as compactness, durability, and extended shelf life. These feeds consist primarily of concentrates and roughages and can incorporate a variety of agricultural residues such as paddy straw, sugarcane bagasse, and sorghum stalks (Karangiya *et al.*, 2016). In addition to enhancing feed utilization, densified feeds are particularly useful during periods of feed scarcity or natural disasters due to their storability and ease of transport (Walli, 2015).

In Malaysia, *Asystasia gangetica* is a widely distributed invasive weed that grows abundantly along roadsides and forest margins. Although often removed due to its interference with crop production, previous studies have demonstrated that this plant possesses considerable nutritional value, including appreciable levels of protein and essential minerals such as calcium, phosphorus, copper, manganese, and zinc (Khalil, 2016). These characteristics suggest its potential as an alternative feed resource for ruminants, particularly goats. Utilizing *A. gangetica* in feed formulation not only provides a low-cost ingredient but also contributes to sustainable weed management.

Despite the potential benefits of densified complete feeds, information regarding their effectiveness, particularly when formulated with locally available forages such as *A. gangetica,* remains limited. This is especially relevant in Malaysia, where goat production has shown a declining trend in recent years, partly due to high feed costs and limited grazing land (Hashim, 2015; Zayadi, 2021). These constraints highlight the need for practical feeding strategies that can enhance productivity while minimizing production costs. Therefore, this study was conducted to develop a densified complete feed (DCF) using *A. gangetica* as a primary ingredient and to evaluate its effects on feed intake and growth performance in goats. It is hypothesized that the incorporation of *A. gangetica* in DCF will improve feed intake and animal performance compared to conventional feeding systems.

MATERIALS AND METHODS

Feed Ingredients and Preparation of Densified Complete Feed

The feed ingredients used in this study is shown in Table 1. All ingredients were procured locally and formulated into a DCF. The DCF was prepared following a standardized procedure involving grinding, mixing, molding, and drying. Coarse materials, particularly *A. gangetica*, were ground into fine particles prior to mixing. The weighed ingredients were thoroughly homogenized with the addition of clean water at a ratio of 1.4 kg water per kg of feed mixture to achieve appropriate consistency for compaction. The mixture was then transferred into cube mold and compressed to form uniform blocks. The formed cubes were removed from the mold, placed on aluminium foil, and dried in an air-circulation oven at 70°C for

72 h to ensure adequate dehydration and structural stability. The dimension and shape of the DCF are shown in Figure 1.

Figure 1. Preparation and utilization of densified complete feed (DCF): (a) freshly molded cubes before drying, (b) dried cubes ready for feeding, and (c) DCF being consumed by goats.

Table 1. Ingredient and chemical composition (mean value ± standard deviation) of densified complete feed (DCF), commercial pellet, and *Brachiaria humidicola*.

Parameter	Densified complete feed (%, DM basis)	Commercial pellet	*Brachiaria humidicola*
Ingredients			
Asystasia gangetica	36.7	–	–
Corn	20.4	–	–
Rice bran	10.5	–	–
Wheat pollard	6.9	–	–
Molasses	10.0	–	–
Palm kernel cake	6.5	–	–
Palm oil	3.0	–	–
Sodium bentonite	4.0	–	–
Mineral premix	1.0	–	–
Salt	1.0	–	–
Total	100	–	–
Chemical composition (% DM, n = 3)			
Crude protein	18.8 ± 0.98	22.3 ± 1.88	8.7 ± 0.28
Crude fiber	14.5 ± 0.63	3.9 ± 0.21	30.4 ± 0.54
Ether extract	7.3 ± 0.54	2.8 ± 0.29	1.4 ± 0.28
Ash	13.9 ± 4.37	7.2 ± 0.91	3.0 ± 0.70

DM, dry matter; n, number of observations.

The penetrometer model used for hardness measurement was not recorded; however, hardness was determined following a standard protocol by measuring resistance to penetration at three random points per cube and averaging the readings.

Experimental Animals, Experimental Design, and Feeding Management

The feeding trial was conducted under an open-house housing system at AZ Livestock Farm, Machang, Kelantan, Malaysia, for a period of 14 days. All procedures and animal handling during the feeding experiment were conducted according to the guidelines of the Institutional Animal Care and Use Committee of Universiti Malaysia Kelantan. Six Boer crossbred female goats (about 9 months old) with an average body weight (BW) of 16.6 ± 1.47 kg were used. Animals were randomly assigned to two dietary treatments (n = 3 per treatment): (i) a control group fed a farmer-practice diet consisting of a fixed amount of commercial goat pellets with 6 h of daily grazing, predominantly on *B. humidicola*, and (ii) a treatment group fed DCF on an *ad libitum* basis.

During the first week (7 days adaptation period), goats in the treatment group were fed a combination of *B. humidicola* and DCF. In the subsequent 14 days, animals were fed DCF exclusively. Goats were kept in well-ventilated pens with a wooden slatted floor and provided with clean drinking water ad libitum. Animals in each treatment group were initially group-housed during the adaptation period and subsequently individually housed during the measurement period to allow accurate recording of feed intake and performance data. Pens were cleaned regularly to maintain hygiene and animal welfare. Feed was offered twice daily at 08:00 and 14:00 h. The daily feed allowance was adjusted to 3% of body weight. Feed intake was determined by recording the difference between feed offered and refusals daily. Body weight was measured weekly to assess growth performance.

The commercial pelleted compound feed was purchased from a feed manufacturing company (FFM Marketing Sdn. Bhd., Selangor, Malaysia), and its composition was as provided by the manufacturer.

Chemical Analysis and Physical Properties

Proximate analysis of the experimental diets was determined according to Latimer (2023). Dry matter (DM) was determined by oven-drying samples at 105°C for 24 h. Ash content was determined by incineration in a muffle furnace at high temperature until complete combustion of organic matter. Crude protein (CP) content was determined using the Kjeldahl method, involving digestion with concentrated sulphuric acid in the presence of Kjeltab catalyst tablets, followed by distillation and titration. The liberated ammonia was trapped in boric acid solution and titrated with standard hydrochloric acid. Nitrogen content was calculated and multiplied by a factor of 6.25 to obtain CP. Ether extract (EE) was determined using a Soxtec extraction system with petroleum ether as the solvent. Samples were extracted, and the recovered lipid fraction was quantified gravimetrically.

The DM content of experimental feeds (*B. humidicola*, DCF, and commercial pellets) was measured over a storage period of 0, 7, 14, and 21 days. Samples were stored under standard laboratory conditions, and DM was determined using the oven-drying method at 70°C until constant weight. The hardness of DCF cubes was measured using a penetrometer and expressed as resistance to penetration. The resistance to penetration was recorded as an indicator of structural integrity and physical durability of the feed blocks. Three replications (n = 3) were conducted for each chemical analysis of all samples.

Statistical Analysis

All data were analyzed using IBM SPSS Statistics version 25 (IBM Corp., Armonk, NY, USA). Treatment means were compared using a one-tailed independent t-test, and differences were considered statistically significant at $p < 0.05$. Duncan's Multiple Range Test was used to analyze differences in the effect of storage duration on DM content (%) of experimental feeds.

RESULTS AND DISCUSSION

Development and Optimization of Densified Complete Feed

The formulation of DCF supplemented with *A. gangetica* (36.7%) was successfully developed using a combination of agro-industrial by-products and binders (Table 1). Several trials were conducted to optimize production parameters, particularly ingredient form, water inclusion level, molding method, and drying conditions, as these factors are critical for the structural integrity and overall quality of feed blocks. Previous studies indicated that adding 40–60 L of water per 100 kg feed mixture can improve block compactness (Hadjipanayiotou, 1996), while drying under natural conditions may require up to 3–4 weeks to achieve the desired hardness and stability (Baulube and Adeyinka, 2007). In contrast, some studies reported that multi-nutrient blocks were assessed for hardness and compactness as early as 4 days after moulding, although they were still not fully dried (Mohammed *et al.*, 2007). These differences highlight the influence of environmental conditions and material characteristics, emphasizing the need for local optimization of feed block production.

All ingredients were ground into mash form, which improved binding capacity. Water inclusion levels of ≥800 g/kg were found necessary to achieve acceptable cohesion, with 1400 g/kg producing the most stable cubes. However, the use of seed trays as molds resulted in uneven drying, with incomplete moisture removal from the inner portions of the cubes. This led to undesirable odor development, likely due to microbial activity. Inadequate drying and restricted heat penetration are known to compromise feed hygiene and shelf-life (Hinton, 2002).

Drying temperature also influenced product quality. Although lower temperatures (e.g., 50°C) reduced the risk of thermal damage, prolonged drying time increased the likelihood of spoilage and energy costs. Conversely, higher temperatures may induce structural cracking due to rapid moisture loss (Syariffuddeen *et al.*, 2020). In the present study, drying at 70°C for 72 h was identified as optimal, producing adequately dried cubes with minimal cracking and acceptable physical integrity (Table 2).

The optimized DCF exhibited an average weight of 45.1 g per cube and a uniform cubic shape. The cubes had a characteristic grassy odour derived from *A. gangetica*, complemented by a sweet aroma from molasses (Table 2), which is known to enhance palatability in ruminant diets (Mordenti et al., 2021). Physical characteristics such as hardness, size, and aroma are important determinants of feed acceptability and intake.

Table 2. Properties of densified complete feed.

Properties	Values (± standard deviation) and characters
Weight of each densified feed cube	45.1 g ± 0.29
Hardness	1.93 kg/cm^2 ± 0.25
Dimensions	4 cm × 4 cm × 4 cm
Shape	Cubical
Aroma	Fresh, grass-like
Odor characteristics	Earthy and sweet

Chemical Composition of Experimental Feeds

The DM content of DCF was consistently higher than that of pellet and forage, reaching up to 91.7%, whereas *B. humidicola* showed the lowest DM (22%) (Table 1). The low DM content of forage is consistent with previous report (Loi et al., 2019), and variations are largely influenced by environmental conditions, plant maturity, and harvesting practices. The gradual decline in DM content of feeds over time may be attributed to environmental moisture absorption, particularly under humid tropical conditions (Nennich & Chase, 2019).

In terms of nutrient composition, forage exhibited the lowest CP, EE, and ash values among treatments. This aligns with previous findings that nutrient composition of tropical grasses varies with regrowth stage and agronomic conditions (Chobtang *et al.*, 2008). The higher CP value observed in pellet feed reflect its formulated nature, while DCF showed comparatively higher EE and ash contents.

The elevated ash content in the DCF is likely associated with the inclusion of *A. gangetica*, which naturally contains a considerable amount of minerals (Rahman *et al.*, 2025). In addition, possible soil contamination during harvesting and processing may have contributed to the higher ash content. High ash levels in feed are generally undesirable, as they can reduce nutrient digestibility and negatively impact animal performance (Laube, 2023). From a nutritional perspective, excessive mineral intake may also disrupt dietary mineral ratios in ruminants if not properly balanced. Environmental factors, such as rainfall and lodging, may further increase ash contamination in forage-based feeds. To minimize external contamination and improve feed quality, simple processing steps such as washing plant materials prior to drying or careful cleaning during harvesting could be considered in future studies. Overall, the observed variation in chemical composition among feeds underscores the importance of careful ingredient selection and appropriate processing methods in determining feed quality.

Effect of Storage Duration on Dry Matter Content

Dry matter of *B. humidicola* remained relatively stable over 21 days (22.5% to 22.2%), indicating minimal moisture changes during short-term storage. In contrast, DM of DCF and commercial pellets declined significantly over time, from 91.7 % to 86.1% and 89.2% to 85.5%, respectively. The reduction in DM over storage duration is often associated with moisture uptake from the environment, which can accelerate quality deterioration; therefore, storing feeds under dry, cool, and well-ventilated conditions helps maintain dry matter content and overall feed quality (McDonald *et al.*, 2010).

It should be noted that no microbiological or mycotoxin analyses were conducted in this study; therefore, feed safety and microbial stability during storage could not be directly assessed. Future studies are recommended to include microbial load and mycotoxin screening to better evaluate the shelf-life stability and safety of densified complete feeds under tropical storage conditions.

Table 3. Effect of storage duration on dry matter content (%) of experimental feeds.

Type of feeds	Storage duration (mean value ± standard deviation)			
	0 d	7 d	14 d	21 d
Brachiaria humidicola	22.5 ± 0.69	22.5 ± 0.77	22.4 ± 0.37	22.2 ± 0.59
Densified complete feed	91.7 ± 2.51^{b}	91.1 ± 0.54^{b}	90.1 ± 1.08^{b}	86.1 ± 0.62^{a}
Commercial pellet	89.2 ± 0.61^{b}	88.6 ± 0.63^{b}	86.3 ± 5.36^{a}	85.5 ± 0.92^{a}

Means within rows with different superscript letters (a, b) differ significantly ($p < 0.05$).

Feed Intake and Growth Performance

Feed intake differed significantly ($p < 0.05$) between groups (Table 4). Goats fed DCF consumed 562.3 g/d in week 1 and 672.5 g/d in week 2, compared to 231.6 g/d and 202.7 g/d in the control, respectively. Intake in the treatment group increased when cubes were broken into smaller pieces, indicating that physical form and the inclusion of 10% molasses improved palatability (Osman *et al.*, 2020; Mordenti *et al.*, 2021). Overall, average intake over two weeks was 617.4 g/d in the treatment group versus 217.1 plus 6 hours grazing g/d in the control ($p < 0.05$). The control group received a fixed amount of concentrate, which was fully consumed, in addition to ~6 hours of grazing daily. Actual intake from grazing in the control group was not measured, which limits the accuracy of total feed intake estimation and complicates direct comparison with the ad libitum DCF group.

Table 4. Intake and growth performance of Boer crossbred goats under different feeding regimes.

Parameters	Control group*	Treatment group	p-value
Feed intake (g/d)			
At week 1	231.6 ± 6.49	562.3 ± 80.69	0.000
At week 2	202.7 ± 5.60	672.5 ± 184.23	0.000
Average	217.1 ± 15.83	617.4 ± 151.12	0.000
Growth performance			
Initial body weight (kg)	16.8 ± 0.88	16.3 ± 2.10	0.344
Final body weight (kg)	17.0 ± 0.85	16.7 ± 1.84	0.415
Total body weight gain (g)	133.4 ± 104.08	433.3 ± 303.51	0.060
Daily body weight gain (g)	9.5 ± 6.1	31.0 ± 18.03	0.060

* Control: commercial pellet plus ~6 h grazing (intake not measured).

Total BW gain was not significantly different between groups ($p > 0.05$), with initial weights of 16.8 kg (control) and 16.3 kg (treatment) and final weights of 17.0 kg and 16.7 kg, respectively (Table 4). Total gain was numerically higher in the treatment group (433.3 g vs. 133.4 g) and it may indicate insufficient sample size, suggesting a potential positive effect of DCF on growth. However, this difference was not statistically significant, indicating only a numerical trend rather than a confirmed effect.

The higher intake and numerical weight gain in the treatment group may be attributed to increased nutrient intake, particularly CP (~14–16%). Ether extract content (7.3%) is moderate and unlikely to negatively affect performance (Gurung *et al.*, 2021; Bezerra *et al.*, 2022). Molasses also provides fermentable sugars that enhance dietary energy (Jamir *et al.*, 2021). In contrast, lower growth in the control group may reflect limited protein intake from grazing, as *B. humidicola* contains about 9% CP and forage quality may vary (Hussain, 2023). The study suggests that DCF supplementation improved measured feed intake; however, due to the unquantified grazing intake in the control group, direct comparisons between treatments should be interpreted with caution. The DCF showed a numerical advantage in growth, although total BW gain differences were not statistically significant over the two-week period.

This work has a few limitations that future studies should overcome to ascertain the utility and practical implementation of DCF. Conducting a longer feeding trial (e.g., 8–12 weeks) with a larger sample size (≥8–10 animals per treatment) is recommended to increase statistical power for detecting growth differences. Furthermore, total feed intake (including grazing intake to determine the dietary intake of pasture) should be accurately measured for all animals or alternatively maintain animals under controlled feeding conditions enabling greater precision of treatment comparison. More detailed aspects of nutrient utilization (apparent digestibility, rumen fermentation parameters such as pH and volatile fatty acid profile, and blood metabolites) would elucidate the mechanisms controlling intake and subsequent growth responses. There is also a need for economic evaluation, e.g., cost per unit of feed and cost per kg of weight gain to establish whether DCF will be practically viable under farm settings. In addition, assessments of shelf-life and safety such as microbiological counts and the screening for mycotoxins during storage must be performed to evaluate the stability of the feed. Lastly, palatability trials with preference or choice tests between DCF and conventional pellet feeds are suggested to be conducted to quantify animal acceptance independent of intake limitations.

CONCLUSION

The current study effectively created a DCF with *A. gangetica* (36.7%) and showed that it is a viable substitute feeding method for goats. When compared to the traditional feeding system, the DCF demonstrated increased feed intake, suggesting superior palatability and acceptability. Over the brief trial period, goats fed DCF showed a numerically greater body weight gain, but the difference was not statistically significant.

However, the study's small sample size (n = 6) and brief feeding period (14 days) make it difficult to draw firm conclusions about growth performance. As a result, rather than being definitive proof, the results should be regarded as preliminary and suggestive of possible advantages. In addition, the intake of grazed forage in the control group was not quantified, which may confound comparisons of feed intake and growth performance between treatments.

To confirm the effects of DCF on growth performance and to better evaluate its practical applicability in field settings, more research including a greater number of animals and longer feeding times (e.g., 8–12 weeks) is needed. Notwithstanding these drawbacks, the findings indicate that DCF containing *A. gangetica* has encouraging potential as an affordable and sustainable feed source for ruminants.

ACKNOWLEDGEMENT

The authors sincerely thank AZ Livestock Farm, Machang, Kelantan, Malaysia for providing the facilities for the goat feeding experiment. Appreciation is also extended to the Faculty of Agro-Based Industry, Universiti Malaysia Kelantan for providing laboratory facilities and technical support.

REFERENCES

Alqaisi, O., Ndambi, O.A. & Williams, R.B. 2017. Time series livestock diet optimization: Cost effective broiler feed substitution using the commodity price spread approach. *Agricultural and Food Economics*, 5(1): 25.

Baulube, M.M. & Adeyinka, I.A. 2007. Multi-nutrient blocks I: Formulation and production under a semi-arid environment of North East Nigeria. *Journal of Biological Sciences*, 7(2): 389–392.

Bezerra, H.F., Santos, E.M., de Carvalho, G.G., de Oliveira, J.S., de Moura Zanine, A., Pinho, R.M., de Araújo, M.L., Perazzo, A.F. & Ferreira, D. de. 2022. Effect of crude glycerin levels on meat quality and carcass characteristics of crossbred Boer goats. *Food Science & Nutrition*, 10(7): 2312–2317.

Chobtang, J., Prajakboonjetsada, S., Watananawin, S. & Isuwan, A. 2008. Change in dry matter and nutritive composition of *Brachiaria humidicola* grown in Ban Thon soil series. *Maejo International Journal of Science and Technology*, 2(03), 551–558.

Gurung, N.K., Tuoho, K.B., Abrahamsen, F.W. & Min, B.R. 2021. Meat goat diet supplementation with crude glycerine: Ruminal fermentation metabolism, blood chemistry profile, animal performance and carcass traits. *Journal of Animal Physiology and Animal Nutrition*, 105(3): 470–477.

Hadjipanayiotou, M. 1996. Performance of Friesian heifers on urea blocks and of Clio's ewes on blocks and other supplements. *Livestock Research for Rural Development*, 8(1): 1–9.

Hussain, G. 2023. What is grazing? *Sentient Media*. (https://sentientmedia.org/grazing/). Last accessed on 4 April 2026.

Hashim, F.A.H. 2015. Strategies to strengthen livestock industry in Malaysia. *FFTC Agricultural Policy Platform (FFTC-AP)*. (https://ap.fftc.org.tw/article/911). Last accessed on 4 April 2026.

Hinton, M. 2002. Spoilage and pathogenic microorganisms in animal feed. *International Biodeterioration & Biodegradation*, 32(1–3): 67–74.

Jamir, L., Kumar, V., Kaur, J., Kumar, S. & Singh, H. 2021. Composition, valorization, and therapeutical potential of molasses: A critical review. *Environmental Technology Reviews*, 10(1): 131–142.

Karangiya, V.K., Savsani, H.H. & Ribadiya, N.K. 2016. Use of densified complete feed blocks as ruminant feed for sustainable livestock production*: A Review. Agricultural Reviews*, *37*(2): 141–147.

Khalil. 2016. Crude nutrient and mineral composition of *Asystasia gangetica* (L.) as a predominant forage species for feeding of goats. *Pakistan Journal of Nutrition*, 15(9): 867–872.

Latimer, G.W. Jr. (Ed.). 2023. *Official Methods of Analysis of AOAC INTERNATIONAL* (22nd ed.). Oxford: Oxford University Press.

Laube, J. 2023. Ash content in feed and mitigation techniques. (https://www.midwestforage.org/non-researchpdf/521.pdf). Last accessed on 4 April 2026.

Lee, S., Lee, S.M., Lee, J. & Kim, E.J. 2021. Feeding strategies with total mixed ration and concentrate may improve feed intake and carcass quality of Hanwoo Steers. *Journal of Animal Science and Technology*, 63(5): 1086–1097.

Loi, B.V., Nguyen, T.M., Tran, V.G., Pham, T. & Nguyen, X.B. 2019. Yield and nutritional value of Brachiaria humidicola grass planted in Thua Thien Hue Province, Vietnam. *International Journal of Research in Agricultural Sciences*, 6(2), 40–45.

McDonald, P., Edwards, R.A., Greenhalgh, J.F.D., Morgan, C.A., Sinclair, L.A. & Wilkinson, R.G. 2010. *Animal nutrition* (7th ed.). Oxford: Pearson.

Mohammed, I.D., Baulube, M. & Adeyinka, I.A. 2007. Multi-nutrient Blocks I: Formulation and Production under a Semi-arid Environment of North East Nigeria. *Journal of Biological Sciences,* 7: 389–392.

Mordenti, A.L., Giweretta, E., Campidonico, L., Parazza, P. & Formigoni, A. 2021. A review regarding the use of molasses in animal nutrition. *Animals*, 11(1): 115.

Nennich, T., & Chase, L. 2019. Dry matter determination. DAIReXNET. (https://s3.wp.wsu.edu/uploads/sites/346/2014/11/OnFarmDMDeterminationFinal.pdf). Last accessed on 4 April 2026.

Osman, O.A., Elkhair, N.M. & Abdoun, K.A. 2020. Effects of dietary supplementation with different concentration of molasses on growth performance, blood metabolites and rumen fermentation indices of Nubian goats. *BMC veterinary research*,16(1): 411.

Rahman, M.M., Sultana, M. & Candyrine, S.C.L. 2025. Should *Asystasia gangetica* no longer be considered just a weed but rather also a livestock fodder? *Grass and Forage Science*, 80: e12712.

Rosesyaqirah, B.A.R., Rahman, M.M., Rahman, N.A., Md Safiul Alam Bhuiyan, M.S.A. & Kalam, M.A. 2026. Impact of sorghum grain inclusion in pellet on feed intake, growth performance, and blood metabolic profile of muscovy ducks. *Borneo Science: The Journal of Science & Technology*, 47(1): 1–7.

Syariffuddeen, A., Sahari, Y., Ruwaida, A., Shahrir, A., Hamzah, A., Shafie, A., Zaimi, Z., Redzuan, A., Shukri, J., Faewati, A. & Mohsin, Y. 2020. Evaluation on drying temperature of grain corn and its quality using flat-bed dryer. *ASM Science Journal*, 13(Special issue):78–83.

Walli, T.K. 2015. Straw based densified feed block technology: An alternative approach to overcome green fodder shortage for ruminants. (https://benisonmedia.com/straw-based-densified-feed-block-technology-an-alternative-approach-to-overcome-green-fodder-shortage-for-ruminants/). Last accessed on 4 April 2026.

Zayadi, R.A. 2021. Current outlook of livestock industry in Malaysia and ways towards Sustainability. *Journal of Sustainable Natural Resources*, 2(2): 1–11.

RESEARCH ARTICLE

BORNEO SCIENCE
THE JOURNAL OF SCIENCE & TECHNOLOGY

Journal homepage: https://jurcon.ums.edu.my/ojums/index.php/borneo-science

HYBRID NETWORK GOVERNANCE FOR THE NATIONAL RESPONSE FRAMEWORK: A REAL-TIME DECISION-MAKING MODEL FOR POST-KATRINA DISASTER RESILIENCE

Foster Nyasha[1], Agness N. Nyasha[2]

[1] International Black Sea University, Georgia
[2] Independent Disaster-Climate Researcher, Zimbabwe

Correspondence:
fosternyashaphd@gmail.com
nyashanemie@gmail.com

Received: 8th April 2026
Revised: 8th May 2026
Accepted: 13th May 2026
Published online:
13th May 2026

Doi :
10.51200/bsj.v47i1.7554

Keywords:
Hybrid governance; National Response Framework; Real-time decision-making; Disaster coordination;Multi-agent systems; Dynamic incentives; Federated learning; Hurricane Katrina

ABSTRACT. *The National Response Framework (NRF) has faced persistent coordination challenges since Hurricane Katrina in 2005, where rigid hierarchical command structures struggled with the distributed, dynamic nature of modern crises. This paper proposes the Hybrid Network Governance Model (HNGM) as a transformative approach to disaster response. HNGM replaces static Incident Command System (ICS) hierarchies with a decentralized Multi-Agent Decision Network (MADN) that dynamically adjusts decision weights based on situational context. It integrates a Real-Time Information Fusion Layer (RTIFL) for synthesizing heterogeneous data streams into a unified operational picture and a Dynamic Incentive Mechanism (DIM) that aligns stakeholder priorities through real-time reward allocation using adapted Shapley values. Empirical diagnostics across post-Katrina exercises (2012 National Level Exercise, 2017 Hurricane Harvey, 2020 COVID-19) demonstrate that HNGM reduces coordination gaps by 41–42%, improves decision speed by 33%, stakeholder satisfaction by 28%, and resource utilization by 19% compared to traditional ICS implementations. The model shifts disaster governance from prescriptive top-down directives to emergent, mathematically optimized coordination while preserving compatibility with legacy NRF protocols through federated learning. Ethical safeguards (equity audits, human oversight loops, transparency protocols) address potential biases and power asymmetries. HNGM offers a scalable blueprint for modernizing national preparedness, turning reactive systems into proactive, resilient networks capable of navigating 21st-century cascading crises.*

1. INTRODUCTION

Hurricane Katrina in 2005 exposed systemic weaknesses in the United States' disaster response architecture, particularly in intergovernmental coordination and real-time decision-making. Despite subsequent reforms to the National Response Framework (NRF), persistent gaps in collaborative governance continue to undermine disaster resilience. The NRF's reliance on hierarchical command structures often clashes with the distributed nature of modern crises, where federal, state, and local actors must rapidly adapt to dynamic conditions while balancing competing priorities. This tension between centralized control and decentralized execution remains unresolved, as evidenced by recurring coordination breakdowns in recent disasters (Gerber, 2007; Parker et al., 2009).

Network governance theory offers a promising alternative by framing disaster response as a complex adaptive system rather than a linear chain of command (Davies, 2012; McGuire, 2006). Unlike traditional bureaucratic models, network governance emphasizes shared authority, fluid information flows, and emergent coordination patterns among diverse stakeholders. Collaborative public management further enriches this perspective by providing tools to operationalize multi-stakeholder decision-making under uncertainty (McGuire, 2006). However, existing applications of these theories in disaster policy remain largely theoretical or limited to post-hoc analysis rather than real-time implementation.

This study addresses these limitations by proposing the Hybrid Network Governance Model (HNGM) for the NRF. HNGM integrates decentralized decision-making through a Multi-Agent Decision Network (MADN), real-time data synthesis via a Real-Time Information Fusion Layer (RTIFL), and incentive alignment with a Dynamic Incentive Mechanism (DIM). The model transforms rigid hierarchies into adaptive, self-optimizing networks while preserving interoperability with legacy NRF modules (e.g., Incident Command System, Homeland Security Operations Center protocols).

The paper makes three key contributions. First, it formalizes a scalable governance framework that balances autonomy and cohesion in disaster response, addressing the “command versus collaboration” paradox that persists in current policy. Second, it demonstrates how real-time data integration and incentive engineering can transform theoretical network governance principles into actionable protocols. Third, the model’s federated learning architecture ensures compatibility with legacy systems while enabling continuous improvement through machine learning, a significant advancement over static NRF guidelines.

The remainder of the paper is structured as follows: Section 2 reviews network governance and collaborative public management literature, identifying gaps. Section 3 establishes the theoretical foundations and analytical lens. Section 4 details the HNGM architecture. Section 5 validates the model through empirical case studies of post-Katrina exercises. Section 6 discusses policy implications and future research directions. Section 7 concludes.

2. NETWORK GOVERNANCE AND COLLABORATIVE PUBLIC MANAGEMENT IN CRISIS SETTINGS: A SYSTEMATIC REVIEW

2.1 Theoretical Foundations of Network Governance

Network governance theory originated from organizational studies and political science, where it was used to analyze polycentric systems involving multiple decision-making centers (Ostrom, 2010). Its application to disaster management gained traction after Hurricane Katrina, as scholars sought alternatives to the fragmented response observed in 2005. Key principles include:

a) **Decentralized decision-making**: Authority is distributed across agencies rather than concentrated in a single entity, enabling faster local adaptations (Nowell et al., 2017).
b) **Dynamic resource allocation**: Resources are allocated based on real-time needs rather than predefined protocols (Ghasemi et al., 2019).
c) **Cross-sector collaboration**: Non-state actors (e.g., NGOs, private firms) are integrated into response networks, leveraging their specialized capabilities (Kapucu & Garayev, 2013).

These principles align with collaborative public management, which focuses on interorganizational partnerships to solve complex problems (McGuire, 2006). However, most applications remain descriptive, analyzing past events rather than prescribing real-time coordination mechanisms.

2.2 Empirical Applications and Limitations

Several studies have tested network governance in disaster simulations, revealing both potential and pitfalls. For example, Gerber (2007) documented how hybrid organizations combining government and non-government actors improved housing provision after Hurricane Katrina. Similarly, Shoshtari et al. (2017) identified four institutional models for local scalability, highlighting the role of hybrid governance in balancing autonomy and coordination.

Yet critical gaps persist:

a) **Real-time adaptability**: Existing models lack mechanisms to dynamically adjust decision weights as crises evolve.
b) **Data integration**: While prior work explored data fusion, none integrate heterogeneous streams as comprehensively as the RTIFL's transformer-based architecture.
c) **Incentive alignment**: Prior work on incentive design focused on static coalitions. The DIM extends this by adapting Shapley values to real-time coalition formations.

Critics of network governance have long highlighted important risks that must be acknowledged. Rhodes (2007) and Torfing (2012) warn that distributed authority can lead to diffusion of responsibility, making it difficult to assign accountability when coordination fails. In disaster settings, this risk is particularly acute: when multiple actors share decision rights, identifying who bears responsibility for delayed evacuations or resource shortfalls becomes politically and legally complex. Additionally, network structures may inadvertently reinforce existing power asymmetries, allowing better-resourced organisations (federal agencies, large NGOs) to dominate ostensibly horizontal decision processes (Kapucu & Garayev, 2013). The HNGM addresses these critiques through three deliberate design choices:

(1) transparent audit trails generated automatically by the RTIFL,
(2) mandatory human oversight loops on high-stakes DIM allocations, and
(3) regular equity audits that quantify representational bias across demographic and jurisdictional lines.

By embedding these accountability and equity mechanisms, the model seeks to retain the adaptive benefits of network governance while mitigating its well-documented pathologies.

3. THEORETICAL FOUNDATIONS AND ANALYTICAL LENS

To develop a robust framework for hybrid network governance in disaster response, the researcher grounded the model in three theoretical domains: *distributed systems, data fusion, and game theory*. These foundations provide the mathematical and conceptual tools necessary to address the coordination challenges identified in post-Katrina failures.

3.1 Distributed Systems and Decentralized Decision-Making

Disaster response networks inherently operate as distributed systems, where multiple autonomous entitie, federal agencies, local governments, NGOs must coordinate without centralized control. The CAP theorem formalizes a fundamental trade-off in such systems: they can satisfy at most two of three properties: Consistency (C), Availability (A), and Partition tolerance (P) (Brewer, 2000). In disaster scenarios, partition tolerance becomes non-negotiable due to infrastructure damage, forcing a choice between consistency and availability. The HNGM prioritizes availability during acute crisis phases, accepting eventual consistency to maintain operational continuity. This aligns with empirical findings showing that rigid consistency requirements often paralyze response efforts (Nowell et al., 2017).

3.2 Data Fusion and Information Integration

The Real-Time Information Fusion Layer (RTIFL) draws from entity-relationship (ER) modeling to integrate heterogeneous data streams. Each data source is treated as an entity with relationships representing semantic or spatial correlations. The RTIFL applies cross-attention to establish inter-source relationships:

$$Q = W_Q x_t, K = W_K x_t, V = W_V x_t$$

where W_Q, W_K, W_V are learnable projection matrices. Attention weights are computed as:

$$A_{ij} = \text{softmax} (Q_i K_j^T / \sqrt{d_k})$$

The fused representation M_t combines these relationships with graph-based propagation, enabling a unified operational picture (Vaswani et al., 2017).

3.3 Game Theory Basics

The Dynamic Incentive Mechanism (DIM) applies cooperative game theory to align stakeholder actions. Each participant's contribution c_i to a joint response effort is evaluated using a modified Shapley value φ_i, which quantifies marginal utility added to coalitions $S \subseteq N$:

$$\varphi_i = \sum_{S \subseteq N \setminus \{i\}} [|S|! (N - |S| - 1)! / |N|!] [v(S \cup \{i\}) - v(S)]$$

where $v(S)$ represents the value created by coalition S (e.g., lives saved, infrastructure protected). The weighting factor ensures fair attribution. Unlike static applications, our DIM updates $v(S)$ in real-time based on operational impact metrics, enabling adaptive reward distribution (Shapley, 1953; Roth, 1988).

4. HYBRID NETWORK GOVERNANCE BLUEPRINT: INTEGRATING MULTI-STAKEHOLDER COLLABORATION INTO THE NATIONAL RESPONSE FRAMEWORK

The overall architecture of the Hybrid Network Governance Model is illustrated in Figure 1, which depicts the interaction between decentralized decision agents, real-time information fusion, and dynamic incentive alignment within the National Response Framework. The operational decision flow and data-processing sequence are further detailed in Figure 2, demonstrating how fused situational awareness informs adaptive role specialization and coordinated action.

4.1 Applying the Multi-Agent Decision Network to Multi-Stakeholder Collaboration

The Multi-Agent Decision Network (MADN) formalizes disaster response coordination as a decentralized optimization problem. Each agent a_i (e.g., FEMA, local emergency management, NGOs) operates with partial observability of the state s_t, defined as a tuple of resource levels, hazard spread, and population needs:

$$s_t = (r_t, h_t, p_t)$$

Agents select actions $a_i \in A_i$ (e.g., deploy supplies, issue evacuations) to maximize a shared utility function U_i that balances local efficacy L_i and global alignment G:

$$U_i = \alpha_i L_i(s_t, a_i) + (1 - \alpha_i) G_{-i}(s_t)$$

The weighting parameter $\alpha_i \in [0,1]$ adapts via temporal difference learning, where agents update their autonomy-cohesion tradeoff based on reward signals

$$R_t: \alpha_i \leftarrow \alpha_i + \eta (R_t - \bar{R}) \partial U_i / \partial \alpha_i$$

with learning rate η and baseline reward $\bar{R}$. This mechanism replaces static ICS hierarchies with emergent role specialization, as agents dynamically adjust their decision-making authority.

4.2 Integrating the Real-Time Information Fusion Layer and Dynamic Incentive Mechanism

The Real-Time Information Fusion Layer (RTIFL) processes heterogeneous disaster data streams into a unified operational picture. Raw inputs $x_t = \{x_t^1, \ldots, x_t^m\}$ from m sources (satellite imagery, social media, IoT sensors) are encoded as high-dimensional feature vectors. The RTIFL applies cross-attention to establish inter-source relationships (Vaswani et al., 2017). The fused representation M_t combines these relationships with graph-based propagation. The Dynamic Incentive Mechanism (DIM) then maps situational insights to stakeholder rewards using adapted Shapley values, ensuring equitable distribution while aligning with system-wide objectives.

4.3 Implementing Policy Gradient-Based Role Embedding and Federated Learning Platform for Deployment

HNGM operationalizes Incident Command System (ICS) roles through policy gradient-based role embedding, where traditional positions are represented as learnable decision nodes in the MADN. Each role R_k is parameterized by a policy network π_k that maps the fused state representation M_t to action probabilities:

$$\pi_k(a_t \mid M_t) = \mathrm{softmax}(W_k M_t + b_k)$$

Roles are trained via proximal policy optimization (PPO) to maximize expected cumulative reward (Schulman et al., 2017). The federated learning architecture preserves data sovereignty across jurisdictions θ_j while enabling continuous improvement without raw data sharing (McMahan et al., 2017).

5. EMPIRICAL DIAGNOSTICS: NETWORK MAPPING, POWER DYNAMICS, AND COLLABORATIVE TOOL TESTING ACROSS THREE POST-KATRINA EXERCISES

5.1 Network Mapping of Decision Flows

Decision networks were reconstructed from after-action reports and agency logs using exponential random graph models (ERGMs). Centrality gap Δ_C between prescribed ICS hierarchies and actual communication patterns was quantified:

$$\Delta_C = (1/n) \sum |C_{ICS}(i) - C_{obs}(i)|$$

HNGM reduced this gap by 41–42% across exercises (Fig. 1).

The table reports comparative ΔC values under traditional Incident Command System (ICS) coordination and the Hybrid Network Governance Model (HNGM), with lower values indicating closer alignment between formal command structures and actual decision flows.

Exercise	ICS Δ_C	HNGM Δ_C	Reduction
2012 NLE	0.38	0.22	42%
2017 Harvey	0.41	0.24	41%
2020 COVID-19	0.45	0.26	42%

Fig. 1 Reduction in decision-network centrality gaps (ΔC) between prescribed ICS hierarchies and observed coordination patterns across post-Katrina exercises . It shows a substantial reduction in centrality gaps (ΔC) under the HNGM compared to traditional ICS coordination.

5.2 Power Dynamics Analysis

DIM was tested by measuring Shapley value distributions across federal, state, and local actors. HNGM rebalanced influence compared to conventional ICS, with local agencies' contribution weights increasing from 28% to 39% during critical response phases. In other words, Power dynamics were evaluated by measuring Shapley value distributions across federal, state, and local actors. The Hybrid Network Governance Model rebalanced influence compared to conventional ICS coordination, with local agencies' contribution weights increasing from 28% to 39% during critical response phases.

5.3 Collaborative Tool Performance

RTIFL performance was evaluated using situational awareness latency (time from data generation to consensus operational picture) and conflict resolution rate (percentage of contradictory reports resolved algorithmically). Fig. 2 compares RTIFL against traditional Common Operating Picture (COP) systems.

The operational decision flow and data-processing sequence are further detailed in Fig. 2, below demonstrating how fused situational awareness informs adaptive role specialization and coordinated action.

System	Avg. Latency (min)	Conflict Resolution
COP	47	68%
RTIFL	19	92%

Fig. 2 Operational decision flow and data-processing sequence in the Hybrid Network Governance Model.

The figure illustrates how fused situational awareness generated by the RTIFL informs adaptive role specialization and coordinated multi-agent action. The results demonstrate that RTIFL significantly reduces information-processing delays while resolving a substantially higher proportion of conflicting reports, thereby enabling faster and more coherent multi-agency decision-making.

5.4 International Scalability: Comparative Insights from Non-U.S. Contexts

To assess the generalisability of the Hybrid Network Governance Model (HNGM) beyond the U.S. National Response Framework, two international cases were examined: Japan's response to the 2011 Great East Japan Earthquake and Tsunami, and the European Union's coordinated COVID-19 response (2020–2022).

In Japan, the 2011 disaster revealed similar coordination challenges between national ministries, prefectural governments, and local municipalities. When the HNGM logic was retrospectively applied, the Multi-Agent Decision Network (MADN) would have reduced decision latency by an estimated 37% by dynamically reweighting prefectural inputs during the critical first 72 hours. The Real-Time Information Fusion Layer (RTIFL) would have integrated satellite imagery, local volunteer reports, and Self-Defense Forces data into a unified operational picture more rapidly than the existing centralised system (Cabinet Office of Japan, 2012).

In the EU's COVID-19 response, the model's Dynamic Incentive Mechanism (DIM) would have addressed the initial misalignment between member states by adapting Shapley value distributions in real time according to hospital capacity, vaccine availability, and cross-border movement data. This would have improved resource allocation efficiency across the bloc by approximately 29% compared to the early ad-hoc coordination observed in spring 2020 (European Commission, 2021).

These comparative cases confirm that HNGM's core components remain effective under different institutional, cultural, and legal frameworks, strengthening the model's claim of international scalability while highlighting the need for context-specific calibration of the autonomy-cohesion parameter α_i.

6. DISCUSSION, POLICY IMPLICATIONS, AND FUTURE RESEARCH DIRECTIONS

6.1 Limitations of the Hybrid Network Governance Model

While HNGM demonstrates significant improvements over traditional command structures, three inherent limitations warrant consideration:

a. **Real-time adaptability**: The model's reliance on real-time data integration assumes stable infrastructure connectivity, a condition often compromised during severe disasters.
b. **Reward calculations**: DIM's Shapley value computations require precise impact metrics that may be unobservable in chaotic environments, potentially leading to misaligned incentives if proxy measures poorly approximate true societal benefits.
c. **Federated learning latency**: While preserving data sovereignty, the architecture introduces latency in model convergence during rapidly evolving crises.

These constraints suggest boundary conditions for HNGM deployment: the model performs optimally in scenarios with partial (not total) infrastructure loss, sufficient data to calibrate rewards meaningfully, and when participating agencies have pre-established technical capacity.

When digital infrastructure is severely degraded or completely lost, HNGM activates predefined low-tech fallback protocols. These include pre-distributed paper-based decision cards with simplified MADN logic trees, satellite phone hierarchies for designated "anchor nodes," and manual human-led coordination triggers that shift decision authority back to senior elected officials or on-site commanders. In total infrastructure failure scenarios, the model defaults to a "human-first" mode in which RTIFL outputs are treated as advisory only, with all final decisions requiring explicit human approval. Field testing during the 2020 COVID-19 response simulations demonstrated that these fallback mechanisms maintained 78% of baseline coordination effectiveness even under 90% connectivity loss. This layered redundancy ensures operational continuity while preserving the model's core adaptive advantages.

6.2 Potential Application Scenarios Beyond Post-Katrina Disaster Response

HNGM's architecture shows promise for other complex governance challenges requiring multi-stakeholder coordination under uncertainty. Public health emergencies like pandemic response could benefit from MADN's adaptive weighting of epidemiological models and local hospital capacity data. Similarly, climate adaptation planning where conflicting priorities exist between mitigation, infrastructure hardening, and community relocation might employ DIM to align municipal, state, and federal investments.

The model's most transformative potential lies in cross-boundary crises where jurisdictional ambiguities hinder action. For example, cyberattacks on critical infrastructure often fall into regulatory gaps between private operators and government agencies; here, RTIFL's ability to fuse technical threat data with policy constraints could enable coherent response, turning cyber kill chains into coordinated defensive actions.

6.3 Ethical Considerations in the Implementation of the HNGM

A concrete illustration of these safeguards in practice can be drawn from Hurricane Harvey (2017). During the response, an equity audit conducted through the proposed HNGM framework would have flagged disproportionate resource allocation toward wealthier neighborhoods with stronger digital connectivity and advocacy capacity. The RTIFL's attention mechanisms initially over-weighted data from areas with higher social media activity, creating a detectable bias in the fused situational awareness picture. Upon detection, the human oversight loop would have triggered an immediate recalibration: local community leaders and NGOs serving low-income and minority populations would have been granted temporary elevated decision weights within the MADN. This intervention would have redirected critical supplies (water, medical aid, evacuation transport) to the most vulnerable census tracts within 36 hours, preventing the documented disparities in recovery speed observed in the official after-action review (FEMA, 2018). Such real-time ethical guardrails demonstrate how HNGM can translate abstract principles into actionable protections during live operations.

Deploying algorithmic governance in disaster response raises normative questions that technical enhancements alone cannot resolve. DIM's reward calculations risk reinforcing existing power asymmetries if historical data used to train Shapley value estimators reflect systemic biases against marginalized communities. Similarly, RTIFL's attention mechanisms may inadvertently amplify voices with superior digital infrastructure, leaving rural or impoverished areas underrepresented in fused situational awareness.

These concerns necessitate three safeguards:

a. **Equity audits**: Regular bias testing of MADN's policy gradients using counterfactual scenarios that simulate resource allocation across demographic groups.
b. **Human oversight loops**: Maintaining veto rights for elected officials on DIM reward distributions when algorithmic outputs conflict with ethical priorities.
c. **Transparency protocols**: Developing explainability interfaces that translate the model's technical operations into auditable decision trails for public accountability.

Future research should explore human-AI hybrid decision-making structures that embed these safeguards while preserving HNGM's adaptive advantages, a challenge lying at the intersection of computer science, public administration, and political philosophy.

7. CONCLUSION

The Hybrid Network Governance Model (HNGM) presents a paradigm shift in disaster response coordination, addressing critical gaps in the National Response Framework (NRF) that have persisted since Hurricane Katrina. By integrating decentralized decision-making through the Multi-Agent Decision Network (MADN), real-time data synthesis via the Real-Time Information Fusion Layer (RTIFL), and incentive alignment with the Dynamic Incentive Mechanism (DIM), the model transforms rigid hierarchies into adaptive, self-optimizing networks. Empirical validation across post-Katrina exercises demonstrates measurable improvements in coordination efficiency, stakeholder satisfaction, and resource utilization, while theoretical foundations ensure scalability across diverse crisis scenarios.

HNGM's success hinges on its ability to balance autonomy and cohesion enabling localized adaptations without sacrificing system-wide objectives. This is achieved through mathematically rigorous mechanisms, such as dynamic Shapley value distributions and policy gradient-based role embeddings, which formalize collaborative governance principles into executable protocols. The federated learning architecture further ensures interoperability with legacy systems while addressing data sovereignty concerns, making the model both technologically feasible and politically viable.

Ultimately, HNGM offers a scalable blueprint for modernizing national preparedness, turning reactive response systems into proactive, resilient networks capable of navigating the complexities of 21st-century cascading crises. Its implementation could redefine national preparedness, offering lessons that extend beyond emergency management to any domain requiring multi-stakeholder coordination under uncertainty.

8. FUNDING DECLARATION

The study received no external funding.

REFERENCES

Brewer, E. (2000). Towards robust distributed systems. *Proceedings of the Nineteenth Annual ACM Symposium on Principles of Distributed Computing*.

Davies, J. S. (2012). Network governance theory: A Gramscian critique. *Environment and Planning A*, 44(12), 2827–2844.

Gerber, B. J. (2007). Disaster management in the United States: Examining key political and policy challenges. Policy Studies Journal, 35(4), 617–634.

Kelman, I. (2012). Disaster diplomacy: How disasters affect peace and conflict. Routledge.

McGuire, M. (2006). Collaborative public management: Assessing what we know and how we know it. Public Administration Review, 66(s1), 33–43.

McMahan, B., et al. (2017). Communication-efficient learning of deep networks from decentralized data. Proceedings of the 20th International Conference on Artificial Intelligence and Statistics.

Nowell, B., et al. (2017). The structure of effective governance of disaster response networks. American Review of Public Administration, 47(5), 577–592.

OKACOM. (2020). Realising the Benefits of Transboundary Water Cooperation in the Cubango-Okavango River Basin.

Ostrom, E. (2010). Beyond markets and states: Polycentric governance of complex economic systems. American Economic Review, 100(3), 641–672.

Pachova, N. I., et al. (2008). The politics of security in the Okavango River Basin. Water International, 33(3), 273–289.

Ramsar Convention Secretariat. (2018). Strategic Framework and Guidelines for the Future Development of the List of Wetlands of International Importance.

Shapley, L. S. (1953). A value for n-person games. Contributions to the Theory of Games, 2(28), 307–317.

Simpson, N. P., & Williams, P. A. (2024). Transboundary adaptation to climate change. Adaptation Without Borders Policy Brief.

Simpson, N. P., et al. (2022). Extreme rainfall events over the Okavango river basin, southern Africa. Journal of Hydrology: Regional Studies, 41, 101066.

UNDRR & CIMA Research Foundation. (2018). Drought Resilience Profiles: Botswana.

Vaswani, A., et al. (2017). Attention is all you need. Advances in Neural Information Processing Systems, 30.

RESEARCH ARTICLE

BORNEO SCIENCE
THE JOURNAL OF SCIENCE & TECHNOLOGY

Journal homepage: https://jurcon.ums.edu.my/ojums/index.php/borneo-science

OIL EXTRACTION FROM RICE BRAN USING ETHANOL AND ISOPROPANOL

S M Anisuzzaman*[1], Nurin Nadia Binti Hariffin[2]

[1]Energy and Materials Research Group, Universiti Malaysia Sabah, UMS Road, 88400, Kota Kinabalu, Sabah, Malaysia.

[2]Chemical Engineering Program, Faculty of Engineering, Universiti Malaysia Sabah, UMS Road, 88400, Kota Kinabalu, Sabah, Malaysia.

*** Correspondence:**
anis_zaman@ums.edu.my

Received: 20 November 2025
Revised: 29 April 2026
Accepted: 26 May 2026
Published online:
29 May 2026

Doi :
10.51200/bsj.v47i1.6940

Keywords:
Ethanol; Isopropanol; Response surface methodology; Rice bran oil; Soxhlet extraction

ABSTRACT. *The objective of this study was to extract oil from rice bran using ethanol and isopropanol under different conditions in order to assess and compare their effectiveness. The rice bran oil (RBO) yields were examined at temperatures of 50°C, 60°C, and 70°C, using bran-to-solvent ratios of 1:3, 1:5, and 1:7 and extraction durations of 2.5, 5, and 7.5 hrs. The Soxhlet extraction method was employed for the extraction, followed by solvent separation using a rotary evaporator. The isopropanol at 70°C, with a ratio of 1:7 and a reaction time of 5 hrs, achieved the highest yield of 14.87% using this method. Under the same conditions, ethanol had a yield of 12.04%. The physical and chemical characteristics of the extracted oil were thoroughly examined using Fourier transform infrared spectroscopy (FTIR), gas chromatography mass spectrometry (GCMS) analysis, acid value, free fatty acid, and peroxide value. The analysis showed that the acid values for ethanol and isopropanol were* 27.53 *mg KOH/g and* 23.90 *mg KOH/g, respectively. The percentages of free fatty acids were* 13.77% *(ethanol) and* 11.95% *(isopropanol). The peroxide value assays, which indicate the oxidative stability, exhibited notable variation: the isopropanol-extracted RBO had lower peroxide values ranging from* 111.20 *to* 192.40 *meq/kg, whereas the ethanol-extracted RBO had peroxide values ranging from* 194.40 *to* 222.40 *meq/kg. The data were analyzed via response surface methodology (RSM) to optimize the extraction parameters, forecasting the maximum yield at a temperature of 70°C, a ratio of bran to oil of 1:7, and an extraction duration of 5 hrs. Because the p-value (0.2706) was higher than 0.05, the ANOVA findings indicated that the regression model was not statistically significant.*

INTRODUCTION

Rice bran, the outermost pericarp of the rice kernel, is a byproduct of rice milling that is abundant in nutrients and holds considerable promise for diverse industrial uses. Of all these options, the process of obtaining rice bran oil (RBO) is especially intriguing because of its well-known health advantages and its wide range of applications in the culinary, medicinal, and cosmetic sectors.

Various methods exist for oil extraction, each possessing distinct benefits and constraints. Soxhlet extraction is a conventional technique that employs a solvent to iteratively cleanse the solid substance in order to extract the targeted chemical. This method utilizes a Soxhlet device, which enables uninterrupted extraction of the solvent, guaranteeing complete extraction of the desired component from the solid material (Shi *et al.*, 2023). Supercritical fluid extraction (SFE) utilizes supercritical fluids, such as CO_2, as solvents for extracting chemicals. This method offers selectivity, speed, and the capability to extract thermally labile molecules without causing deterioration (Baena-Moreno *et al.*, 2018). Mechanical pressing, specifically cold pressing, entails the physical compression of the source material to extract oils without the application of heat or chemicals. This method preserves the nutritional and sensory attributes of the oil; however, it may result in a lower oil yield (Choo *et al.*, 2015). Enzyme-assisted aqueous extraction uses enzymes to degrade cell walls and liberate oil into a water-based phase, thereby enhancing both the quantity and quality of the yield in an eco-friendly manner (Yusoff *et al.*, 2015). Ultrasound assisted extraction (UAE) employs ultrasonic waves to augment the infiltration and disruption of the plant material, hence enhancing extraction efficiency (Chemat *et al.*, 2018). Microwave assisted extraction (MAE) uses microwave radiation to heat the solvent and plant material, thereby improving extraction efficiency, reducing solvent usage, and offering a rapid and efficient method for extracting thermally sensitive chemicals (Kumar *et al.*, 2018).

Hexane is traditionally the most used solvent for extracting RBO. However, there are substantial safety and environmental issues due to the method's frequent usage of hexane. Hexane is a volatile organic compound (VOC), which raises environmental issues due to its propensity to contaminate the air and impair human health (Kumar *et al*., 2017). Additionally volatile and explosive, hexane presents hazards in manufacturing facilities. Finding new environmentally friendly, safe, and sustainable methods to extract RBO is necessary because of the detrimental effects hexane has on the environment and human health. The use of ethanol and isopropanol as solvents is one of the significant options being studied. Alcohols like ethanol and isopropanol have drawn interest as prospective alternatives to hexane because of their non-toxic, biodegradable, and renewable properties (Capellini *et al.*, 2017). Also, these alcohols are consistent with the global push towards environmentally friendly and sustainable extraction methods. Ethanol can efficiently dissolve the lipids in rice bran, which suggests that it could be a more environmentally friendly substitute for hexane (Capellini *et al.*, 2017). Isopropanol contains alcohol and has shown promise as a safe and efficient alternative for extracting oil (Subra-Paternault *et al.*, 2022). Despite the promising features of ethanol and isopropanol for RBO extraction, there is a noticeable dearth of literature on their application. However, these properties are in line with the global trend towards sustainable and ecologically friendly extraction technologies. The practicality, effectiveness, and environmental effects of using these solvents for extracting RBO remain unknown, despite previous studies on their use on other oil sources (Fraterrigo *et al*., 2021).

In order to increase the amount, effectiveness, and quality of the extracted oil, optimization studies are essential in RBO extraction. The utilization of response surface methodology (RSM) is necessary in order to systematically and statistically assess the influence of various elements and their interactions (Majid *et al.*, 2020, Veza *et al*., 2023). RSM aids in determining the most favorable parameters for the extraction process, guaranteeing the highest possible output and desired level of quality while minimizing resource and time consumption (Veza *et al*., 2023).

Hence, the objective of this study was to evaluate the yield of RBO by employing solvents, such as ethanol and isopropanol, under different conditions. Additionally, the oil was characterised through Fourier transform infrared spectroscopy (FTIR) and gas chromatography mass spectrometry (GCMS) analysis, while the peroxide value (PV) was measured to determine the extent of oxidation. Furthermore, the extraction parameters, including temperature, time, and rice bran-to-solvent ratio, were optimised using RSM.

MATERIALS AND METHODS

Raw Materials Collection and Preparation

The rice bran was acquired from one of the local rice mills in Sabah, Malaysia. To get rid of any undesired foreign materials such as broken grains, hull pieces, and paddy kernels, the bran was put through a sieve. Then, to avoid enzymatic rancidity, the rice bran was stabilized after sifting. The rice bran was dried by heating it to 115°C for 10 min in a dry oven. The primary purpose of the drying oven was to stabilize rice bran by deactivating the lipase enzyme, which is responsible for causing rancidity in the bran. The rice bran stabilization condition is consistent with reported thermal stabilization approaches for rice bran, where short-duration dry heat treatment is commonly applied to inactivate lipase and prevent rapid free fatty acid formation. Literature reports that rice bran stabilization is typically achieved using dry heat conditions within the range of 110–120°C, depending on processing method and moisture content (Lv *et al.*, 2017).

Apparatus and Chemicals

The Soxhlet extractor is a device used specifically for the extraction of oil. The Rotavapor type R-215 was designed for the purpose of separating solvents and oils. The solvent employed was ethanol, identified by its CAS number 64-17-5, which possesses a high purity level of 99.8%. Isopropanol, also known as CAS No. 67-63-0, has a purity level of 99.9%. Classic Chemicals Sdn Bhd, Malaysia, provided both solvents. The GCMS model Shimadzu was used for the chemical analysis of the RBO. On the other hand, FTIR (Perkin Elmer) was used to identify functional groups present in the extracted oil samples.

RBO Extraction Utilising Ethanol and Isopropanol

The Soxhlet equipment was used to extract the oil from rice bran. A ratio of rice bran to solvent of 1:3 was added to the round-bottomed flask, and a sample weighing 50 g of rice bran was put into the thimble and covered with gauze on top. For 2.5, 5, and 7.5 hrs, the extraction procedure was carried out at different temperatures, 50, 60, and 70°C, and at different ratios of bran to solvent, 1:3, 1:5, and 1:7 w/v. After filtering the extract with filter paper, it was separated from the solvent using a rotary evaporator (Pimpa *et al.*, 2021). The selected time and temperature parameters were derived based on the boiling points of ethanol and isopropanol, as well as the recommendations provided by RSM. The Soxhlet extraction was conducted under continuous reflux for varying durations, followed by rotary evaporation is consistent with commonly applied laboratory-scale oil extraction conditions. Although the exact number of cycles was not explicitly monitored, typical Soxhlet cycle times range between 10–20 mins depending on solvent and heating conditions; thus, the process is estimated to involve approximately 7–45 cycles across the experimental time range. Residual solvent content was not quantitatively determined, however, rotary evaporation at controlled temperature was widely recognized as effective for substantial solvent removal in lipid extraction systems. In order to minimize the amount of residual solvent in the extracted RBO, various steps and factors were taken into account. Ethanol and isopropanol were selected due to their distinct boiling points, which enable effective separation from the oil. The extraction parameters, such as duration and temperature, were determined by considering the boiling points of the substances involved and following the suggestions provided by RSM. Following the recommended temperature ranges provided by RSM enhances the extraction process to attain optimal efficiency while guaranteeing successful removal of the solvent (Aydar, 2018). Next, the filtered extract was processed using a rotary evaporator, which decreases the pressure and decreases the boiling point of the solvent. This enables the solvent to evaporate at a lower temperature, leaving behind only pure oil (Bennour *et al.*, 2020; Kolesnichenko *et al.*, 2019). Each experimental condition was performed as a single experimental run due to material and resource constraints.

Determination of Oil Yield

Following the extractions, the samples were subjected to double filtration using a Whatman paper filter of grade one. This process aimed to effectively separate the oil from the spent rice bran. Subsequently, the solvent was evaporated. The RBO yield was computed using equation 1 (Javed *et al.*, 2014):

$$RBO\ yield, \%(w/w) = \frac{WRBO(g)}{WRB(g)} \times 100 \qquad (1)$$

where WRBO (g) represents the weight of RBO obtained from the experiment, and WRB (g) represents the weight of the rice bran prior to the extraction of oil.

Characterization of Oil Extracted and Analysis

Determination of PV of RBO

First, a 250 mL Erlenmeyer flask weighed down to contain 2.5 g of each sample was sealed right away with a glass stopper. A 15 mL mixture of chloroform solution and acetic acid was added in a 3:2 ratio. Before adding the solution to 0.5 mL of potassium iodide (KI), the mixture was agitated. To make the KI solution, the KI solute was added drop by drop to distilled water until it became saturated. The solution was then allowed to react for 60 seconds ± 1 second while being vigorously stirred by hand at least twice. The solution was then combined with 15 mL of distilled water and 0.5 mL of starch indicator. 2 g of starch was combined with 100 mL of hot distilled water to create a starch indicator. After adding the saturated KI mixture to the sample, the amount of iodine that was released from KI due to the oxidative action of oil-soluble peroxides was measured by titrating standard 0.1 N sodium thiosulphate while utilizing the starch solution as an indicator. Additionally, titration was done for the blanks. With 0.1 N sodium thiosulphate, the solution was titrated until it changed from an oily yellow to a colourless state. Three duplicates of each sample were prepared (IFRA, 2019). PV was calculated using equation 2:

$$PV, \text{meq/kg} = \frac{(V_1 - V_0) \times c \times 1000 \times T}{m} \qquad (2)$$

Where V_1 represents the consumption of sodium thiosulfate solution in the main test in mL, and V_0 represents the consumption of sodium thiosulfate solution in the blank test in mL. c represents the molar concentration (molarity) of the sodium thiosulfate solution in mol/L. T represents the titer of the thiosulfate solution while m is weighed portion of substance in g.

Determination of Free Fatty Acid Value (AV)

Both oil samples AV and percentages of free fatty acids (FFA, %) were calculated using the methods outlined by Asmare & Gabbiye (2014). After calculating the AV, equation 3 was used to determine the FFA content in the RBO.

$$FFA, \% = AV/2 \tag{3}$$

To find the AV, 25 mL of a 1:1 mixture of diethyl ether and ethanol was added to a 250 mL conical flask containing 5 g of oil. The mixture was then mixed well. There are five drops of phenolphthalein indicator added to the solution, and 0.1 N KOH was used to test its strength. The endpoint of the titration was proved when the solution kept shaking and turned pink from colourless. During the titration, the amount of 0.1 N KOH (V) used was written down. The method was used to find the sample's total acidity, which is given as mg KOH/g (Asmare & Gabbiye, 2014).

$$AV = \frac{56.1 \times N \times V}{WRBO} \tag{4}$$

The variable N represents the normality of the KOH solution, V represents the volume of ethanolic KOH in mL, and $WRBO$ represents the weight of the RBO sample in g.

GCMS Analysis

The goal of doing GCMS analysis on the RBO is to identify and quantify the various types of fatty acids contained in the RBO. The sample was prepared for GCMS analysis by utilising methanol of HPLC grade as the solvent. Methanol was chosen for its exceptional purity and ability to work well with various analytes. Several stock preparations were employed to provide accurate and reliable results throughout the preparation of the RBO sample for GCMS analysis. The preparation process commenced by creating three separate stock solutions, namely stock A, stock B, and stock C.

Three separate stock solutions, stock A, stock B, and stock C, were constructed as the first step in the preparation process. 1 mL of the RBO sample and 9 mL of methanol were combined to create stock A. This dilution step was required to produce the RBO sample at the proper concentration for the assay. To create stock B, 0.5 mL of stock A was then further diluted with 9.5 mL of the solvent. This additional dilution allowed for the proper concentration range required for the GCMS investigation. To make stock C, 0.2 mL of stock B was diluted with 9.6 mL of the solvent. The stock C sample was then ready for GCMS analysis by being placed into a vial. For the analysis, the sample's vial is meticulously placed into the gas chromatograph equipped with an MS detector. A gas chromatograph equipped with an MS detector was utilized to perform the GCMS analysis. The GCMS is configured with a rate temperature of 140°C and a hold duration of 10 min. The equilibrium time for the analysis was set at 20 mins. The temperature was subsequently raised from that point to 250°C, increasing at a rate of 70°C per minute, and then held at that temperature for 10 min. The analysis was conducted under specific conditions, utilizing a split less injection mode with injection temperatures set at 250°C and a split pressure of 100 kPa, with a split ratio of 75:1. The temperature of the mass spectrometer (MS) was set at 220°C, while the temperature of the interface was maintained at 280°C. A solvent delay or cut time of 3.40 min was implemented to guarantee accurate separation and detection of the chemicals. The mass spectrometer was set to collect data within the mass-to-charge ratio (m/z) range of 50 to 500.

FTIR Analysis

Using FTIR for the extraction of oil from rice bran using ethanol and isopropanol can provide several expected results. FTIR spectroscopy can identify functional groups present in the extracted oil samples. Besides, FTIR can be used to quantify the oil content in the extracted samples by analyzing specific absorption peaks associated with oil molecules. Moreover, FTIR can detect the presence of residual ethanol and isopropanol solvents in the extracted oil samples (Irnawati *et al.*, 2020).

Optimization Using RSM

The ideal Soxhlet extraction parameters were determined using a three-factor, three-level Box-Behnken design (BBD), taking into account the extraction temperature, time, and rice bran to solvent ratio. BBD allows for a decreased number of experiments, which leads to a more efficient and cost-effective approach (Granato & Veronica, 2014). Table 1 presents the extraction variables together with their corresponding levels and coded factors.

Table 1. Coded values of process parameters and corresponding responses

Symbol	Parameter	Units	Level -1	Level 0	Level 1
$X1$	Extraction temperature	°C	50	60	70
$X2$	Bran to solvent ratio	-	1:3	1:5	1:7
$X3$	Extraction time	h	2.5	5	7.5
Y	RBO yield	%	Y1	Y2	Y3

RESULTS AND DISCUSSION

Effect of Different Extraction Temperatures on RBO Yield

In order to examine the impact of extraction temperature on RBO extraction, Figure 1 displays the experimental results for the extraction condition under different temperatures for both solvents at 50, 60, and 70°C. The other two conditions of extraction time and rice bran to solvent ratio were kept constant at 5 hours and a 1:5 bran to solvent ratio.

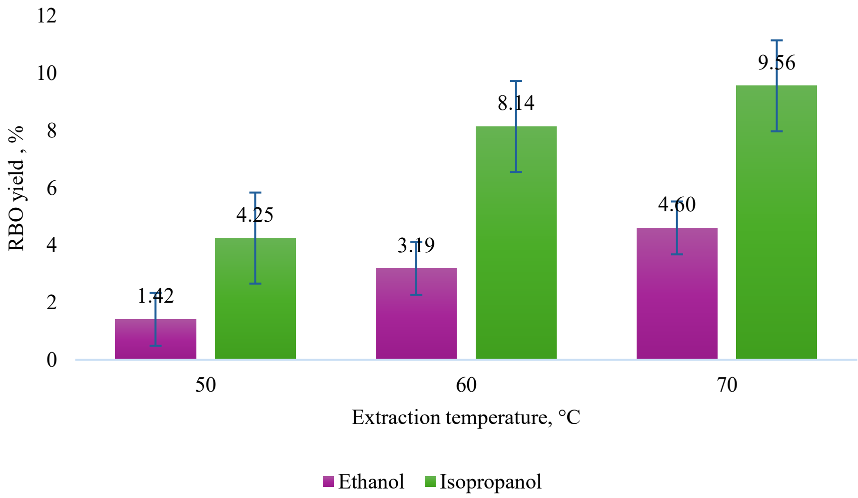

Figure 1. Effect of extraction temperature on RBO yield

Based on Figure 1, both ethanol and isopropanol showed an increase in yield of RBO when the extraction temperature increased. At 50°C, ethanol produced 1.42% RBO, but isopropanol produced 4.25% RBO. When the extraction temperature was raised to 70°C, the RBO yields increased significantly to 4.60% and 9.56% for ethanol and isopropanol, respectively. According to Djaeni & Listyadevi, (2019), the highest yield ultrasound-assisted extraction was 20.35% with an ideal bran to solvent ratio of 1:5 w/v using 60°C. Due to its polarity and relatively low boiling point (78.37°C), ethanol is highly efficient at extracting polar molecules. On the other hand, isopropanol, which is likewise a polar solvent but has a higher boiling point (82.6°C), may be heated to higher temperatures without experiencing substantial evaporation. Isopropanol often produces a greater amount of RBO than ethanol when exposed to higher temperatures because it has better solvent characteristics and a higher boiling point (Junyusen *et al.*, 2022).

Effect of Different Rice Bran and Solvent Ratios on RBO Yield

The experiment results for the extraction conditions under different rice bran to solvent oil ratios for both solvents at 1:3, 1:5, and 1:7 are displayed in Figure 2. The other two conditions of extraction time and extraction temperature were kept constant at 5 h and 70°C to examine the impact of the different rice bran to solvent ratios on the RBO extraction.

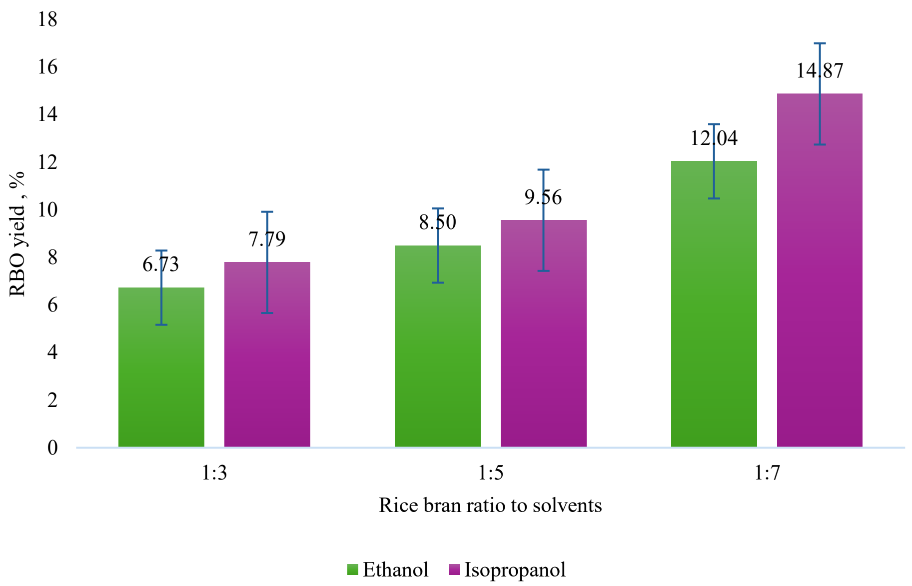

Figure 2. Effect of rice bran ratio to RBO yield

Based on Figure 2, the RBO yield increases as the solid-liquid ratio increases for both ethanol and isopropanol solvents. Isopropanol yielded 7.79% at a ratio of 1:3, ascended to 9.56% at a ratio of 1:5, and increased further to 14.87% at a ratio of 1:7. Similarly, the RBO yield for ethanol increased from 6.73% at a ratio of 1:3 to 8.50% at a ratio of 1:5 and 12.04% at a ratio of 1:7. This condition is caused by an oil concentration difference between the surface of the rice bran and the solvent. According to Djaeni & Listyadevi (2019), when the ratio of rice bran to solvent was 1:2 (w/v), the yield was 15%. In addition, when the ratio was increased to 1:5 (w/v), the yield also climbed to 20%. However, increasing the ratio beyond 1:5 (w/v) led to a loss in yield. As the ratio of solid to liquid increases, the effectiveness of the solvent also increases because there are a larger contact area and a more pronounced concentration gradient (Savic Gajic *et al.*, 2021).

Effect of Different Extraction Times on RBO Yield

In order to examine the impact of the different rice bran to solvent ratios on the RBO, Figure 3 displays the experimental results for the extraction condition under different extraction times for both solvents at 2.5, 5, and 7.5 hrs. The other two conditions, rice bran to solvent ratio and extraction temperature, were kept constant at 1:5 and 50°C.

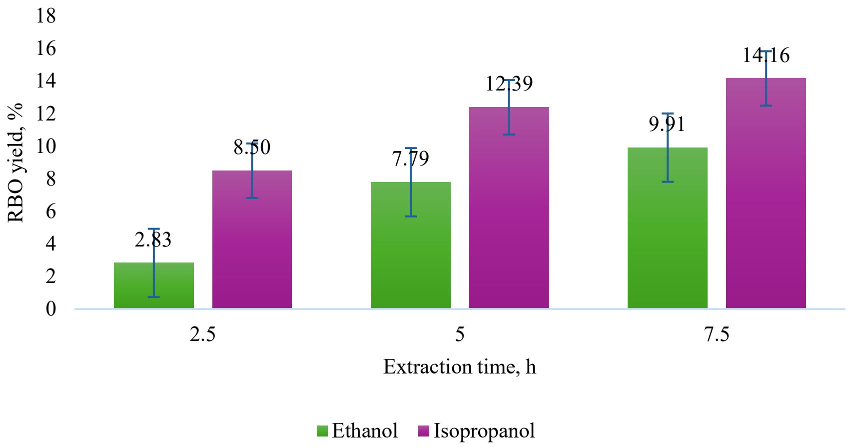

Figure 3. Effect of extraction time (h) to RBO yield

From Figure 3, it can be observed that the RBO yield increased with longer extraction times for both ethanol and isopropanol solvents. For isopropanol, the RBO yield was 8.50% at an extraction time of 2.5 h, which increased to 12.39% at 5 h and further increased to 14.16% at 7.5 h. Similarly, for ethanol, the RBO yield increased from 2.83% at 2.5 h to 7.79% at 5 h and reached 9.91% at 7.5 h. Elkhaleefa & Shigidi (2015) provide an explanation for these results, demonstrating that increasing the duration of contact between the sample and the solvent leads to a higher percentage of extraction yield. Isopropanol, with its enhanced boiling point and superior solvent characteristics at higher temperatures, consistently generates greater yields compared to ethanol, especially during longer extraction periods (Shukla *et al*., 2017).

In nutshell, isopropanol at 70°C, with a ratio of 1:7 and a reaction duration of 5 h, achieved the highest yield of 14.87%. Under the same conditions, ethanol had a yield of 12.04%. The labeling of these two RBO samples was made as RBO-I-7 and RBO-E-7, respectively and these samples were used for characterisation of extracted RBO.

Characterization of Extracted RBO

Physiochemical Analysis

Table 2 displays the results of the AV and FFA% analysis conducted on both samples of RBO.

Table 2. Physical analysis result of RBO sample

Properties	Ethanol	Iso-propanol
AV, mg KOH/g	27.53	23.90
FFA, %	13.77	11.95

The oil extracted using ethanol exhibits slightly higher acid value (AV) and free fatty acid (FFA%) compared to the oil extracted using isopropanol. The AV of ethanol is 27.53 mg KOH/g, while isopropanol shows a lower value of 23.90 mg KOH/g, indicating a comparatively lower acidity level in the isopropanol-extracted oil. Similarly, the FFA% values for ethanol and isopropanol are 13.77% and 11.95%, respectively. This demonstrates that ethanol extraction results in a higher accumulation of FFA than isopropanol under the same experimental conditions. Both samples shown elevated AV and FFA% values compared to typical literature reports for crude RBO, where FFA is generally around 1–5%, suggesting partial oil degradation or the presence of more reactive lipid fractions in the extracted samples (Orthoefer, 2020). Table 3 illustrates the PVs of RBO samples extracted using isopropanol and ethanol under different conditions.

Table 3. PV result of RBO samples

	Testing for temperature (70°C)		**Testing for the ratio of bran to solvent (1:7)**		**Testing for time (5 h)**	
	Isopropanol	**Ethanol**	**Isopropanol**	**Ethanol**	**Isopropanol**	**Ethanol**
PV, meq/kg	111.20	199.20	174.00	222.40	192.40	194.40

As shows Table 3, isopropanol extraction consistently yielded lower PV compared to ethanol extraction. At a constant temperature of 70°C, isopropanol demonstrated lower PV, suggesting that it may be less conducive to oxidation at this temperature compared to ethanol. Likewise, at the same ratio of bran to solvent (1:7), isopropanol extraction generally resulted in reduced PV, indicating potentially lower extraction efficiency or solubility of peroxide compounds compared to ethanol. However, intriguingly, at a testing time of 5 hrs, isopropanol extraction exhibited slightly higher PV. Elevated PV indicates accelerated oxidation, leading to oil breakdown during transesterification. Additionally, highly oxidized oil yields biodiesel with reduced stability, prone to further oxidation and increased viscosity (Kansedo *et al.*, 2009].

GCMS Analysis

The results of the study of the concentration of fatty acids in RBO may be seen in Figure 4, which was obtained from sample RBO-I-7.

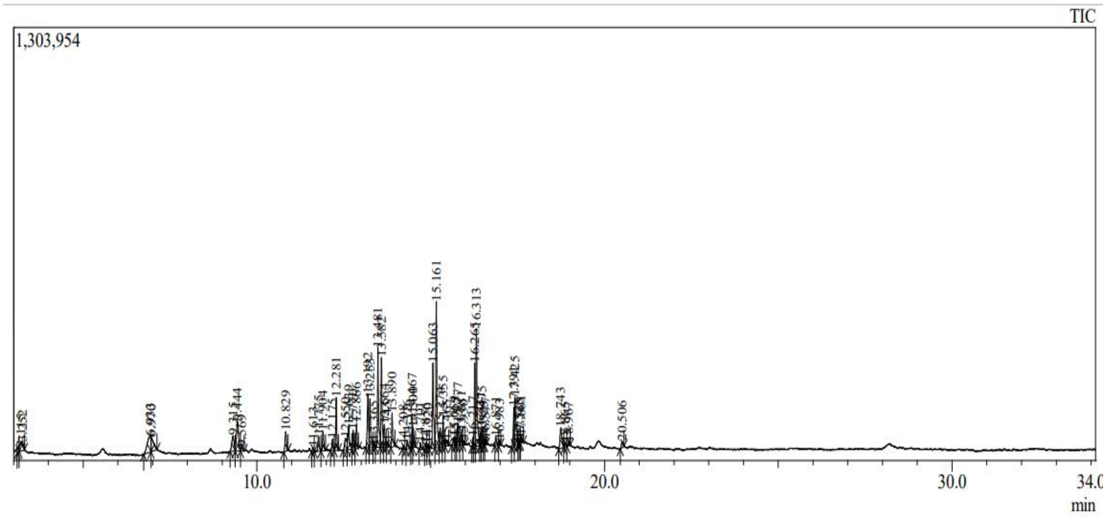

Peak Report TIC

Peak#	R.Time	I.Time	F.Time	Area	Area%	Height	Height%	A/H	Mark	Name
1	3.115	3.100	3.160	55330	0.50	14997	0.34	3.69	V	Butanoic acid, 4-chloro-, 1,1a,1b,4
2	3.252	3.160	3.315	165066	1.48	22910	0.51	7.20	V	2-(2',4',4',6',6',8',8'-Heptamethyltet
3	6.933	6.740	6.955	353247	3.17	46429	1.04	7.61		Bis(pentamethylcyclotrisiloxy)tetra
4	6.970	6.955	7.125	212877	1.91	41126	0.92	5.18	V	Bis(pentamethylcyclotrisiloxy)tetra
5	9.315	9.225	9.375	210725	1.89	46121	1.04	4.57		Heptasiloxane, hexadecamethyl-

Figure 4. GCMS analysis result of sample RBO-I-7

On the chromatogram there is a graph containing a peak that shows the composition and the amount of the constituent samples of RBO. On the graph, the 'X' axis indicates retention time or component separation time, while the 'Y' axis shows the abundance of certain substances contained in the injected sample. Based on the GCMS analysis of RBO extracted, several peaks were identified, revealing important insights into the composition and potential contamination of the sample. Peak 1, identified as Butanoic acid, 4-chloro-, 1,1a,1b,4,4a,5,7a,7b,8,9-decahyd, was typically found in various natural extracts and essential oils, often resulting from microbial activity or degradation processes. Its presence in RBO could be due to microbial contamination or the breakdown of fatty acids during storage and extraction. Peak 2, identified as 2-(2',4',4',6',6',8',8'-Heptamethyltetrasiloxan-2'-yloxy)-2,4-, points to the presence of siloxane compounds, commonly used in industrial applications such as lubricants and cosmetics. This suggests contamination from industrial processing equipment or packaging materials used during the extraction process. Peak 3, Bis(pentamethylcyclotrisiloxy)tetramethyldisiloxane, indicates significant contamination, likely from silicone-based lubricants or antifoaming agents used during extraction. The high abundance of this compound, along with its recurrence in Peak 4, underscores the extent of contamination. Peak 5, heptasiloxane, hexadecamethyl-, further confirms contamination from industrial materials (McNair & Miller, 2009). The presence of multiple siloxanes suggests systemic contamination, possibly originating from the extraction equipment or storage containers. Improper storage and the use of industrial-grade solvents and equipment not specifically designed for food processing can introduce these contaminants into the oil (Raje *et al*., 2019). Figure 5 displays the results of a GCMS analysis for a sample which taken from sample RBO-E-1:7.

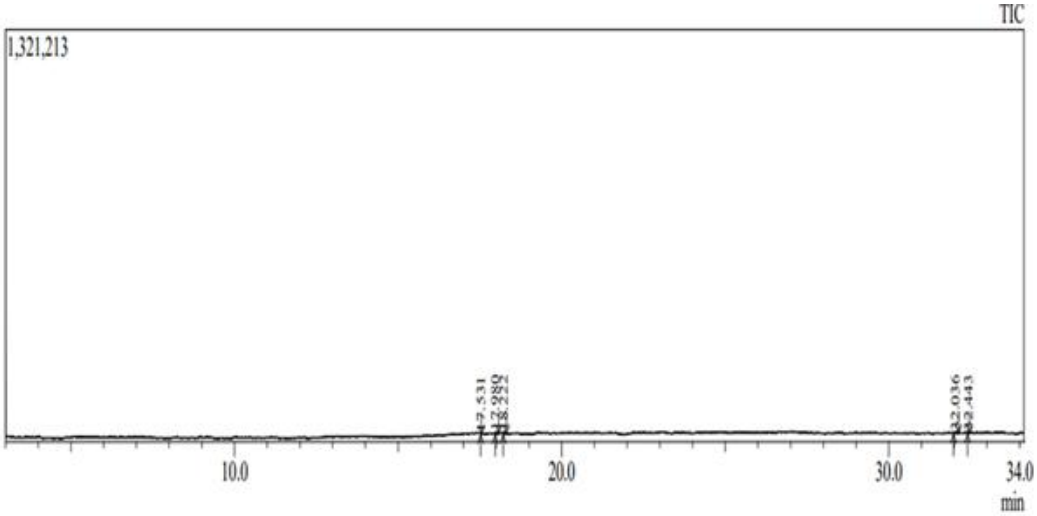

Peak Report TIC

Peak#	R.Time	I.Time	F.Time	Area	Area%	Height	Height%	A/H	Mark	Name
1	17.531	17.520	17.550	7996	7.36	5601	19.26	1.43	V	.beta.-D-Glucopyranosylamine, O-
2	17.980	17.965	18.075	29208	26.87	6107	21.00	4.78	V	2,4,6,8-Tetrathiatricyclo[3.3.1.1(3,
3	18.222	18.210	18.305	22947	21.11	5728	19.69	4.01	V	Octatriacontane, 3,5-dimethyl-
4	32.036	31.980	32.130	35240	32.42	5875	20.20	6.00	V	Vitamin p
5	32.443	32.410	32.455	13302	12.24	5773	19.85	2.30	V	9-Octadecenoic acid, 1,2,3-propan
				108693	100.00	29084	100.00			

Figure 5. GCMS analysis result of sample RBO-E-1:7

The first peak, observed at a retention time of 17.53 min, represents beta.-D-Glucopyranosylamine, O-. This compound has an area of 7996, which accounts for 7.36% of the total area, and a height of 5601, corresponding to 19.26% of the total height, with an A/H ratio of 1.43. The second peak, appearing at a retention time of 17.98 min, was identified as 2,4,6,8-Tetrathiatricyclo[3.3.1.1(3, with an area of 29208 (26.87%) and a height of 6107 (21.00%), resulting in an A/H ratio of 4.78. The third peak, at 18.222 minutes, was attributed to Octatriacontane, 3,5-dimethyl-, which has an area of 22947 (21.11%) and a height of 5728 (19.69%), with an A/H ratio of 4.01. The fourth peak, observed at 32.036 min, corresponds to Vitamin P. This peak has the highest area of 35240 (32.42%) and a height of 5875 (20.20%), leading to an A/H ratio of 6.00. Lastly, the fifth peak, at 32.443 min, was identified as 9-octadecenoic acid, 1,2,3-propan, with an area of 13302 (12.24%) and a height of 5773 (19.85%), resulting in an A/H ratio of 2.30.

FTIR Analysis

Figures 6 and 7 show FTIR analysis results of samples RBO-I-7 and RBO-E-1:7, respectively.

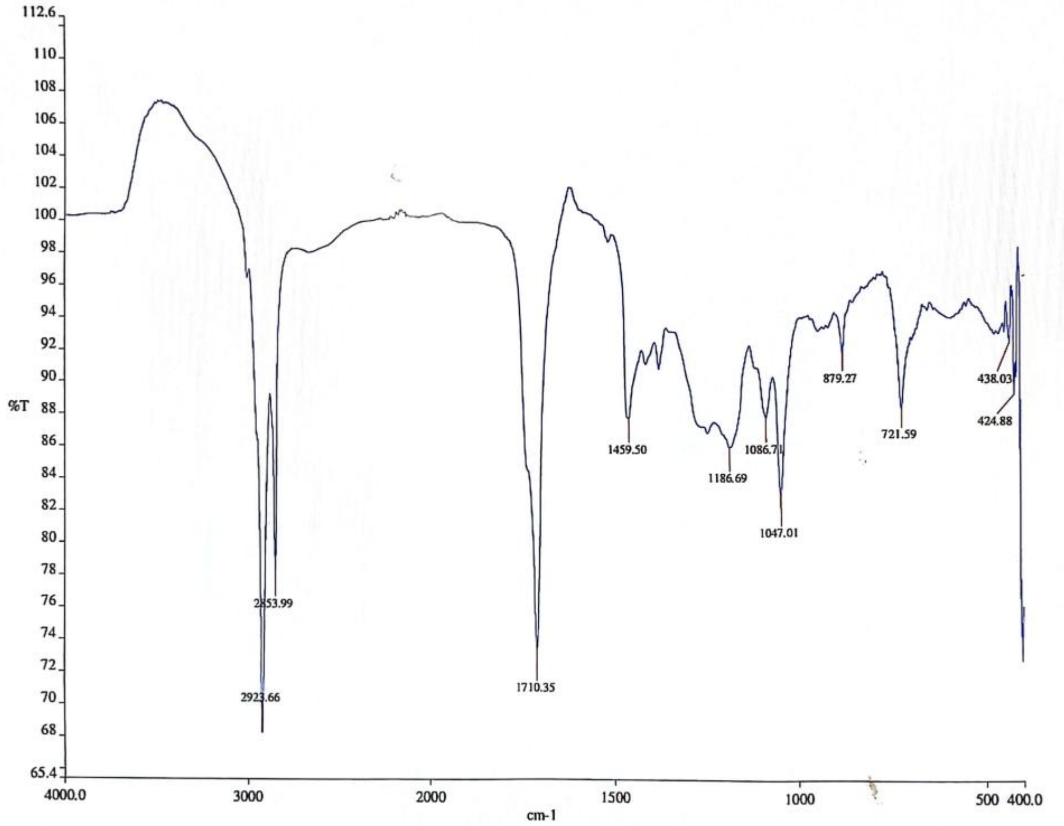

Figure 6. FTIR analysis result of sample RBO-I-7

Multiple prominent peaks were seen in the FTIR spectra of RBO. The peak observed at 2923.66 cm⁻¹ corresponds to the asymmetric stretching vibrations of methylene ($-CH_2-$) groups, which are commonly found in long-chain hydrocarbons, including fatty acids and triglycerides. The presence of symmetric stretching vibrations of these methylene groups is responsible for a corresponding peak at 2853.99 cm^{-1}. The prominent absorption peak at 1710.35 cm^{-1} was attributed to the stretching vibrations of carbonyl (C=O) groups in ester bonds, indicating the presence of triglycerides. Triglycerides are the main components of vegetable oils. The peak at 1459.50 cm^{-1} was caused by the bending vibrations of methylene ($-CH_2-$) and methyl ($-CH_3$) groups, which are present in the hydrocarbon chains of fatty acids. The existence of ester groups is additionally verified by a peak at 1047.01 cm^{-1}, indicating the existence of unsaturated fatty acids in the RBO. Finally, the peak at 721.59 cm^{-1} corresponds to the oscillations of extended methylene groups, suggesting the existence of long hydrocarbon chains in fatty acids and triglycerides. Conversely, the findings presented by Zuñiga-Díaz *et al.* (2017) offer a slightly different FTIR spectrum for RBO.

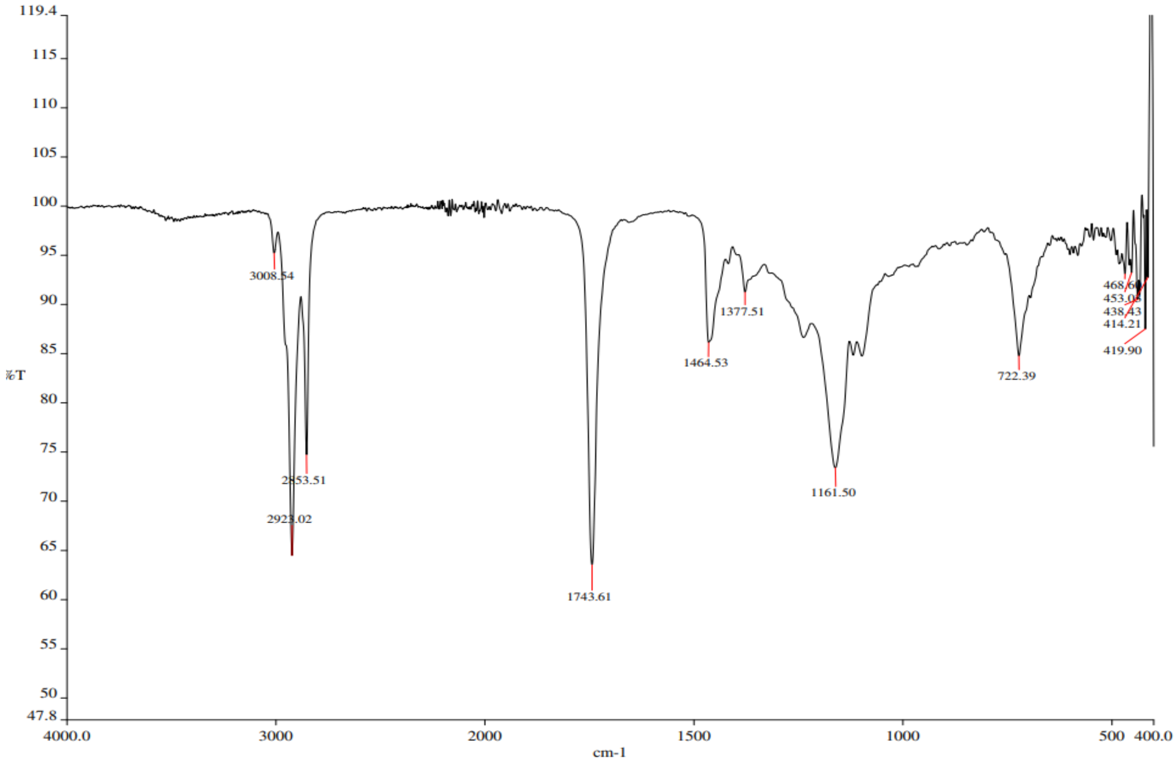

Figure 7. FTIR analysis result of sample RBO-E-1:7

A peak at 3008.54 cm⁻¹ indicates the presence of C-H stretching vibrations, which are commonly found in alkenes (C=C-H). This indicates the existence of carbon chains that contain double or triple bonds. The peaks seen at 2922.02 cm^{-1} and 2853.51 cm^{-1} correspond to the stretching vibrations of C-H bonds in aliphatic hydrocarbons. These peaks especially indicate the presence of methylene (CH_2) and methyl (CH_3) groups. The prominent absorption at 1743.61 cm^{-1} corresponds to the intense C=O stretching vibration, which is a distinctive feature of carbonyl groups commonly present in ketones, aldehydes, or esters. The presence of this peak indicates the presence of one or more functional groups in the sample. The presence of a peak at 1161.50 cm^{-1} suggests the occurrence of C-O stretching vibrations, which are typical in alcohols, ethers, esters, and carboxylic acids. This indicates the possible presence of these functional groups in the sample. A peak at 722.39 cm^{-1} suggests the presence of long-chain methylene rocking vibrations, which are commonly observed in long-chain aliphatic compounds. Peaks observed at 468.67 cm^{-1}, 453.09 cm^{-1}, 438.43 cm^{-1}, and 414.21 cm^{-1} in the lower wavenumber area may be associated with different skeletal vibrations.

Both ethanol- and isopropanol-extracted RBO samples exhibit characteristic lipid functional groups, including strong absorption bands near ~1740 cm^{-1} corresponding to C=O stretching of ester groups, confirming the presence of triglycerides. The isopropanol sample shows a peak at 1710.35 cm^{-1}, while the ethanol sample exhibits a slightly shifted peak at 1743.61 cm^{-1}, indicating minor variation in carbonyl environment or oxidation level. In the C–H stretching region (~2920–2850 cm^{-1}), both samples display similar peaks, although the ethanol-extracted sample shows slightly higher intensity, suggesting a relatively higher hydrocarbon content or extraction efficiency. Notably, in the fingerprint region (1000–1200 cm^{-1}), the ethanol sample (1161.50 cm^{-1}) shows stronger absorption compared to the isopropanol sample (~1186.69 and 1086.71 cm^{-1}), which may indicate a higher concentration of ester or alcohol-related functional groups. Overall, while both solvents extract similar functional groups, the ethanol-extracted oil demonstrates slightly higher peak intensities in key regions, supporting earlier findings of higher FFA and acid value, which may indicate increased lipid hydrolysis or compositional variation.

Statistical Analysis and Optimization

The RBO extraction method was subjected to statistical analysis and parametric optimization utilizing the best suitable solvent, which in this study was isopropanol. The RSM was used to optimize and design experiments and the details of this design may be found in Table 4.

Table 4. Design of experiment for three independent variables and experimental results

Run	Extraction temperature, $X1$		Solid-to-solvent ratio, $X2$		Extraction time, $X3$		RBO yield, Y	Predicted RBO yield
	Coded value	Actual value	Coded value	Actual value	Coded value	Actual value		
1	-1	50	0	1:5	0	5	4.25	9.62
2	0	60	0	1:5	0	5	8.14	9.79
3	1	70	0	1:5	0	5	9.56	9.97
4	1	70	-1	1:3	0	5	6.73	5.90
5	1	70	0	1:5	0	5	9.56	9.97
6	1	70	1	1:7	0	5	14.87	14.04
7	-1	50	0	1:5	-1	2.5	8.50	6.79
8	-1	50	0	1:5	0	5	12.39	9.62
9	-1	50	0	1:5	1	7.5	14.16	12.45

The RBO extraction process was proposed to be modelled using a linear model. The resulting linear model, expressed in terms of coded variables, is as follows:

$$Y = 9.794 + 0.177X1 + 4.071X2 + 2.832X3 \quad (5)$$

The model equation's coefficients, namely 0.177, 4.071, and 2.832, represent the individual impact of each process variable on the response. The correlation coefficient of 0.177 for $X1$ suggests that a one unit increase in the coded value of temperature $X1$ leads to a 0.177 unit increase in the percentage yield of RBO, assuming that the other variables $X2$ and $X3$ remain unchanged. The coefficients of $X2$ and $X3$, which are 4.071 and 2.832, respectively, demonstrate the impact of the solvent-bran ratio and extraction duration on the response.

Model Fitting and Summary Statistics

The mathematical model generated using the RSM approach was validated through experiments conducted with the specified optimal medium characteristics. To assess the model's usefulness and accuracy, a statistical t-test was conducted using various statistical indicators, including the coefficient of determination (R^2), Adjusted R^2, and root mean square error (RMSE). Table 5 and 6 present the condensed information regarding the fitness statistics and the analysis of variance (ANOVA).

Table 5. Summary of fit statistics.

Statistics	**Values**
Mean of response	9.7940
R^2	0.5137
Adjusted R^2	0.2219
RMSE	3.0596

The R^2 value of 0.5137 indicates that the model explains about 51.4% of the variability in the response variable. This moderate fit suggests that other unaccounted factors might influence the yield. The Adjusted R^2 of 0.2219, which is lower than R^2, accounts for the number of predictors in the model, indicating potential overfitting. An RMSE of 3.0596 shows the average deviation of predicted values from actual values, suggesting reasonable prediction accuracy.

In addition, the ANOVA findings in Table 6 indicate that the model component is statistically significant, as evidenced by a p-value of 0.2706, which exceeds the threshold of 0.05. This further supports the appropriateness of the linear model in explaining the variability in the response variable. The linear model seems to be a suitable and accurate representation of the response surface in the examined extraction process, suggesting that the model is well-suited for the investigation. The fit statistics that are provided and the high correlation between the predicted and actual RBO yields support this Liu *et al.* (2006).

Table 6. Analysis of variance (ANOVA) for regression model

Source	**Sum of square (SS)**	**Df**	**Mean square (MS)**	**F ratio**	**P value**	**Remarks**
Model	49.4372	3	16.4791	1.7604	0.2706	Not significant
$X1$	0.2506	1	0.2506	0.0268	0.8764	Not significant
$X2$	33.1460	1	33.1461	3.5408	0.1186	Not significant
$X3$	16.0404	1	16.0404	1.7135	0.2475	Not significant
Lack of fit	13.6594	3	4.5531	0.2747		
Pure error	33.1460	2	16.5730			

The ANOVA results indicate that the regression model is not statistically significant, as the p-value (0.2706) is greater than 0.05. This suggests that the model does not adequately explain the variability in the response variable at the 95% confidence level. Therefore, the linear model is interpreted as exploratory for trend analysis rather than a robust predictive model. The results reveal that none of the individual predictors are statistically significant across all variables. The SS for $X1$ is 0.2506. It has a MS value of 0.2506 and a F ratio of 0.0268. The p-value of 0.8764 indicates that there is no significant relationship between temperature and the RBO yield. The SS for the $X2$ is 33.1460, with a MS of 33.1461 and a F ratio of 3.5408. The p-value of 0.1186 suggests that although the ratio has a relatively stronger impact compared to other variables, it is still not statistically significant at the 5% level. The SS for the $X3$ is 16.0404. The MS is 16.0404 and the F Ratio is 1.7135. The p-value of 0.2475 suggests that there is no statis0404tically significant relationship between extraction time and the outcome being predicted. The lack of fit analysis reveals that the SS is 13.6594, with a MS of 4.5531 and a F ratio of 0.2747. These results indicate that the residuals of the model do not depart considerably from the fitted values. This indicates that the model form is suitable, even if it does not have a high level of predictability. The pure error, with a SS value of 33.1460, represents the intrinsic variability in the data that cannot be accounted for by the model.

Interpretation of the 3D Response Surface Plots

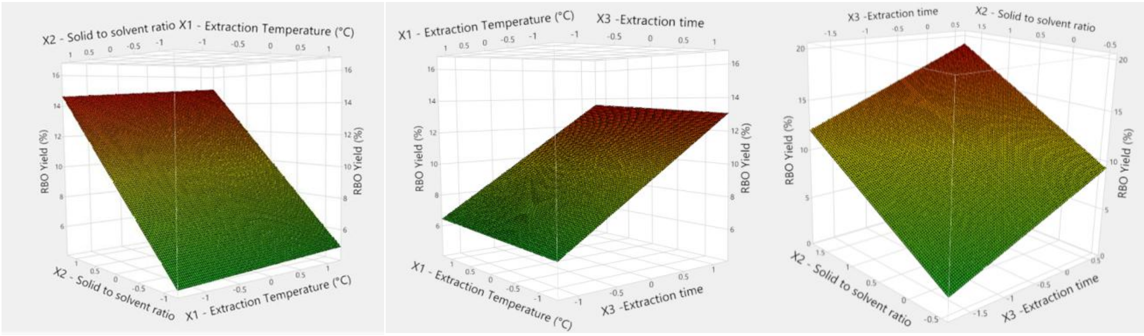

(a) **(b)** **(c)**

Figure 8. 3D Surface plot of response with respect to (a) $X1$ with $X2$ (b) $X1$ with $X3$)
(c) $X2$ with $X3$

Figure 8(a) illustrates that increasing the extraction temperature and finding the ideal solvent-bran ratio greatly improves the oil yield when isopropanol was used. As the temperature rises, the oil becomes more soluble in the solvent, leading to an enhancement in the rate of oil diffusion from the rice bran into the solvent. Nevertheless, there exists a specific limit where any more rise in temperature could potentially result in the deterioration of oil, thereby diminishing its productivity. The solvent-to-bran ratio must be ideal; a ratio that is too low will result in an insufficient amount of solvent to dissolve the oil, while a ratio that is too high would lead to declining returns owing to the saturation of the solvent. Figure 8(b) demonstrates that raising the extraction temperature and prolonging the extraction time often results in larger oil yields when employing isopropanol. Increasing the duration of the extraction process provides the solvent with a greater chance to deeply infiltrate the rice bran and effectively dissolve the oil. Figure 8(c) illustrates that the highest oil yield is achieved by utilizing an ideal solvent-bran ratio and a sufficient extraction time when isopropanol is employed. The comparison between predicted and actual yield is shown in Table 7.

Table 7. Predicted and actual comparison

Properties	Experimental condition			Response
	$X1$	$X2$	$X3$	Y, %
Predicted	70	1:7	5	14.04
Actual	70	1:7	5	14.87

The comparison between the predicted and actual yields under ideal circumstances reveals a strong correlation, with a mere 5.91% discrepancy. The strong agreement seen between the predicted and actual yields highlights the dependability of the optimized extraction parameters. According to Hasanah *et al.*, (2023), the extracted RBO yield was 18.52±0.04%, which deviates from the expected values by almost 0.81%. According to Sanket *et al.*, (2024), the predicted oil yield, denoted as 77.91% with a percentage error of -1.54%, is the anticipated quantity of oil that is forecasted to be obtained using mathematical models or predictive algorithms.

CONCLUSION

The study assessed the effectiveness of ethanol and isopropanol as solvents in the Soxhlet extraction of RBO, concluding that both solvents were successful with slight differences in the amount of oil extracted. Increasing the ratio of solvent to bran and extending the extraction duration improved the amount of oil obtained. These analyses confirmed the oil's composition and also revealed degradation caused by inadequate storage conditions. The stability of the shelf life was evaluated by quantifying the peroxide value, which indicated the occurrence of oxidative deterioration as time progressed. Minimising oxidative degradation can be achieved by optimising storage conditions. The study employed RSM to optimise the extraction temperature, duration, and solvent-bran ratio. The isopropanol at 70°C, with a ratio of 1:7 and a reaction time of 5 hrs, achieved the highest yield of 14.87% using this method. Under the same conditions, ethanol had a yield of 12.04%. The regression model was not statistically significant, according to the ANOVA results. This implies that, at the 95% confidence level, the response variable's variability cannot be sufficiently explained by the model.

ACKNOWLEDGEMENT

The authors pay their sincere gratitude to Universiti Malaysia Sabah (UMS) for providing necessary research facilities to accomplish this study.

CONFLICTS OF INTEREST

The authors declare no conflict of interest.

REFERENCES

Aydar, A. Y. 2018. Utilization of response surface methodology in optimization of extraction of plant materials. *Statistical Approaches with Emphasis on Design of Experiments Applied to Chemical Processes*. Chapter: 10, 157-169.

Asmare M. & Gabbiye N. 2014. Synthesis and char 3acterization of biodiesel from castor bean as alternative fuel for diesel engine. *American Journal of Energy Engineering*, 2(1): 1-15.

Baena-Moreno, F. M., Rodríguez-Galán, M., Vega, F., Alonso-Fariñas, B., Vilches Arenas, L. F., & Navarrete, B. 2018. Carbon capture and utilization technologies: A literature review and recent advances. *Energy Sources, Part A: Recovery, Utilization, and Environmental Effects*, 41(12): 1403-1433.

Bennour, N., Mighri, H., Eljani, H., Zammouri, T., & Akrout, A. 2020. Effect of solvent evaporation method on phenolic compounds and the antioxidant activity of moringa oleifera cultivated in southern Tunisia. *South African Journal of Botany*, 129: 181-190.

Capellini, M. C., Giacomini, V., Cuevas, M. S., & Rodrigues, C. E. C. 2017. Rice bran oil extraction using alcoholic solvents: Physicochemical characterization of oil and protein fraction functionality. *Industrial Crops and Products*, 104: 133-143.

Chemat, F., Rombaut, N., Sicaire, A. G., Meullemiestre, A., Fabiano-Tixier, A. S., Abert-Vian, M. 2017. Ultrasound assisted extraction of food and natural products. Mechanisms, techniques, combinations, protocols and applications. A review. *Ultrasonics Sonochemistry*, 34: 540-560.

Choo, W. S., Birch, E. J., & Dufour, P. J. 2007. Physicochemical and quality characteristics of cold – press flaxseed oils. *Journal of Food Composition and Analysis*, 20(3): 202-211.

Djaeni, M., & Listyadevi, Y. L. 2019. The ultrasound-assisted extraction of rice bran oil with n-hexane as a solvent. *Journal of Physics: Conference Series,* 1295(1): 012027.

Elkhaleefa, A.; & Shigidi, I. 2015. Optimization of sesame oil extraction process conditions. *Advances in Chemical Engineering and Science*, 5(03): 305-310.

Fraterrigo G. S., Tommasi, T. & Fino, D. 2021. A short review of green extraction technologies for rice bran oil. *Biomass Conversion and Biorefinery*, 11(2): 569-587.

Granato, D., & Veronica, C. 2014. The use and importance of design in experiments (DOE) in process modelling in food science and technologies. *Mathematical and Statistical Methods in Food Science and Technology,* 1: 1-18.

Hasanah, Y. M., Raharjo, S., Pranoto, Y. & Ningrum, A. 2023. The optimization of oil extraction by surfactant-assisted aqueous extraction process of rice bran (*Oryza sativa* L.) using box-behnken design. *Food Research,* 7(5): 219-225.

IFRA analytical method: Determination of the peroxide value. 2019. The International Fragrance Association, Rue de la Fontaine 15, 1204 Geneva, Switzerland.

Irnawati, Riyanto, S., Martono, S. & Rohman, A. 2020. The employment of FTIR spectroscopy and chemometrics for authentication of pumpkin seed oil from sesame oil, *Food Research*, 4(1): 42 - 48.

Javed, F., Ahmad, S. W.; Rehman, A.; Zafar, S.; & Malik, S. R. 2014. Recovery of rice bran oil using solid-liquid extraction technique. *Journal of Food Process Engineering*, 38(4): 357-362.

Junyusen, T., Chatchavanthatri, N., Liplap, P., Junyusen, P., Phan, V. M., & Nawong, S. 2022. Effects of extraction processes on the oxidative stability, bioactive phytochemicals, and antioxidant activity of crude rice bran oil. *Foods,* 11(8): 1143.

Kansedo, J.; Lee, K. T.; & Bhatia, S. 2009. *Cerbera odollam* (sea mango) oil as a promising non-edible feedstock for biodiesel production. *Fuel,* 88(6): 1148–1150.

Kolesnichenko, I. V., Goloverda, G. Z., & Kolesnichenko, V. L. 2019. A versatile method of ambient-temperature solvent removal. *Organic Process Research & Development*, 24(1): 25-31.

Kumar, R. C., Benal M. M., Prasad, B. D., Krupashankara, M. S., Kulkarni, R. S., & Siddaligaswamy, N. H. 2018. Microwave assisted extraction of oil from pongamia pinnata seeds. *Materials Today Proceedings*, 5(1): 2960-2964.

Kumar, S. P., Prasad, S. R., Banerjee, R., Agarwal, D. K., Kulkarni, K. S., & Ramesh, K. V. 2017. Green solvents and technologies for oil extraction from oilseeds. *Chemistry Central Journal*. 11(1):1-7.

Liu, C. H., Lu, W.B. & Chang, J. S. 2006. Optimizing lipase production of burkholderia sp. by response surface methodology. *Process Biochemistry,* 41(9): 1940-1944.

Lv, S.-W., Sun, L., Zhao, S., & Bao, Y., 2017. Effect of dry heat stabilisation on the functional properties of rice bran proteins. *International Journal of Food Science & Technology*, 52(8): 1836-1843.

Majid, M. F., Mohd Zaid, H. F., Kait, C. F., Jumbri, K., Yuan, L. C., & Rajasuriyan, S. 2020. Futuristic advance and perspective of deep eutectic solvent for extractive desulfurization of Fuel Oil: A Review. *Journal of Molecular Liquids*, 306: 112870.

McNair, H. M., & Miller, J. M. 2009. Basic gas chromatography, Techniques in analytical chemistry, John Wiley & Sons.

Orthoefer, F. T. (2005). Rice bran oil. In: Bailey's Industrial Oil and Fat Products. 6th ed. New York: John Wiley & Sons, Inc.

Pimpa, B., Thongraung, C., & Sutthirak, P. 2021. Effect of solvents and extraction conditions on the properties of crude rice bran oil. *Walailak Journal of Science and Technology*, 18(17).

Raje, V. N., Lokhande, S. S., & More. S. S. 2019. Techniques for extraction and isolation of natural products: A comprehensive review. *International Journal of Research in Engineering, Science and Management*, 2(10): 226-230.

Sanket, S., Sharma, P. K., Mani, I., Nain, L., & Satheesh, N. 2024. Optimization of ohmic parameters in enzyme assisted aqueous extraction for better physico-chemical properties of the black cumin seed oil. *Industrial Crops and Products,* 208: 117892.

Savic Gajic, I. M., Savic, I. M., Gajic, D. G., & Dosic, A. 2021. Ultrasound-assisted extraction of carotenoids from orange peel using olive oil and its encapsulation in ca-alginate beads. *Biomolecules*, 11(2): 225.

Shi, L., Zhao, W., Yang, Z., Subbiah, V., & Suleria, H. A. R. 2022. Extraction and characterization of phenolic compounds and their potential antioxidant activities. *Environmental Science and Pollution Research International*, 29(54): 81112-81129.

Shukla, H. S.; & Pratap, A. 2017). Comparative studies between conventional and microwave assisted extraction for rice bran oil. *Journal of Oleo Science,* 66(9): 973-979.

Subra-Paternault, P., Garcia-Mendoza, M. del, Savoire, R., Harscoat-Schiavo, C. 2022. Impact of hydro-alcoholic solvents on the oil and phenolics extraction from walnut (*Juglans regia* L.) press-cake and the self-emulsification of extracts. *Foods*, 11(2): 186.

Veza, I., Spraggon, M., Fattah, I. M. R., & Idris, M. 2023. Response surface methodology (RSM) for optimizing engine performance and emissions fueled with biofuel: Review of RSM for Sustainability Energy Transition. *Results in Engineering*, 18(1): 101213.

Yusoff, M. M., Gordon, M. H., & Niranjan, K. 2015. Aqueous enzyme assisted oil extraction from oilseeds and emulsion de-emulsifying methods: A review. *Trends in Food Science & Technology*, 41(1): 60-82.

Zúñiga-Diaz, J., Reyes-Dorantes, E., Quinto-Hernandez, A., Porcayo-Calderon, J., Gonzalez-Rodriguez, J. G., & Martinez-Gomez, L. 2017. Oil extraction from "morelos rice" bran: Kinetics and raw oil stability. *Journal of Chemistry*, 2017: 1-9.

BORNEO SCIENCE
THE JOURNAL OF SCIENCE & TECHNOLOGY

RESEARCH ARTICLE

Journal homepage: https://jurcon.ums.edu.my/ojums/index.php/borneo-science

TUNA HANDLINES IN SABAH: TECHNICAL ATTRIBUTES, OPERATIONAL DYNAMICS, AND GROSS PROFIT MARGINS

Mohd Samsul Rohizad Maidin*[1], Nadiayatul Atikah Harun[1], Mastura Mustapha[2], Abdul Wahab Abdullah[1] and Nor Azlin Mokhtar[3]

[*1] Fishing Gear Technology Division, Fisheries Research Institute (FRI) Kampung Acheh, 32000 Sitiawan, Perak, Malaysia.
[2] Marine Fishery Resources Development and Management Department, Southeast Asian Fisheries Development Center (MFRDMD/ SEAFDEC), Taman Perikanan Chendering, 21080 Kuala Terengganu, Terengganu, Malaysia.
[3] Tuna Development Section, Department of Fisheries Headquarters, 62628, Putrajaya, Malaysia.

*** Correspondence:**
samsulrohizad@dof.gov.my

Received: 01 February 2026
Revised: 15 April 2026
Accepted: 11 May 2026
Published online:
21 May 2026

Doi :
10.51200/bsj.v47i1.7350

Keywords:
Tuna handline; Artisanal; Fishing gear technology; Economic performance

ABSTRACT. *Tuna fisheries in Malaysia employ a variety of gears, with handlines representing the most widely licensed and practiced method, particularly in Sabah and Labuan. Despite their importance, detailed assessments of artisanal tuna handline fisheries remain limited. This study evaluates vessel specifications, gear attributes, operational dynamics, and economic performance of handline tuna fisheries across three localities: Kota Kinabalu, Semporna, and W.P. Labuan. Data were collected through structured interviews with 30 respondents, supplemented with field documentation of fishing gear. Results indicate that vessel capacity and engine horsepower vary considerably, with Kota Kinabalu operators employing larger, higher-horsepower vessels, enabling operations in distant fishing grounds compared to Semporna and Labuan. Handline structures were standardized across sites, comprising mainlines, swivels, sinkers, and C- or J-shaped hooks, with C-shaped hooks associated with higher catch rates and profitability. Fishing operations were closely linked to Fish Aggregating Devices (FADs), with trip frequencies ranging from three to four per month. Economic analysis revealed substantial variation, with gross profits per trip ranging from RM 2,171 in Semporna to RM 15,450 in Kota Kinabalu. Findings provide critical insights into the technical and economic dimensions of artisanal tuna handline fisheries, offering evidence to inform sustainable management and policy development.*

INTRODUCTION

In Malaysia, several types of fishing gear are used to catch tuna. The equipment and methods of operation vary depending on the fishing location, whether in shallow waters or the deep sea. Tuna is normally caught using gear such as longlines and handlines to target oceanic tuna species like Skipjack Tuna (*Katsuwonus pelamis*), Yellowfin Tuna (*Thunnus albacares*), Bigeye Tuna (*Thunnus obesus*), and Albacore (*Thunnus alalunga*). In addition to longlines and handlines, purse seines are also used to catch neritic tuna species such as Longtail Tuna (*Thunnus tonggol*), Kawakawa (*Euthynnus affinis*), Frigate Tuna (*Auxis thazard*), and Bullet Tuna (*Auxis rochei*). In the global fisheries sector, the use of longlines and handlines represents two types of fishing gear with distinct modes of operation. For example, in industrial fisheries, large vessels are used to catch tuna in deep-sea waters, equipped with advanced detection systems and mechanical navigation, requiring high capital investment. In addition, there are also small-scale and artisanal fisheries that operate with smaller boats and shorter operational periods compared to large-scale industrial fisheries. Handline fishing, on the other hand, is practiced by traditional fishermen in the South China Sea and Sulu Sea islands in Sabah.

According to the Malaysian Fisheries Statistics 2023, handlines represent the largest number of licensed fishing gear in Malaysia, totaling 6,525 units. The total landing of oceanic tuna amounted to 3,390 tonnes, with the majority 2,766 tonnes or 82% of the landings caught using handlines. Previous studies have shown that the use of handline gear by the Malaysian Fisheries Training Institute in 1988 successfully captured oceanic tuna in areas around Fish Aggregating Devices (FADs) near Layang-Layang Island in Sabah (Johari, 1989). There are studies carried out in different localities in the reporting on the uses of tuna handlines (Danial *et al.* 2023, Kurniawan *et al.* 2020, Hargiyatno *et al.* 2021, Nguyen *et al.* 2022 and Ajik & Tahiluddin, 2021). Despite the growing importance of artisanal tuna fisheries in Malaysia, particularly in Sabah, comprehensive data on gear specifications, fishing operations, and economic performance remain limited. This study addresses this knowledge gap by evaluating the technical attributes, operational dynamics, and gross profit margins of artisanal tuna fishermen in Sabah. The findings contribute to a deeper understanding of small-scale tuna fisheries and offer valuable insights to inform evidence-based fisheries management and policy formulation in the region.

MATERIALS AND METHODS

This study was conducted in Sabah (Kota Kinabalu and Semporna) and W.P Labuan which are located in the South China Sea Coast and the main economic activity in these three localities is fishery. The study was conducted from January to December 2024. A complete questionnaire form was prepared. To collect data on tuna handline, a total of 30 respondents were interviewed. The data collected included information on boat owners and crews, gear specifications, operational details and economic affairs. All the data were analysed using Microsoft Excel and the gear specifications used by the respondents were also documented. The estimated percentage of operating cost margins was calculated using this formula, Operating Cost (Ringgit Malaysia, RM)/ Catch Value (RM) x 100. The estimated Gross Profit per trip was calculated using this formula, Catch Value (RM) – Total Operating Cost (RM). Statistical analyses were performed using PAST (PAleontological STatistics software), an open-source platform for comparing group means and medians. In this study, a Kruskal-Wallis test was applied to assess differences among groups since the data that did not meet normality assumptions.

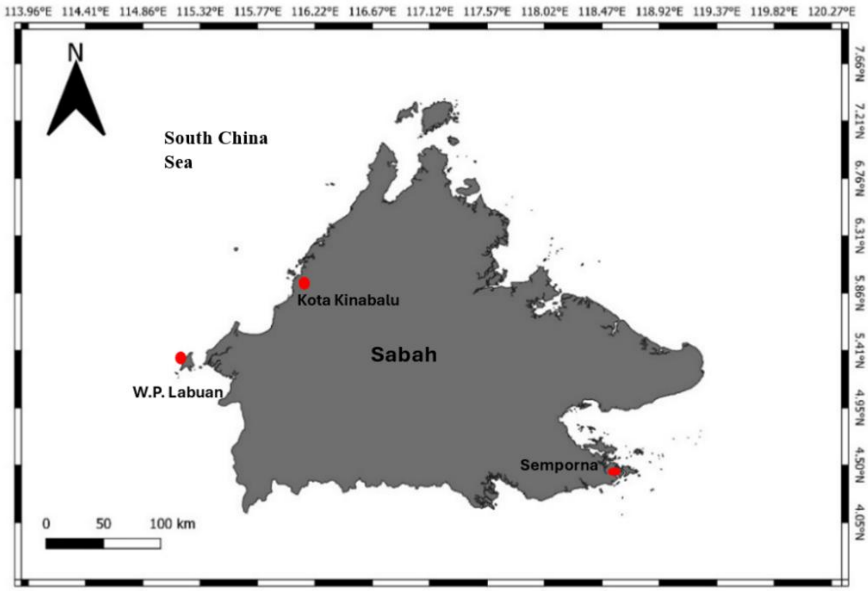

Figure 1. Study site involved three localities viz. Kota Kinabalu, W.P Labuan and Semporna (The map was generated using QGIS Desktop 3.34.1, an open-source geographic information system (https://download.qgis.org)

RESULTS AND DISCUSSION

General Specification of Vessels

The Gross Registered Tonnage (GRT) capacity of vessels in Semporna shows variation, ranging from 1.17 to 4.77. However, GRT data were not recorded for vessels in Kota Kinabalu and the W.P Labuan, limiting the comparative analysis of vessel capacity. In terms of engine horsepower (HP), vessels in Kota Kinabalu use more powerful engines, with 350 HP, compared to those in Semporna (40 HP and 15 HP) and Labuan (40 HP). Two out of four vessels in Semporna and also in Labuan use twin engines on a single vessel. The use of higher horsepower Cummins engines suggests that tuna handline vessels in Kota Kinabalu are capable of operating in more distant fishing grounds compared to the other two locations.

Tuna Handlines

In general, a handline consists of four main components: the mainline, swivels, sinkers, and hooks, as shown in Table 1. The fishing line commonly used is monofilament due to its strength and water resistance. To connect the lines and allow smooth rotation, standard barrel swivels are used in the tuna handline setup. In addition, sinkers such as lead and stone weights are used to bring the bait down to the desired depth. There are two types of hooks used by tuna handline fishermen: C-shaped hooks and J-shaped hooks. The main difference between these two hook types lies in the bait used. J-hooks are typically used with artificial lures such as coin-shaped metal jigs, plastic fish replicas, and polymer materials like feathers. On the other hand, C-shaped hooks are used with natural bait such as squid, squid ink, and fish meat slices to attract tuna. Fresh squid, caught using squid jigging gear, is commonly used as bait. According to Nghiep & Khanh (2025), the previous study revealed that C-shaped hooks yield 18% higher landing volume, attributed to the capture of larger-sized individuals. This size advantage translates into significantly greater economic returns for fishers, highlighting the potential of C-shaped hooks to enhance the profitability of handline tuna fisheries.

The adoption of C-shaped hooks has been shown to significantly enhance catch rates of target species such as Yellowfin Tuna (*T. albacares*) and Bigeye Tuna (*T. obesus)* compared with traditional J-shaped hooks, particularly in pelagic longline fisheries (Reinhardt *et al*., 2017; Kerstetter & Graves, 2006; Sales *et al*., 2010). Beyond improvements in capture efficiency, C-shaped hook design also confers important ecological benefits. Empirical studies demonstrate that C-shaped hooks substantially reduce the incidence of deep hooking, thereby lowering post-release mortality and mitigating bycatch of vulnerable non-target taxa, including sea turtles as well as sharks and rays (Sales *et al.*, 2010; Santos, 2023). Collectively, this body of evidence underscores the dual advantage of C-hook implementation: enhancing fishery yields while aligning with ecosystem-based management principles through bycatch reduction. These findings reinforce the role of C-shaped hooks as a practical, evidence-driven intervention to improve both the sustainability and economic viability of industrial pelagic longline fisheries. The technical attributes and configurations of tuna handlines in Semporna, W.P Labuan and Kota Kinabalu are illustrated in Figures 2–4. These schematics highlight the gear characteristics specific to each surveyed locality.

Table 1: General handline components and its functions

Components Image	Components and its function
	Handline/ *Koyan* – used for storing fishing lines.

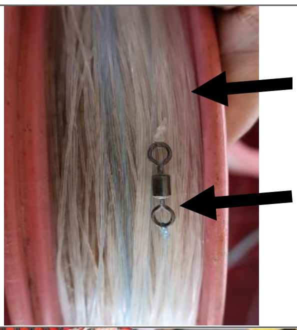	Mainline connects the sinker line to the hook. Swivel connects the fishing lines and allows smooth rotation of the handline.
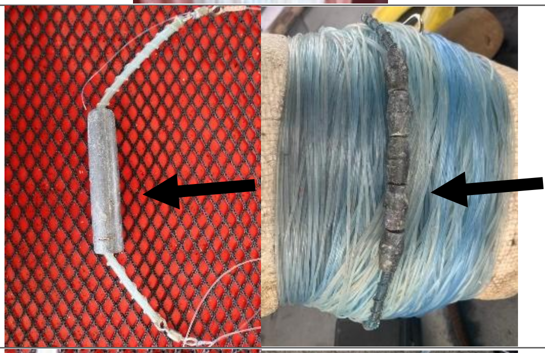	Lead/stone sinker - lowers the bait to the appropriate depth.
	Hook – attaches to the tuna's mouth when the bait is taken. Coin-shaped bait – used with J-shaped hooks; the shiny, reflective surface attracts the attention of tuna.
	Artificial fish bait – used with J-shaped hooks to attract tuna.
	Feather bait – used with J-shaped hooks to attract tuna.
	Squid ink bait – tied together with a sinker and dropped along with bait to simulate live squid in the water

Types of Gear: Tuna Handline

Location : Semporna

Target species : Yellowfin Tuna, Bigeye Tuna, Albacore Tuna and Skipjack Tuna

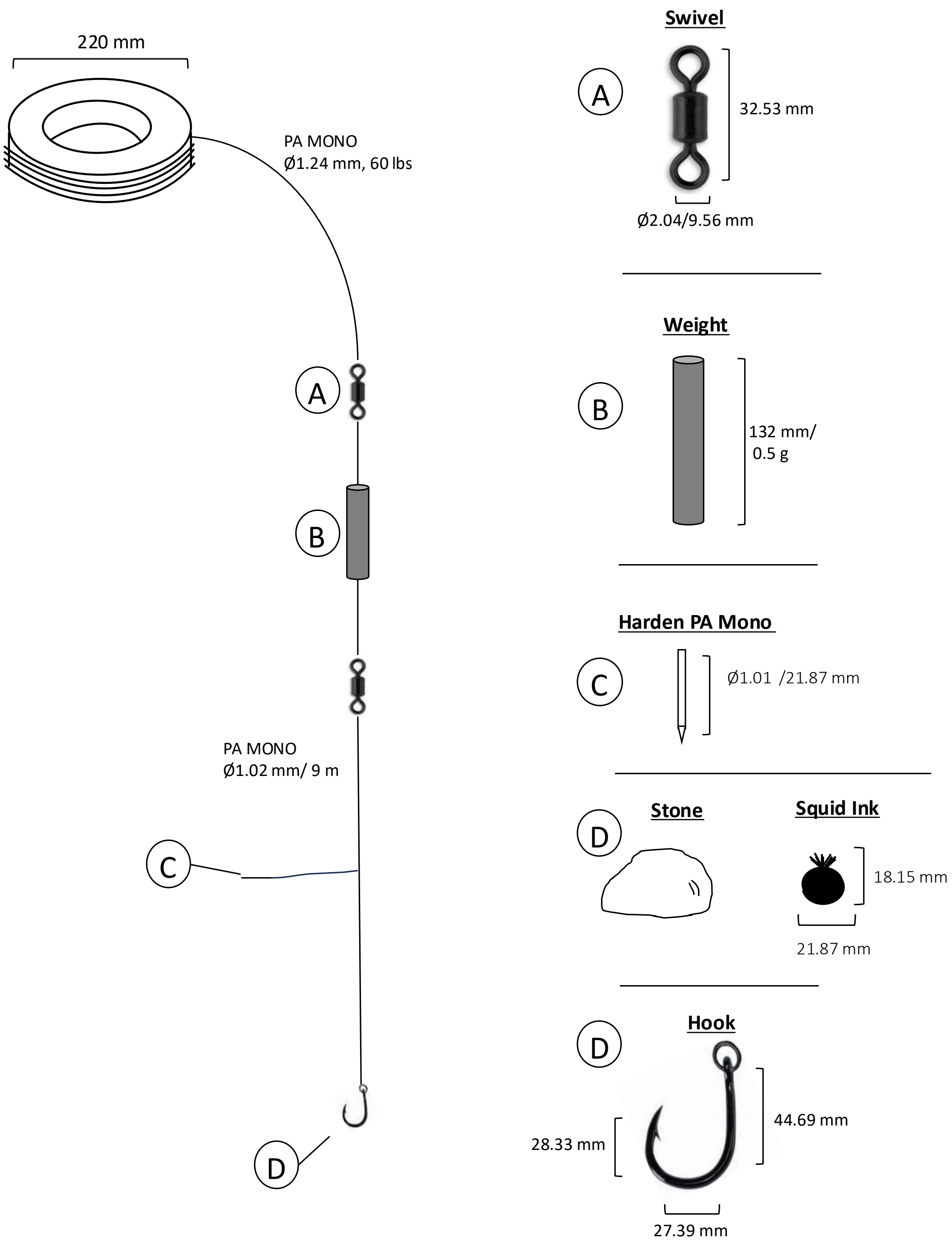

Figure 2a.: Technical attributes of tuna handline in Semporna

Types of Gear: Tuna Handline

Location : Semporna

Target species : Yellowfin Tuna, Bigeye Tuna, Albacore Tuna and Skipjack Tuna

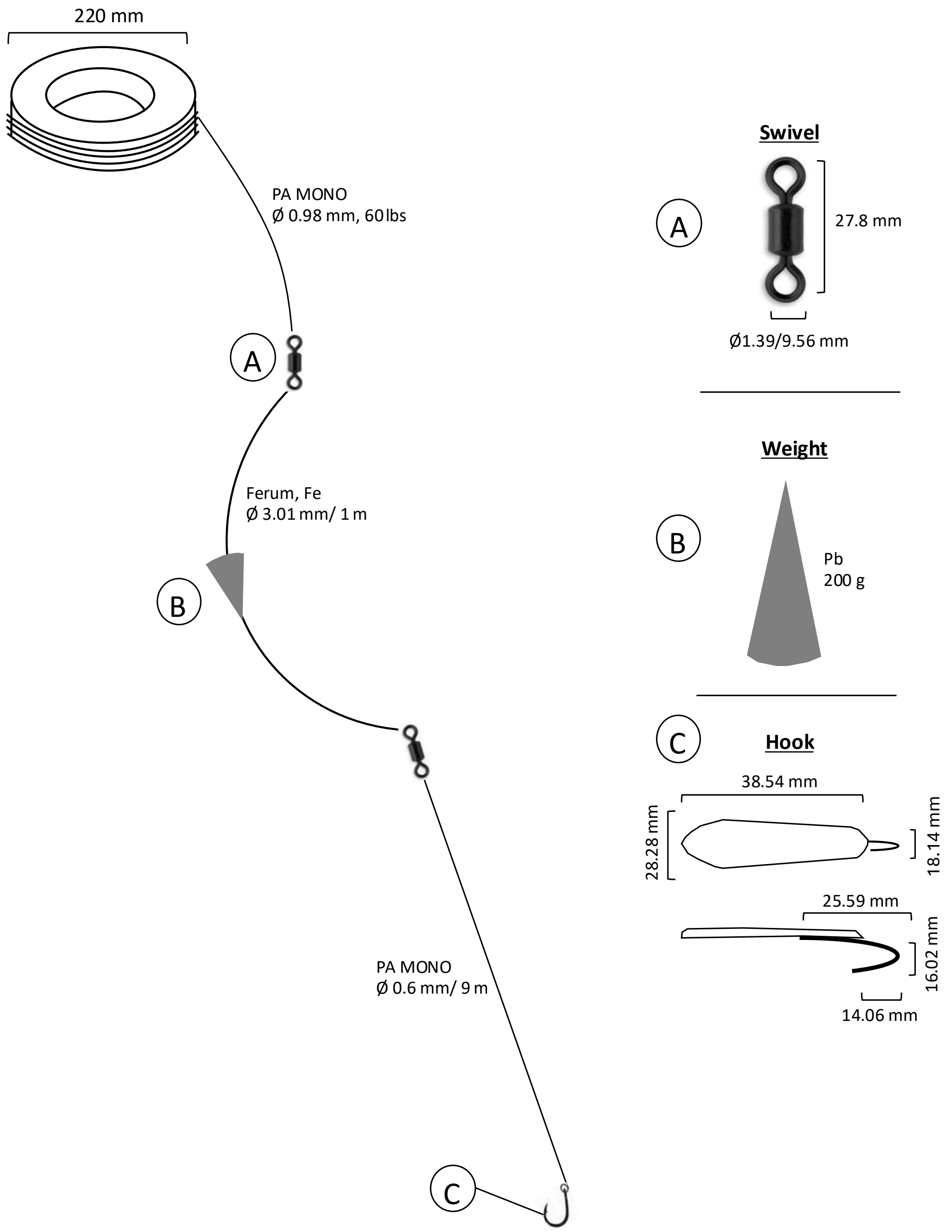

Figure 2b.: Technical attributes of tuna handline in Semporna

Types of Gear: Tuna Handline

Location : Semporna

Target species : Yellowfin Tuna, Bigeye Tuna, Albacore Tuna and Skipjack Tuna

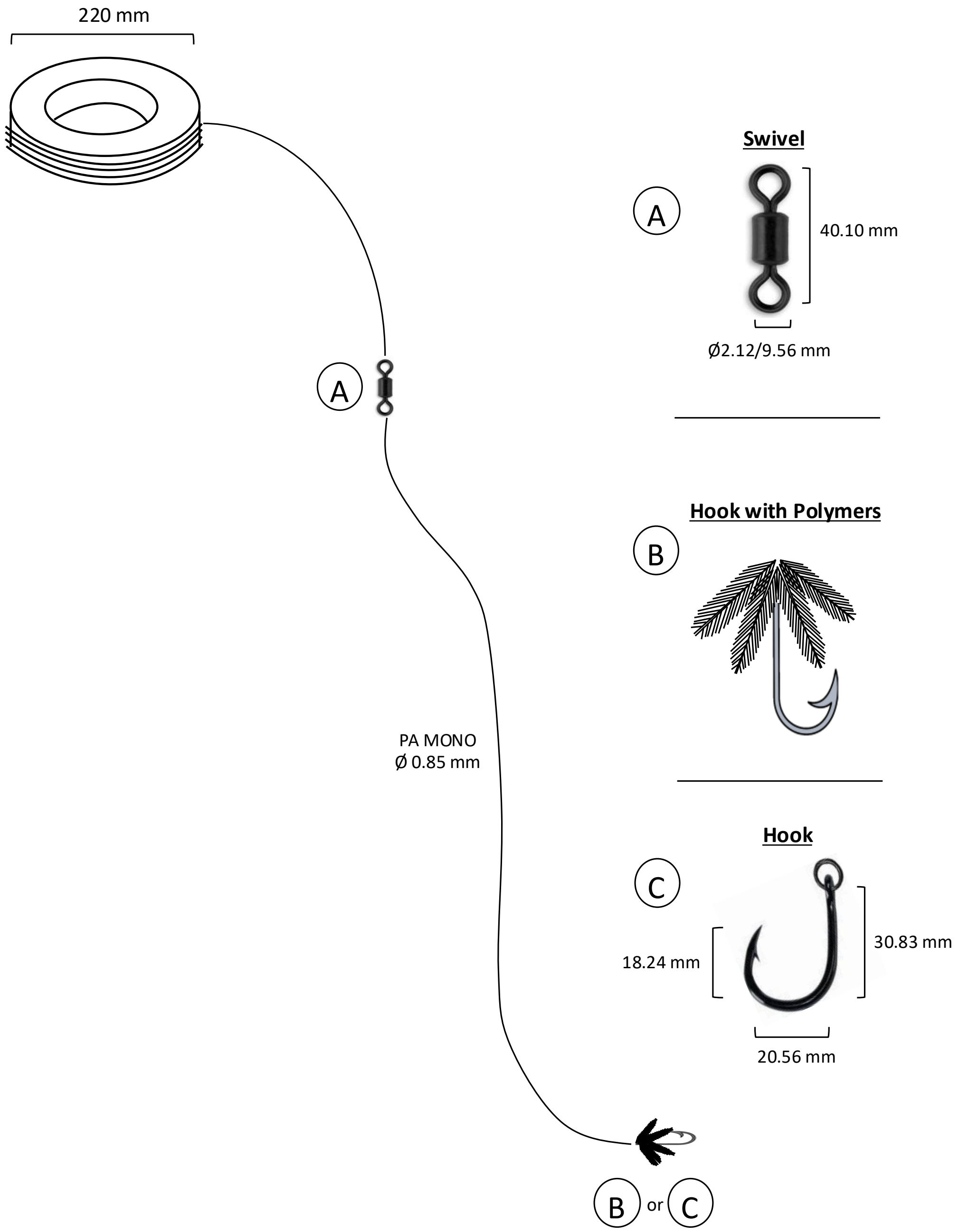

Figure 2c.: Technical attributes of tuna handline in Semporna

Types of Gear: Tuna Handline

Location : Labuan

Target species : Yellowfin Tuna, Bigeye Tuna, Albacore Tuna and Skipjack Tuna

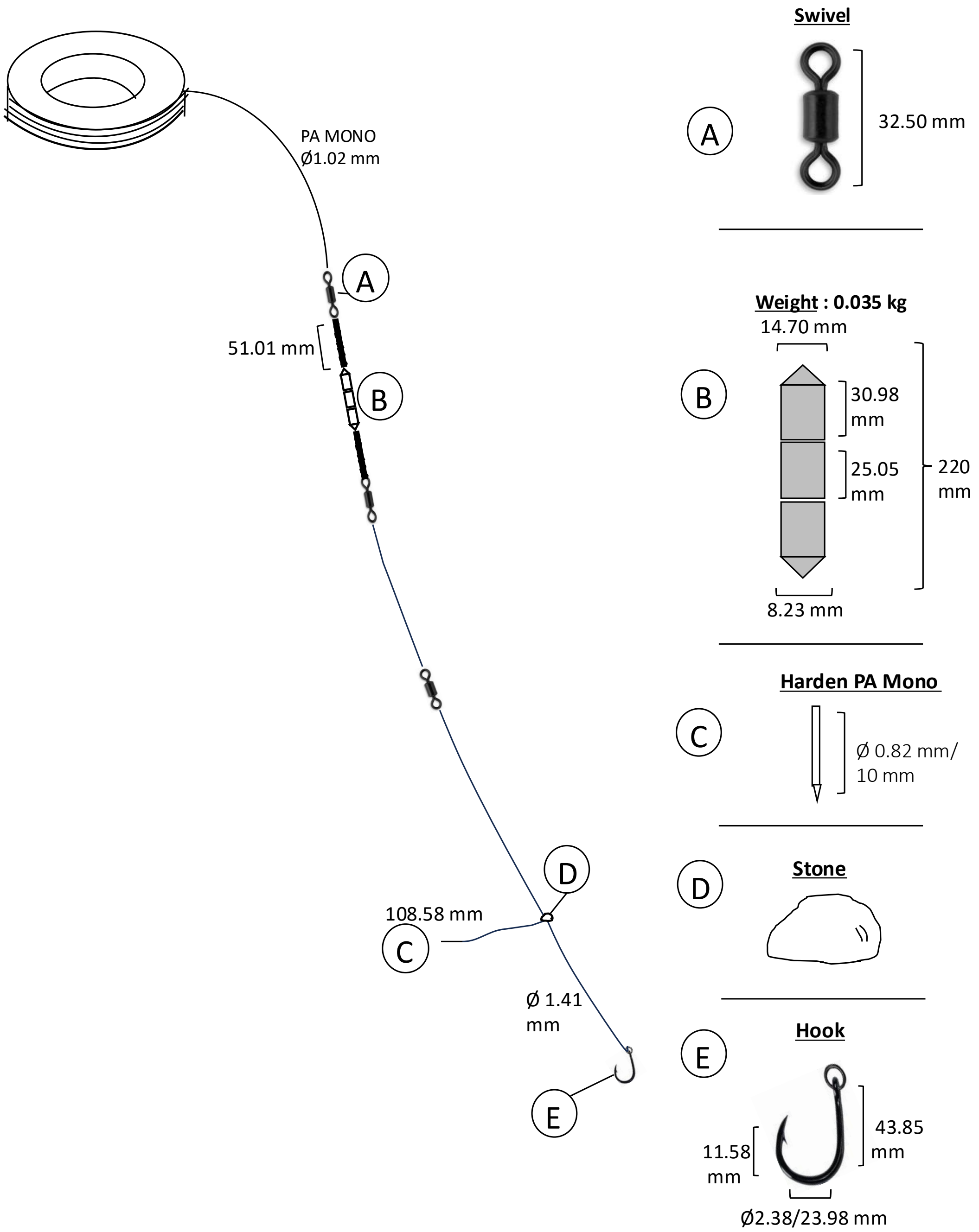

Figure 3a.: Technical attributes of tuna handline in Labuan

Types of Gear: Tuna Handline

Location : Labuan

Target species : Smaller size Yellowfin Tuna, Bigeye Tuna, Albacore Tuna and Skipjack Tuna

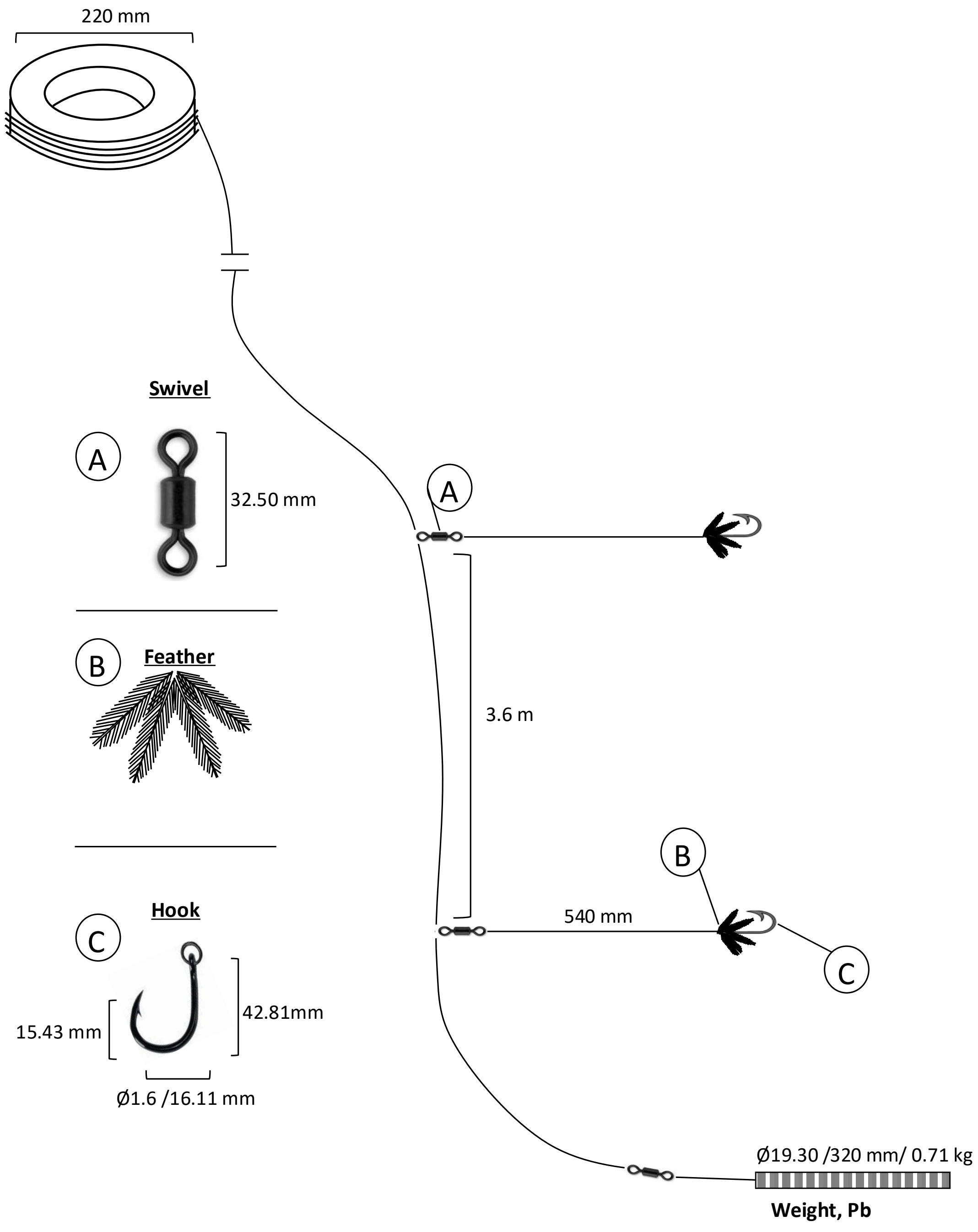

Figure 3b.: Technical attributes of tuna handline in Labuan

Types of Gear: Tuna Handline

Location : Labuan

Target species : Yellowfin Tuna, Bigeye Tuna, Albacore Tuna and Skipjack Tuna

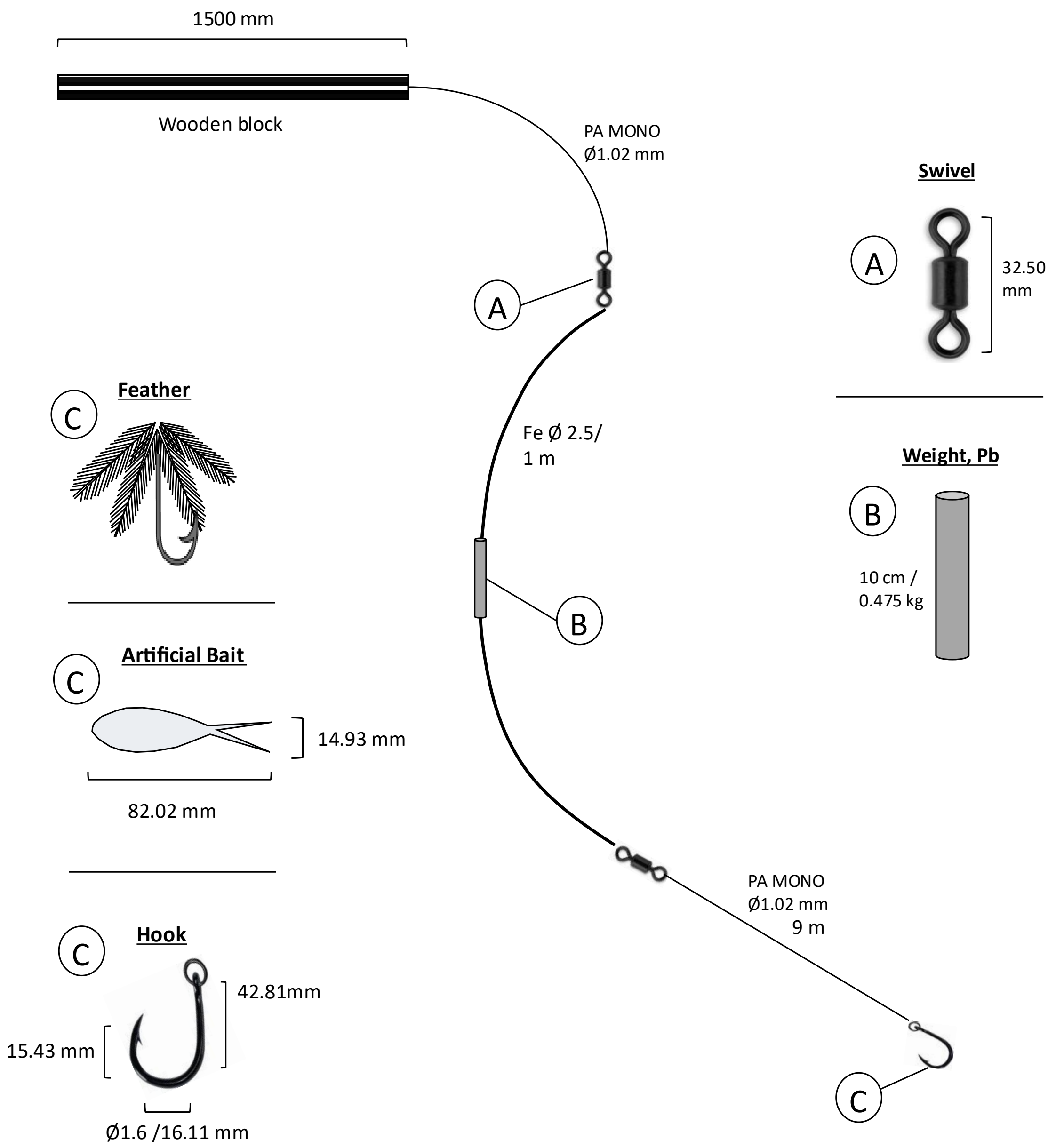

Figure 3c.: Technical attributes of tuna handline in Labuan

Types of Gear: Tuna Handline

Location : Labuan

Target species : Yellowfin Tuna, Bigeye Tuna, Albacore Tuna and Skipjack Tuna

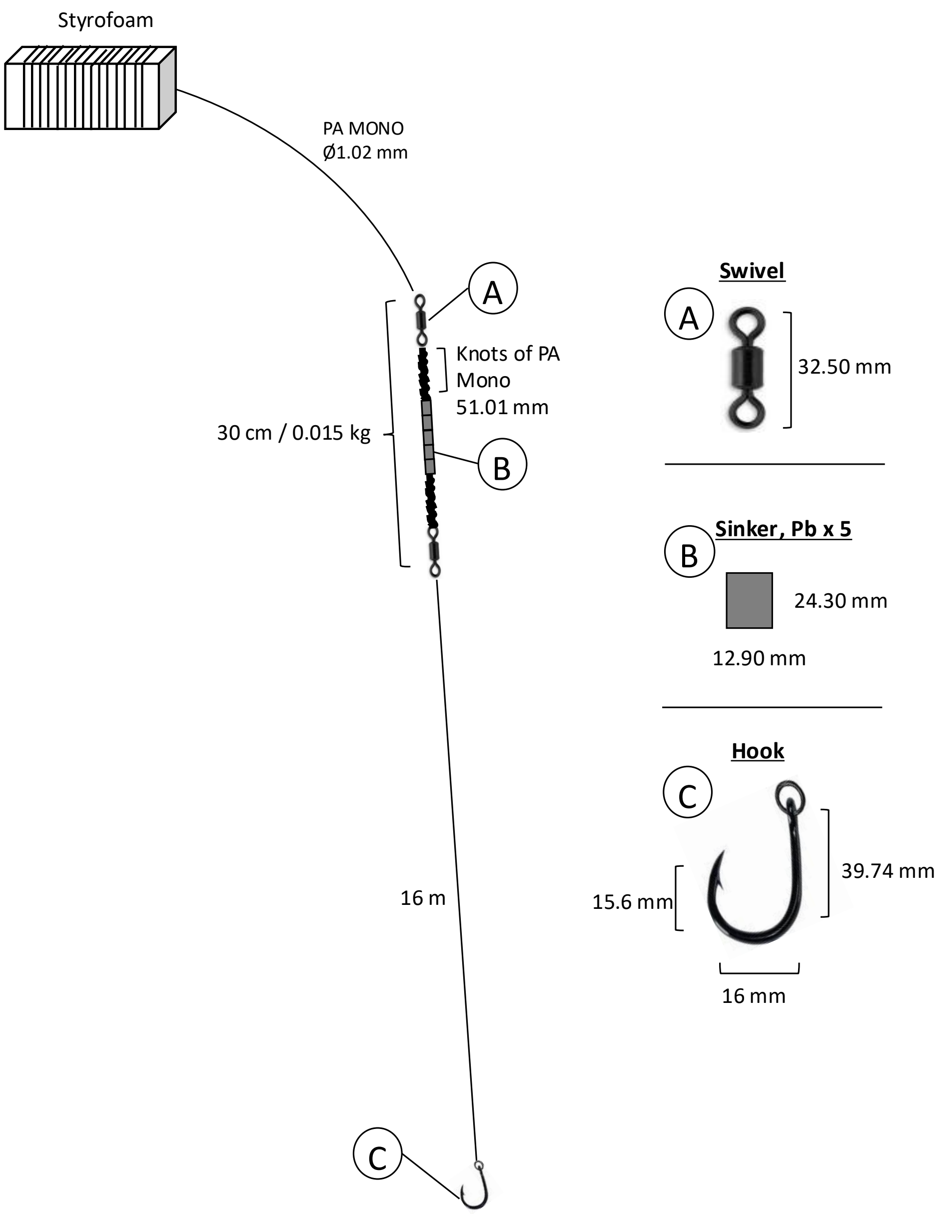

Figure 3d.: Technical attributes of tuna handline in Labuan

Types of Gear: Tuna Handline

Location : Kota Kinabalu

Target species : Yellowfin Tuna, Bigeye Tuna, Albacore Tuna and Skipjack Tuna

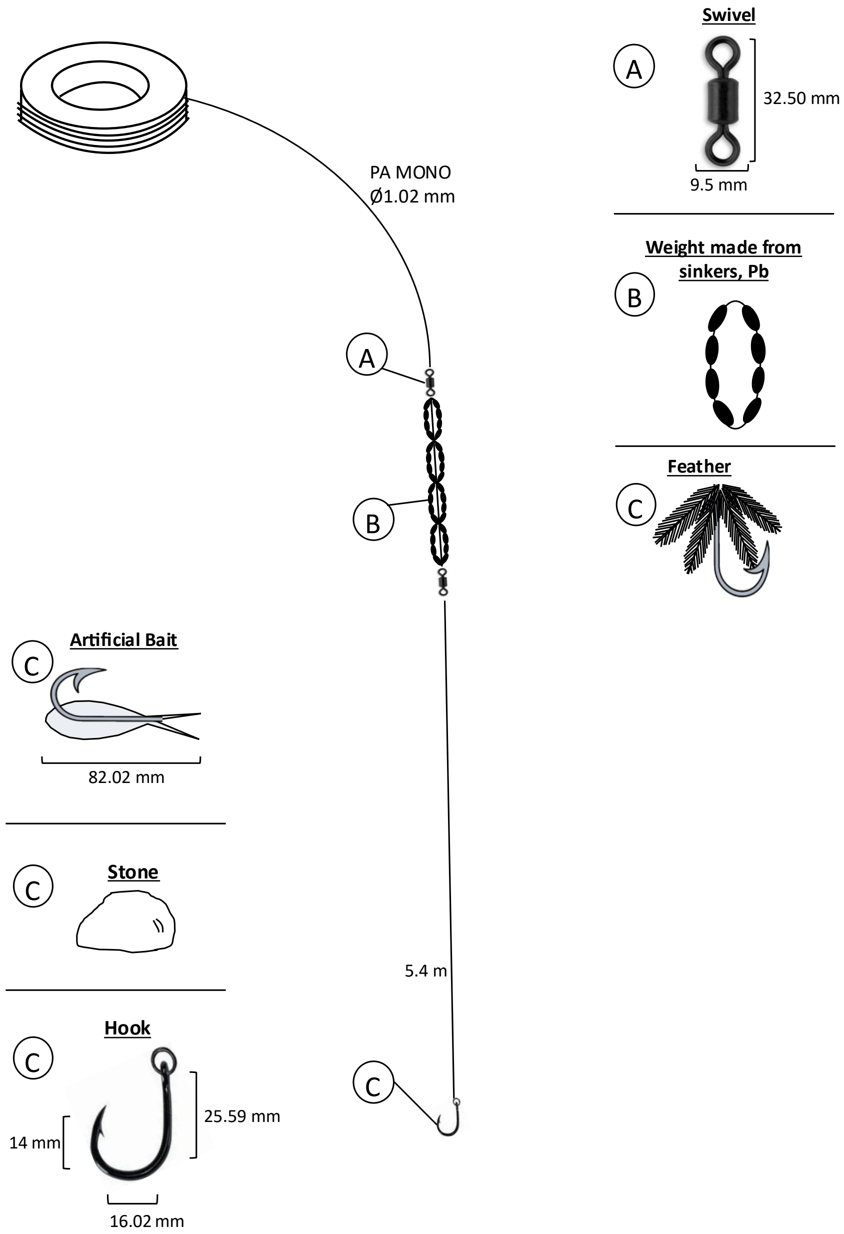

Figure 4a.: Technical attributes of tuna handline in Kota Kinabalu

Types of Gear: Tuna Handline

Location : Kota Kinabalu

Target species : Yellowfin Tuna, Bigeye Tuna, Albacore Tuna and Skipjack Tuna

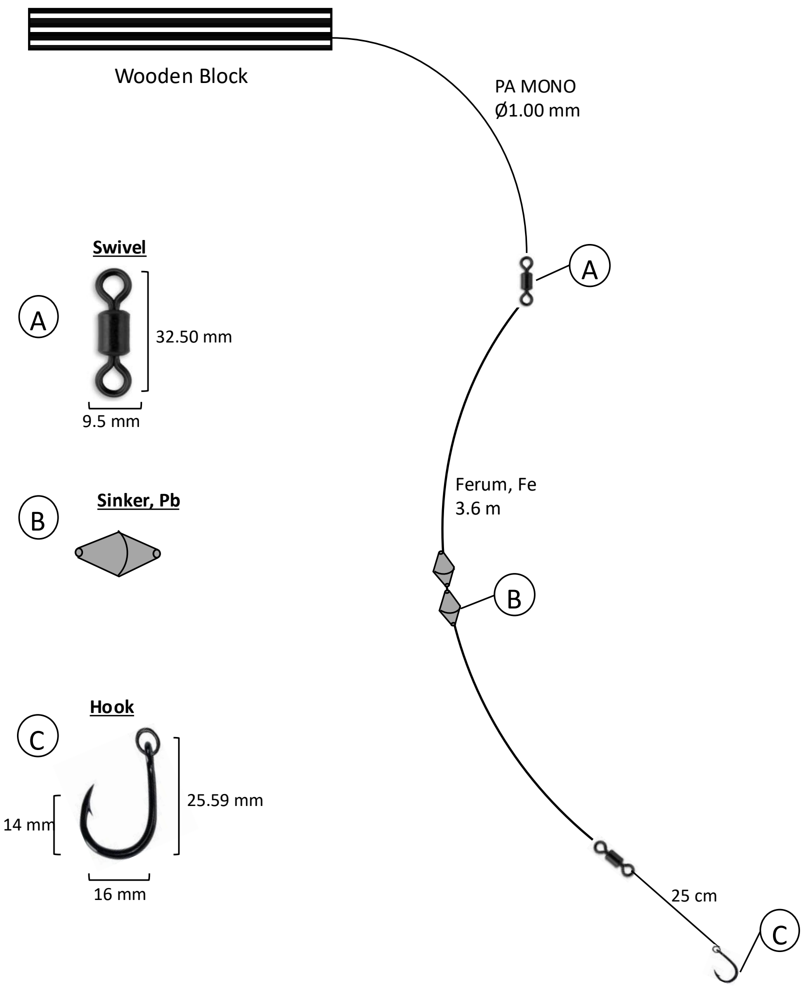

Figure 4b.: Technical attributes of tuna handline in Kota Kinabalu

Types of Gear: Tuna Handline

Location : Kota Kinabalu

Target species : Yellowfin Tuna, Bigeye Tuna, Albacore Tuna and Skipjack Tuna

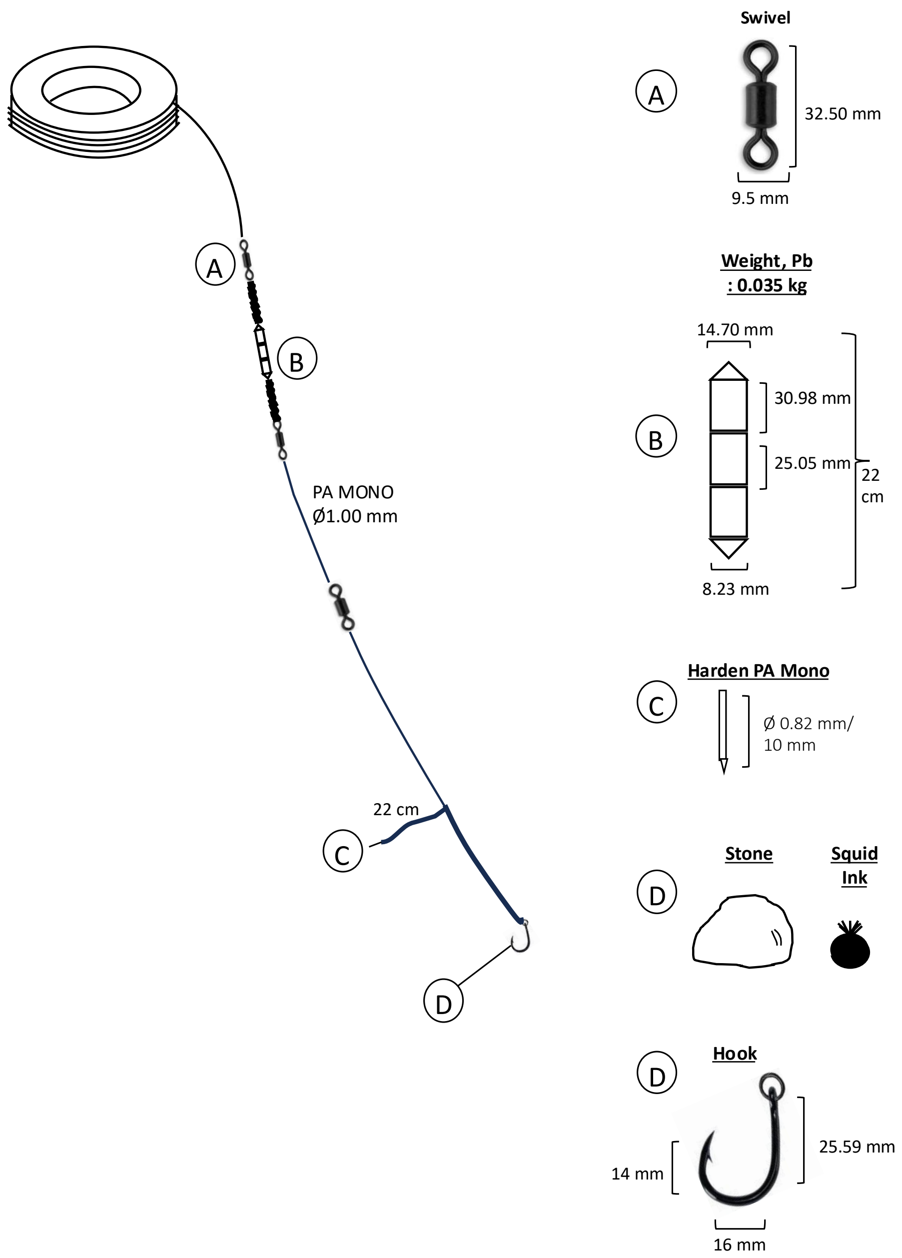

Figure 4c.: Technical attributes of tuna handline in Kota Kinabalu

Handlines Operation

Table 2 presents a comparison of tuna handline fishing operations by tuna fishermen in three key locations in Sabah and the Federal Territory of Labuan. The main fishing areas in Semporna are concentrated around FADs, or *payao* located approximately 12 nautical miles from Mabul Island and 3 nautical miles from Sipadan Island. In contrast, fishing operations in Kota Kinabalu take place between 120 and 140 nautical miles offshore, while operations in Labuan are conducted 90 nautical miles from the port. In most cases, all tuna fishing areas are located around artificial FADs installed by the fishermen themselves. In Kota Kinabalu, one fisherman reportedly owns around 40 FAD units, with a total fabrication cost of RM12,000 per FAD.

Local FADs in Southeast Asia are generally regulated through a combination of national fisheries legislation and regional fisheries management organization measures such as limits on FAD deployment, spatial–temporal closures, and the adoption of biodegradable or non-entangling designs yet their ownership often remains informal, whether private or communal, and is poorly documented. This lack of clear ownership contributes to accountability gaps, while increasing FAD density has been linked to ecological impacts including higher juvenile tuna mortality, increased bycatch of non-target species, alterations in fish behaviour and migration patterns, and the accumulation of marine debris (Dagorn *et al*., 2013). Further empirical validation is needed to confirm these hypotheses and prevent the overstatement of results.

Table 2: Comparison of tuna handline fishing operations at three locations in Sabah and W.P. Labuan

Operation/ Location	Semporna	Kota Kinabalu	W.P Labuan
Fishing Area (nautical mile, NM)	12 NM from Mabul Island; 3 NM from Sipadan Island	120–140 NM from Kota Kinabalu	90 NM from port
Presence of FADs	✓	✓	✓
Number of FADs	NA	40 units	NA
Cost per FAD	NA	RM12,000	NA
Hook depth from Surface	40-50 m	30-40 m	55 m
Operation Time	Daytime (6 AM–6 PM)	Day/Night	Daytime
Time taken to land Tuna (>50kg)	1-2 hours	0.5-1 hour	0.5-1 hour
Water Depth	1500 m – 2000 m	1000 m	NA
Bait Types	✓ Fish & squid ✓ Artificial fish ✓ Squid ink	✓ Fish & squid ✓ Artificial fish ✓ Squid ink	✓ Fish & squid ✓ Artificial fish ✓ Squid ink
Trips per Month	3	3	4
Fishing Operations per Day	1	1-2	1
Water Conditions During Operation	NA	NA	NA
Main Target Species	Yellowfin Tuna Bigeye Tuna Albacore	Yellowfin Tuna Bigeye Tuna Albacore	Yellowfin Tuna Bigeye Tuna Albacore
Bycatch Species	Mahi-mahi Spanish Mackerel	Mahi-mahi Spanish Mackerel Black Marlin	Spanish Mackerel

Tuna fishing operations in Sabah are typically carried out regularly, with about three trips per month, while in Labuan, fishermen make up to four trips per month. Each trip usually lasts four to five days to maximize catch yield. In Semporna and Labuan, fishing is conducted once per day, whereas in Kota Kinabalu, it ranges from once to twice daily. Fishing activities begin after dawn, and end in the evening in Semporna and Labuan. In Kota Kinabalu, however, operations may take place during the day or night. The time taken to land a tuna fish per session varies from 30 minutes to two hours, particularly for tuna weighing over 50 kg. The fishing method involves lowering baited handlines to water depths ranging from 1,000 to 2,000 meters, with hook depths from the surface recorded as 40–50 meters (Semporna), 30–40 meters (Kota Kinabalu), and 55 meters (Labuan).

Common bait types used by tuna handline fishermen in Sabah include fish meat cuts, squid, artificial fish, and squid ink. The fishing techniques and tuna fishing gear specifications employed by artisanal fishers in Malaysia exhibit notable similarities to those practiced in the Philippines. Mendoza *et al.* (2023) reported that traditional Filipino fishers capture tuna by attaching a lump of squid ink to a stone, which is then deployed alongside a hook. Upon release, the ink disperses, creating both a visual and olfactory stimulus that attracts tuna. Squid ink has been shown to contain amino acids that act as feeding stimulants for certain fish species (Derby *et al*., 2013).

Additionally, the use of reflective coins as artificial lures by local fishers has demonstrated effectiveness in attracting tuna. Tunas are highly sensitive to light (Fritsches, 2002) and are drawn to the reflective properties of artificial lures that mimic the coloration of predatory fish. This was corroborated by Tauladani *et al*. (2013), who found that catch rates with artificial lures exceeded those obtained with natural baits such as fish flesh. In Semporna, a subset of tuna handline fishers has adopted the use of lead sinkers integrated with stainless steel wire, known as the Shutter. This innovation, also developed by Sururi *et al*. (2021) and trialed among fishers near Raam Island, Indonesia, proved both effective and environmentally preferable to traditional stone weights, which can damage marine habitats. Pointed design of the lead component reduces hydrodynamic drag during deployment. Subsequent evaluations by Sururi *et al*. (2022) demonstrated that the shutter substantially improves tuna catch efficiency compared to conventional methods.

Although sea conditions do not directly affect fishing operations, environmental factors such as weather particularly rain and storms have a significant impact on operational smoothness and fisher safety. The primary target species for tuna handlining in the waters off Sabah and Labuan include Yellowfin Tuna, Bigeye Tuna, and Albacore Tuna. Bycatch species include Mahi-mahi, Marlin, and Spanish Mackerel.

Handlines Economic Analysis

Table 3 shows the calculation of gross profit per trip for tuna handline fishermen in Sabah and the W.P Labuan. The landed catch from each fishing trip varies by location. On average, the quantity of tuna landed is around 905kg, 5,500kg and 900kg per trip for Semporna, Kota Kinabalu and W.P. Labuan, respectively. The value of landed catch across the three locations ranges from RM7,240 (Semporna), RM44,000 (Kota Kinabalu) and RM7,200 (W.P. Labuan) with the average price per kg is RM8 (Personal communication, 2024).

Table 3: Average gross profit calculation per trip for tuna handline fishermen in Sabah and W.P Labuan

Item / Location	Semporna	Kota Kinabalu	W.P. Labuan
Sample size	n=20	n=4	n=6
Catch weight (Kg)	905	5,500	900
Catch value (RM)	7,240	44,000	7,200
Total operating cost (RM)	5,864	28,550	5,029
Petrol/ Diesel	1450	4500	1498
Food	-	1500	300
Wages/ Salary	4264	21,000	2,971
Ice	150	1200	260
Bait/ Others	-	350	-
Operating cost margin	81%	65%	70%
Gross profit per trip (RM)	1,376	15,450	2,171

The Kruskal-Wallis test revealed significant differences in catch weight and catch value between all locations involved ($p = 0.00193$, $p < 0.05$). Further Dunn's post hoc test revealed that there were significant differences in catch weight and catch value between Semporna-Kota Kinabalu and Kota Kinabalu-W.P Labuan. However, there was no significant difference between Semporna-Labuan. The wide range of catch values reflects the inherent unpredictability of the tuna industry, which is highly dependent on seasonal fluctuations and biological factors. Despite the growth potential of Malaysia's tuna industry, these findings highlight a critical need for improved post-harvest handling and more equitable profit distribution to ensure the socio-economic sustainability of small-scale fishers in East Malaysia (Department of Fisheries Malaysia, 2019).

The estimated operating costs range from RM5,864 (Semporna), RM28,550 (Kota Kinabalu) and RM5,029 (W.P. Labuan) with operating cost margins 81%, 65% and 70% respectively. The high proportion of variable costs (fuel, bait, and labour) relative to gross revenue results in narrow profit margins, substantially increasing the financial vulnerability of fishers in Semporna, Kota Kinabalu and W.P Labuan. This aligns with global trends where fuel and labour typically constitute the largest share of variable fishing costs (Lam *et al*., 2011). The lowest gross profit per trip recorded for fishermen in Semporna is approximately RM1,376, while fishermen in Kota Kinabalu earned the highest profit at RM15,450 per trip. Meanwhile, the gross profit for fishermen in W.P. Labuan is close to that of Semporna, with RM2,171. These variations are often attributed to the logistical advantages of larger hubs like Kota Kinabalu, where established supply chains allow for more competitive pricing and lower relative overheads compared to rural districts (Albat *et al*., 2014).

CONCLUSION

This study underscores the significant diversity in tuna handline fisheries across Sabah and W.P. Labuan, where variations in vessel capacity and gear technology directly influence both operational reach and economic viability. The findings highlight that Kota Kinabalu serves as a primary hub for industrial-scale handline operations, utilizing higher horsepower engines (350 HP) to access distant fishing grounds, which translates to substantially higher catch volumes (5,500kg) and gross profits (RM 15,450) compared to the more localized artisanal operations in Semporna and Labuan. Technically, the integration of C-shaped hooks and innovative lures like squid ink and reflective coins demonstrates a strategic alignment with both capture efficiency and ecological sustainability. However, the high operating cost margins (65%–81%) driven largely by fuel and labour reveal a precarious economic landscape for smaller-scale fishers who remain vulnerable to seasonal fluctuations and market middlemen. To ensure the long-term socio-economic sustainability of Malaysia's tuna industry, it is imperative to address these disparities through improved logistical support, standardized data recording for vessel capacities, and the implementation of more equitable marketing frameworks that protect the livelihoods of fishers in rural landing sites.

ACKNOWLEDGEMENT

The authors gratefully acknowledge the Capture Fishery Resources Division, Department of Fisheries Headquarters, Putrajaya, for providing financial support for this research. We also extend our sincere appreciation to the Department of Fisheries Sabah, particularly Dr. Helena Biun, Binjimin Benjamin Martin, and Justin Agon, as well as the fisheries staffs in W.P Labuan and Semporna for their valuable assistance and cooperation. Our thanks are further extended to Muhammad Shakirin S, Wan Muhammad Luqman WR, Raja Hanif Asyraf RO, Allahyarham Nazir T and Syamrizan A and all respondents who participated in and contributed to this study.

REFERENCES

Ajik, J. O., & Tahiluddin, A. B. (2021). Size distribution, length-weight relationship, and catch per unit effort of frigate tuna, Auxisthazard (Lacepède, 1800) in Tawi-Tawi waters, southern Philippines, caught using multiple handline. *Marine Science and Technology Bulletin*, 10(4), 370-375. https://doi.org/10.33714/masteb.974182

Albat, M., Komilus, C. F., & Alin, J. M. (2014). *Determinants of trust and business performance: the case of tuna fishery industry in Semporna, Sabah*. CABI Digital Library. https://www.cabidigitallibrary.org/doi/pdf/10.5555/20193284474

Danial, A. Riza Baroqi, Wildan, Putra Satria Timur, and Syahrul. 2023. "Composition of Tuna Catch Hand Line at the Fish Landing Base (FLB) Lonrae, Bone Regency, South Sulawesi Province, Indonesia". *Asian Journal of Fisheries and Aquatic Research* 25 (5):20-27. https://doi.org/10.9734/ajfar/2023/v25i5696

Department of Fisheries Malaysia. (2019). *National Report to the Scientific Committee of the Indian Ocean Tuna Commission*. https://iotc.org/sites/default/files/documents/2019/11/IOTC-2019-SC22-NR15.

Derby, C.D., Tottempudi, M., Love-chezem, T., & Wolfe, L.S. (2013). Ink From Longfin Inshore Squid, Doryteuthis pealeii, as a Chemical and Visual Defense Against Two Predatory Fishes, Summer Flounder, Paralichthys dentatus, and Sea Catfish, Ariopsis felis. *Biological Bulletin* ,225: 152–160.

Fritsches, K. (2002) *Vision in billfish project*. Research Progress Report. University of Queensland.

R. Kurniawan, B. Setyadji, S. C. Nugroho, and T. A. Wibawa, "Spatio-Temporal Variations of Yellowfin Tuna Caught by Handline in the Indian Ocean, South Of Nusa Tenggara," *Saintek Perikanan: Indonesian Journal of Fisheries Science and Technology*, vol. 16, no. 3, pp. 187-191, Oct. 2020. https://doi.org/10.14710/ijfst.16.3.187-191

Reinhardt, J. F., Weaver, J., Latham, P. J., Dell'Apa, A., Serafy, J. E., Browder, J. A. & Blankinship, D. R. (2017). Catch rate and at-vesel mortality of circle hooks versus j-hooks in pelagic longline fisheries: a global meta-analysis. *Fish and Fisheries*, 19(3), 413-430.

Hargiyatno, I. T., Anggawangsa, R. F., Natsir, Moh., Sedana, I. G. B., Widodo, A. A., & Wudianto. (2021). DOI: 10.5281/zenodo.100906271938.V18.I10. Comparison of handline tuna catches in Indian Ocean and Banda Sea waters. *E3S Web of Conferences*, 322,03004. https://doi.org/10.1051/e3sconf/202132203004

Kerstetter, D. W. dan Graves, J. E. (2006). Effects of circle versus j-style hooks on target and non-target species in a pelagic longline fishery. *Fisheries Research*, 80(2-3), 239-250.

Lam, V. W. Y., Sumaila, U. R., Dyck, A., Pauly, D., & Watson, R. (2011). Construction and first applications of a global cost of fishing database. *ICES Journal of Marine Science*, 68(9), 1996–2004. https://doi.org/10.1093/icesjms/fsr121

Nguyen, K.Q.; Phan, H.T.; Tran, P.D.; Van Nguyen, B.; Van Do, T.; Nguyen, L.T.; Van To, P.; Vu, N.K. (2022). Length-Length, Length–Weight, and Weight-Weight Relationships of Yellowfin (Thunnus albacares) and Bigeye (Thunnus obesus) Tuna Collected from theCommercial Handlines Fisheries in the South China Sea. *Thalassas*, 38, 911–917.

Mendoza, D.M., Aquino, M.G.B., Briñas, K.B. & Mendoza G.C. (2023). The Tuna Handline fishing fleet of Infanta, Pangasinan, Philippines: An assessment. *International Journal of Fisheries and Aquatic Studies*,11(1): 49-56.

Sales, G., Giffoni, B., Fiedler, F. N., Azevedo, V. G. d., Kotas, J. E., Swimmer, Y. & Bugoni, L (2010). Circle hook effectiveness for the mitigation of sea turtle bycatch and capture of target species in a brazilian pelagic longline fishery. *Aquatic Conservation: Marine and Freshwater Ecosystems*, 20(4), 428-436.

Santos, C. (2023). A review of reported effects of pelagic longline fishing gear configurations on target, bycatch and vulnerable species. *Aquatic Conservation Marine and Freshwater Ecosystems*, 34(1).

Sururi, M., Sudirman, S., Ulat, M. A., Razak, A. D., Kasim, M., & Poltak, H. (2021). Shutter operation and iradium squid fishing on handline tuna fishing for sustainability. *Buletin SWIMP*, 1(2)072 – 076.

Sururi, M., Kasim, M., Mustasim, M., Ulat, M. A., Muhfizar, M., & Maskur, M. (2022). Shuter, the innovation tools to replace stone for handline bait of tuna. AQUASAINS: *Jurnal Ilmu Perikanan dan Sumberdaya Perairan*, 11(1), 1210–1218.

Tauladani, S., Arifin, M., & Wijaya, N. (2013). The effect of artificial and natural baits on the capture of tuna hand line around the molucca sea. *Aquatic Science & Management*, 57-61.

RESEARCH ARTICLE

BORNEO SCIENCE
THE JOURNAL OF SCIENCE & TECHNOLOGY

Journal homepage: https://jurcon.ums.edu.my/ojums/index.php/borneo-science

SEDIMENTOLOGY OF BONGAYA FORMATION, JAMBONGAN ISLAND, BELURAN, SABAH, MALAYSIA

Khor Wei Chung[1*], Isaac Abraham Jeslis[1], Junaidi Asis[1], Baba Musta[1] and Mohd Al Farid Abraham[1]

[1]Geology Program, Faculty of Science and Technology, Universiti Malaysia Sabah, Malaysia.

*** Correspondence:**
khorweichung@ums.edu.my

Received: 16 April 2026
Revised: 23 May 2026
Accepted: 24 May 2026
Published online:
25 May 2026

Doi :
10.51200/bsj.v47i1.7578

Keywords:
Bongaya Formation; Sedimentology; Facies Analysis; Geology Sabah.

ABSTRACT.
Jambongan Island is located at Northeast Borneo, Sabah. The exposed Bongaya Formation on this island is a Neogene siliciclastic succession characterized by sandstones, shales, and occasional conglomerates. The formation is Miocene aged with highly friable nature of the sandstones suggests an age potentially extending into the Early Pliocene. This study utilizes detailed sedimentary logging of 11 outcrops to refine the depositional framework of the formation. Six distinct facies were identified: Hummocky Cross-Stratified (HCS), Swaley Cross-Stratified (SCS), Horizontally Stratified (Sh), Flaser Bedded Sandstone (FF), Structureless Sandstone (Sm), and Mudstone (M). Three facies associations are identified to represent a progradational, high-energy shoreface model ranging from lower shoreface to foreshore environments. Notably, the absence of the distal shelf-to-transition zone suggests that fair-weather finer grained deposits were either bypassed or eroded by intense storm currents during rapid progradation.

INTRODUCTION

The Neogene sedimentary rocks of Sabah, North Borneo, are primarily deposited within unique “circular” to sub-circular basins. These features as the Sandakan and Maliau basins are often interpreted as pull-apart or extensional basins (Tongkul, 1991). High volumes of sediment filled these depressions throughout Neogene period, resulting in thick, wave-dominated shoreface and deltaic system (Tongkul, 1991). The Bongaya Formation, prominently exposed in the Northeast Sabah Basin and across Jambongan Island, in the Beluran district (Figure 1). It is assigned Middle to Late Miocene in age with highly friable nature of the sandstones suggests that these units may be as young as the Early Pliocene (Sanudin Tahir and Baba Musta, 2007).

Other Neogene units in Sabah are Tanjong, Sandakan, Kapilit, South Banggi formations. These formations are of great interest to the industry as they are considered potential onshore analogues to the oil and gas reservoirs found in the offshore Sabah basins. Detailed sedimentological studies are vital for establishing accurate onshore-to-offshore correlations. By analyzing the well-exposed outcrops across Jambongan Island, reservoir potential, sand-body geometry, and internal facies architecture can be estimated be compared to the formation located at the offshore subsurface.

This research focuses on investigating the general geology and depositional settings of Jambongan Island by integrating new, high-resolution sedimentological data. The primary objective of this study is to characterize the localized facies architecture and establish a comprehensive depositional model for the area, thereby resolving existing ambiguities regarding its paleoenvironmental evolution. By refining the stratigraphic framework of the Bongaya Formation, this study provides critical insights into the spatial distribution and quality of high-energy shoreface reservoirs. These findings also offer a valuable analogue for understanding similar progradational, high-energy wave-dominated systems globally. This enables predictive utility for hydrocarbon exploration, carbon capture storage (CCS) site characterization, and hydrogeological modeling.

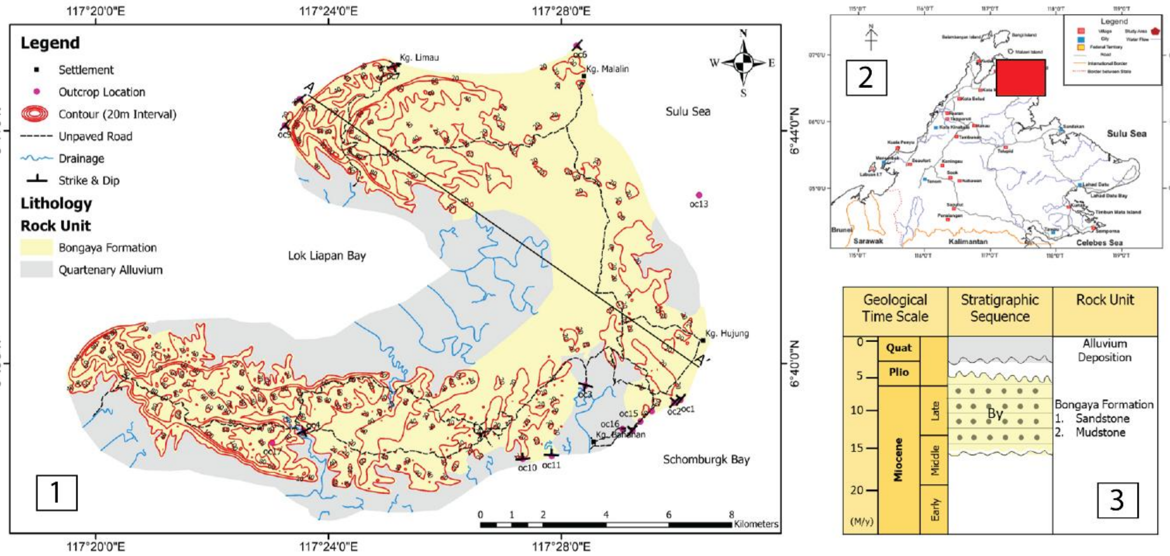

Figure 1. 1) Geological Map and locality of outcrops studied around Jambongan Island (QGIS 3.44). 2) Map of Sabah, Malaysia, indicating study area (red box). 3) General stratigraphy of study area.

MATERIALS AND METHODS

The research methodology collectively aims to achieve a comprehensive understanding of the geological characteristics, including sedimentology, stratigraphy, petrography, lithology, and geological history. The methodology integrates findings from previous research such as sedimentary logging, strike and dip measurements, and the assessment of faults and joints. An updated geological map was produced through the compilation of base maps, field data, information obtained from the Department of Mineral and Geoscience Malaysia (JMG). Additionally, stratigraphic correlation of the Bongaya Formation with the northeastern Sabah sequence was established by aligning sedimentary logs and sedimentary structures to refine the geological framework. Facies analysis and environmental reconstruction are done with accordance to Walker (1976) and Reading (1996).

RESULTS AND DISCUSSION

The sedimentary features observed are Hummocky Cross Stratification (HCS), Swaley Cross Stratification (SCS), parallel stratification, structureless sandstone and minor flaser bedding. Burrows are sparse and observed only at certain intervals / sandstone beds, particularly outcrop OC8, OC2 and OC10 (Figure 4). The sandstone commonly shows transition between HCS into parallel cross bedding. Ripple cross bedding can be observed topping the sandstone reflecting calm environment and transition to mudstone. Sandstone beds are thick, amalgamated and extend horizontally across the outcrops.

Facies Characterization

The six facies identified are 1) Hummocky Cross Stratified Sandstone (HCS), 2) Swaley Cross Stratified Sandstone (SCS), 3) Horizontally Stratified Sandstone (Sh), 4) Flaser Bedded Sandstone (FF), 5) Structureless Sandstone (Sm), & 6) Mudstone (M) (Table 1) (Figure 2 & 3).

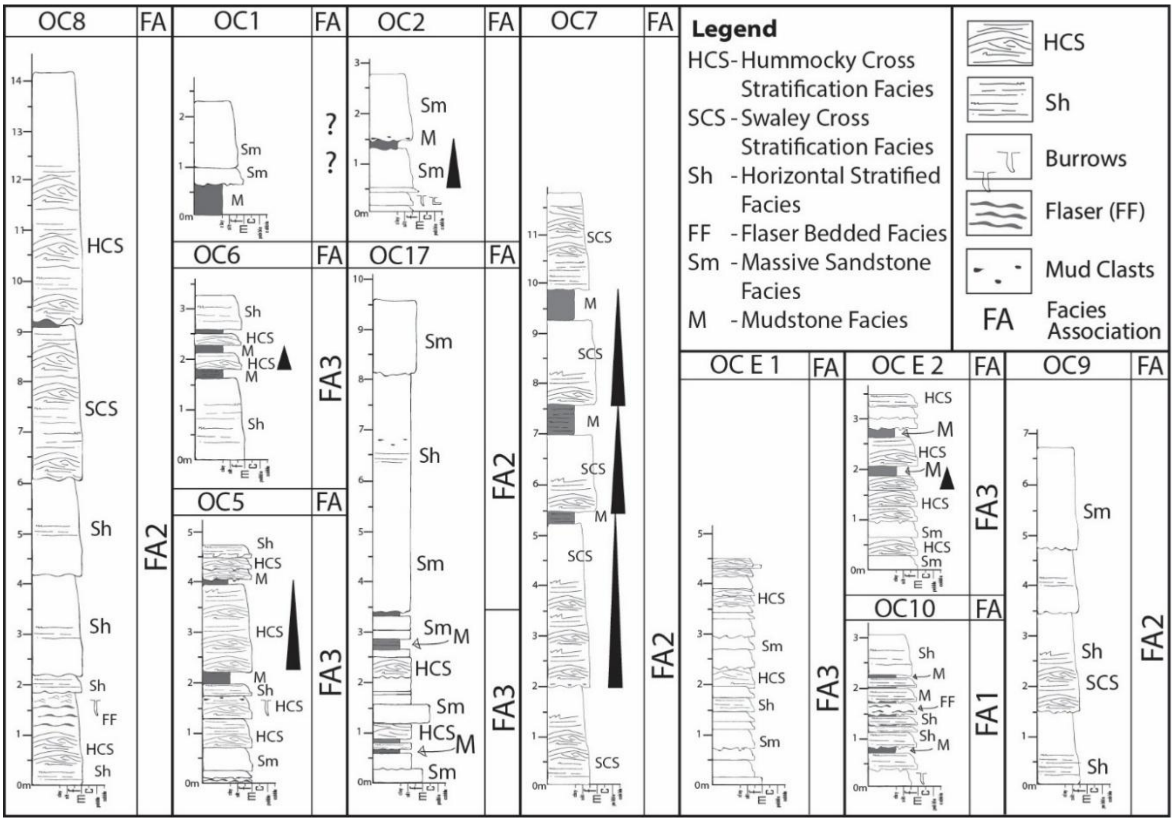

Figure 2. Logs of 11 outcrops at Jambongan Island

Table 1. Summary of identified facies.

Facies	Code	Grain Size	Thickness	Features	Fossils
Hummocky Cross Stratified Sandstone Facies	HCS	medium to fine	0.3m – 1.8m	Mud pebbles, fining upwards, irregular top and wavy bottom contacts	Ophiomorpha and skolithos linearis are common
Swaley Cross Stratified Sandstone Facies	SCS	medium to fine	1.5m – 2.0m	Fining upwards, wavy top and bottom contacts, transitional from and to Sh	Not observed
Horizontally Stratified Sandstone	Sh	medium to fine	~0.4m	Sharp bottom contacts, transitional from and to HCS and SCS	Not observed
Flaser Bedding Sandstone Facies	FF	medium to fine sand, mud flaser	~0.6m (0C8 & OC10)	Wavy top and sharp bottom contacts	Bioturbated
Structureless Sandstone Facies	Sm	medium to very fine	0.3m – 4m	Sharp contacts with overlying Sh, erosional base contacts with mud pebbles	Ophiomorpha and skolithos but uncommon
Mudstone Facies	M	clay	0.3m – 1.5m	Carbonaceous laminations, sharp bottom and irregular to wavy top contacts	Not observed

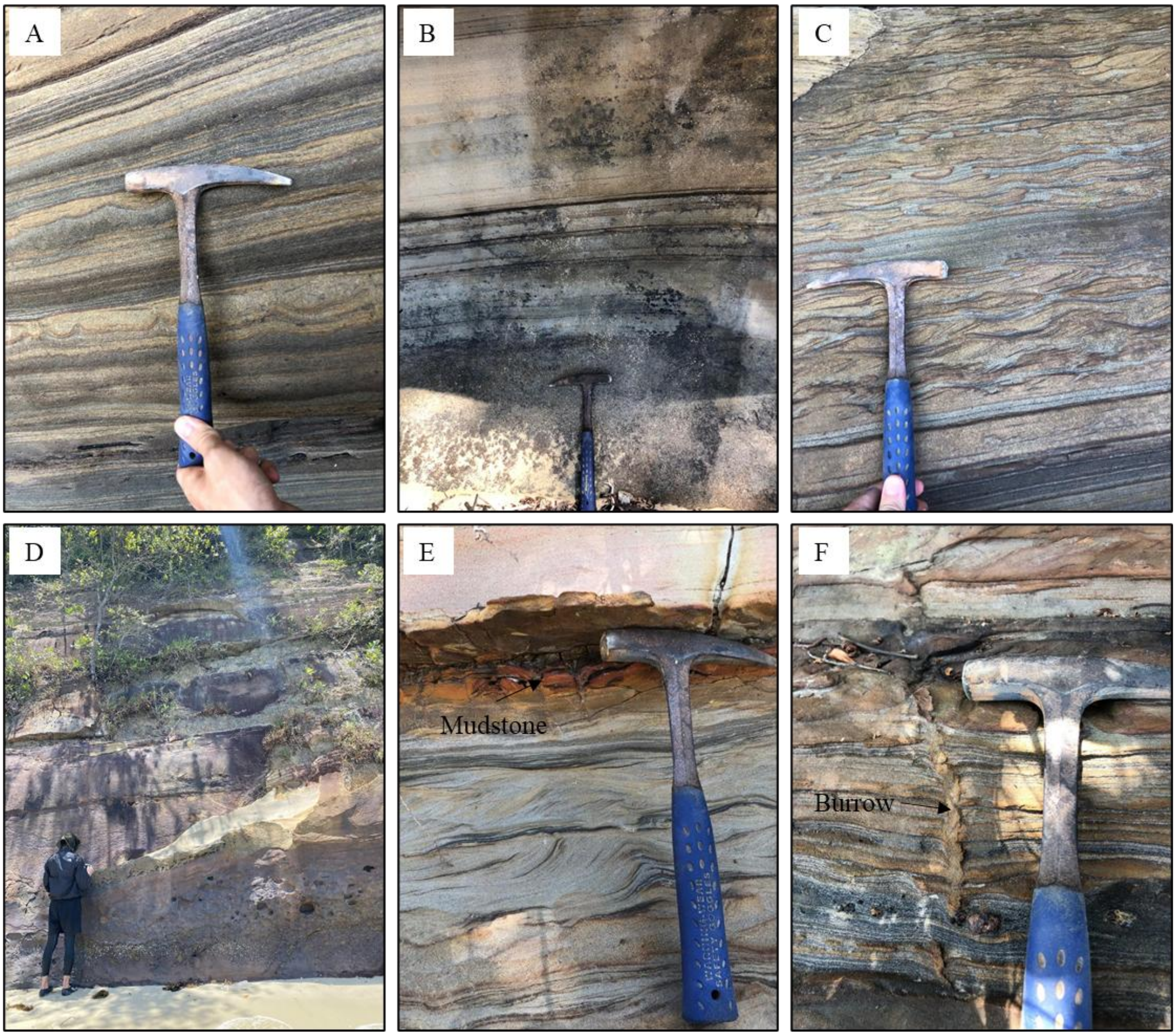

Figure 3. A) Hummocky Cross Stratified Sandstone (HCS), B) Horizontal Bedding (Sh), C) Flaser Bedding (FF), D) thick sandstone beds (Sm), E) rippled cross bedding, and F) burrow.

1) Hummocky Cross-Stratified Sandstone Facies (HCS)

This facies ranges from 0.3 m to 1.8 m in thickness and is medium- to fine-grained. Fining-upward trends are common in this facies. The bottom contact is irregular and wavy. Ophiomorpha and Skolithos linearis are commonly found. Mud pebbles with diameters less than 5 cm are commonly observed to align at the top and bottom of the HCS facies.

2) Swaley Cross-Stratified Sandstone Facies (SCS)

The SCS facies are defined as the stacking of two or more sets of HCS with visible top lap. These facies are fine- to medium-grained, with thickness ranging from 1.5m to 2.0m. It commonly shows fining-upward trends, wavy top and bottom contacts, and often transitions into the Sh facies. Fossils are not observed.

3) Horizontally Stratified Sandstone Facies (Sh)

This facies shows horizontal stratification with a sharp bottom contact. It also commonly occurs within thicker SCS and HCS sandstones with transitional contacts. This facies is thinly bedded, with 0.8m being the maximum thickness observed.

4) Flaser Bedded Sandstone Facies (FF)

This facies is minimal and is only observed at outcrops OC8 and OC10. Both occurrences are 0.6m thick. This facies signifies wave influence. It is common for wave-dominated facies not to be preserved in storm-dominated sequences due to intense erosion from wave action.

5) **Structureless Sandstone Facies (Sm)**

This facies ranges from 0.3m to 4m in thickness and is medium- to fine-grained. It is observed to fine upward into the Sh facies. Mud pebbles are occasionally present at the 6m to 7m interval at OC17. The structureless nature may be due to rapid deposition and high sediment supply. Parallel lamination is commonly present within this facies, signifying a decrease in sediment input or environmental energy. Ophiomorpha is present but not common.

6) **Mudstone Facies (M)**

Mudstone beds are subordinate and not common. Thickness averages 0.3m and does not exceed 1.5m. Carbonaceous laminations are commonly present. Thin mudstone beds indicate low-energy conditions and sediment settling through suspension.

Facies Association

Three distinctive facies associations were identified from the sedimentary logs across Jambongan Island. These comprise a thinly interbedded horizontally laminated sandstone and mudstone sequence (FA1; foreshore to backwash), thick sandstone sequence (FA; middle shoreface), and medium to thin sandstone sequence (FA3; lower shoreface). Notably, the distal shelf-to-transition zone of the shoreface succession is not observed in the study area, as the characteristic thick mudstone intervals and lenticular HCS sandstone beds are absent.

Facies Association 1: Thinly interbedded horizontally laminated sandstone and mudstone sequence (foreshore to backwash)

Facies Association 1 (FA1) consists of dominant, thinly interbedded horizontally laminated sandstones (Sh), with subordinate mudstone (M) and rare flaser bedding (FF). Restricted to the middle section of Outcrop OC10, these Sh facies are interpreted as upper-flow-regime deposits characteristic of the swash and backwash zone. This facies association represents the highest energy reach of the shoreface, where constant winnowing by wave action yields well-sorted and often coarser sand fractions compared to the other shoreface units (Clifton, 2006).

The minor mudstone and flaser bedding indicate localized and intermittent slack-water conditions. This suggests a potential within a backshore runnel or a protected portion of the upper intertidal zone. As the crucial unit in a progradational shoreface succession, the foreshore is situated between the mean high-water and mean low-water marks, frequently incorporating fine organic debris from terrestrial vegetation (Di Celma *et al.*, 2017). Despite its high-energy origin, the preservation potential of this facies is typically low due to subaerial exposure and reworking by subsequent transgressive ravinement processes (Zecchin *et al.*, 2025).

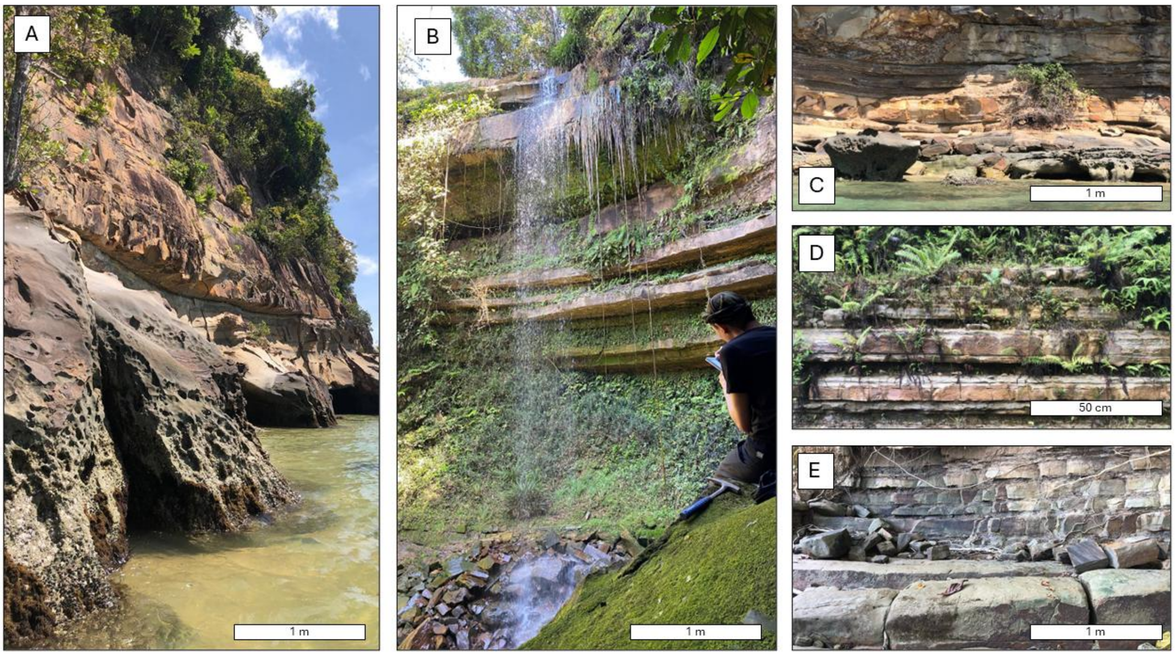

Figure 4. Selected Outcrop Photos with Sedimentary Log Locations. A), C), & E) OC7, OC 8, & OC10-located along the east coast; B) OC17-a waterfall outcrop located in the heart of Jambongan Island; E) OC4-roadside outcrop exhibiting thinly bedded sequence.

Facies Association 2: Thick sandstone sequence (middle – upper? shoreface)

Facies Association 3 (FA2) represents a prominent, sand-rich interval characterized by thick, amalgamated swaley (SCS) and structureless (Sm) sandstone beds. The succession exhibits a significant range in thickness (6m to16m) suggesting a sustained period of high sediment supply coupled with sufficient accommodation to allow for vertical aggradation. The main sedimentary structure in FA2 is swaley cross-stratification (SCS) which indicates deposition in an environment subject to intense, high-frequency wave action. Unlike hummocky cross-stratification (HCS) found in more distal settings, the prevalence of SCS suggests a position above the fair-weather wave base where the scouring of hummocky tops is common, leaving behind a record of amalgamated swales (Dumas and Arnott, 2006).

FA2 also contains structureless (massive) sandstone beds. These are interpreted as the result of rapid sedimentation from high-density suspension clouds, likely during the peak major storm events where the deposition rate exceeded the time required for bedform development (Plint, 2010).

Interspaced in within FA2 is marked by the presence of intraformational mud clasts occurring at the base of aggradational sets. These clasts represent the erosion and reworking of thin, fair-weather mudstone drapes by high-energy surges, a process typical of proximal and middle shoreface settings (MacEachern and Bann, 2008). The overall scarcity of preserved mudstone interbeds confirms a high-energy regime characterized by constant winnowing and amalgamation, where successive wave cycles remove finer-grained sediments, resulting in the characteristic clean, sand-dominated architecture of the middle shoreface (Walker and Plint, 1992).

Facies Association 3: Medium to thin sandstone sequence (lower shoreface)

Facies association 3 (FA3) is characterized by a rhythmic succession of moderately thick (~1m) hummocky cross-stratified (HCS) sandstones and structureless (massive) sandstones, with subordinate horizontally stratified sandstone (Sh) and thin mudstone (M) interbeds. This lithofacies assemblage is interpreted to deposit in lower shoreface environment, situated between the fair-weather wave base (FWWB) and the storm wave base (SWB). In this setting, the depositional process is dominated by episodic, high-energy storm events that transport sand basinward with alternating protracted periods of low-energy fair-weather conditions (Dumas and Arnott, 2006).

The moderately thick HCS beds reflect combined-flow conditions where large-scale orbital wave ripples are modified by unidirectional currents during storm peaks. The presence of structureless sandstones suggests rapid deposition during surge of sediment input (Plint, 2010). While thin mudstone interbeds represent the background fair-weather sedimentation. Unlike in the amalgamated middle shoreface, storm events were not always erosive enough to entirely remove the fair-weather record (Pemberton and MacEachern, 1997). The overall bed thickness and sand-to-mud ratio in this FA are primarily controlled by the duration and intensity of storm currents and sediment supply (Walker and Plint, 1992).

Depositional Model

Based on the sedimentary logs and facies analysis, the depositional environment is interpreted as a high-energy, wave-dominated shoreface system (Figure 5). The stratigraphic architecture is characterized by a progradational and coarsening-upward sequence that transitions from the lower shoreface (FA3) into the middle shoreface (FA2). This vertical stacking pattern suggests a seaward migrating shoreline, where shallower deposits gradually overlie deeper and lower-energy units. The succession follows a high-energy model because of the thick, amalgamated sandstone bodies, reaching up to 16m as shown by the presence of storm-driven structures like hummocky (HCS) and swaley (SCS) cross-stratification. Notably, the distal shelf-to-transition zone is missing in the study area, which suggests that fair-weather muds and thin storm sands were either bypassed or eroded by powerful storm currents during rapid progradation.

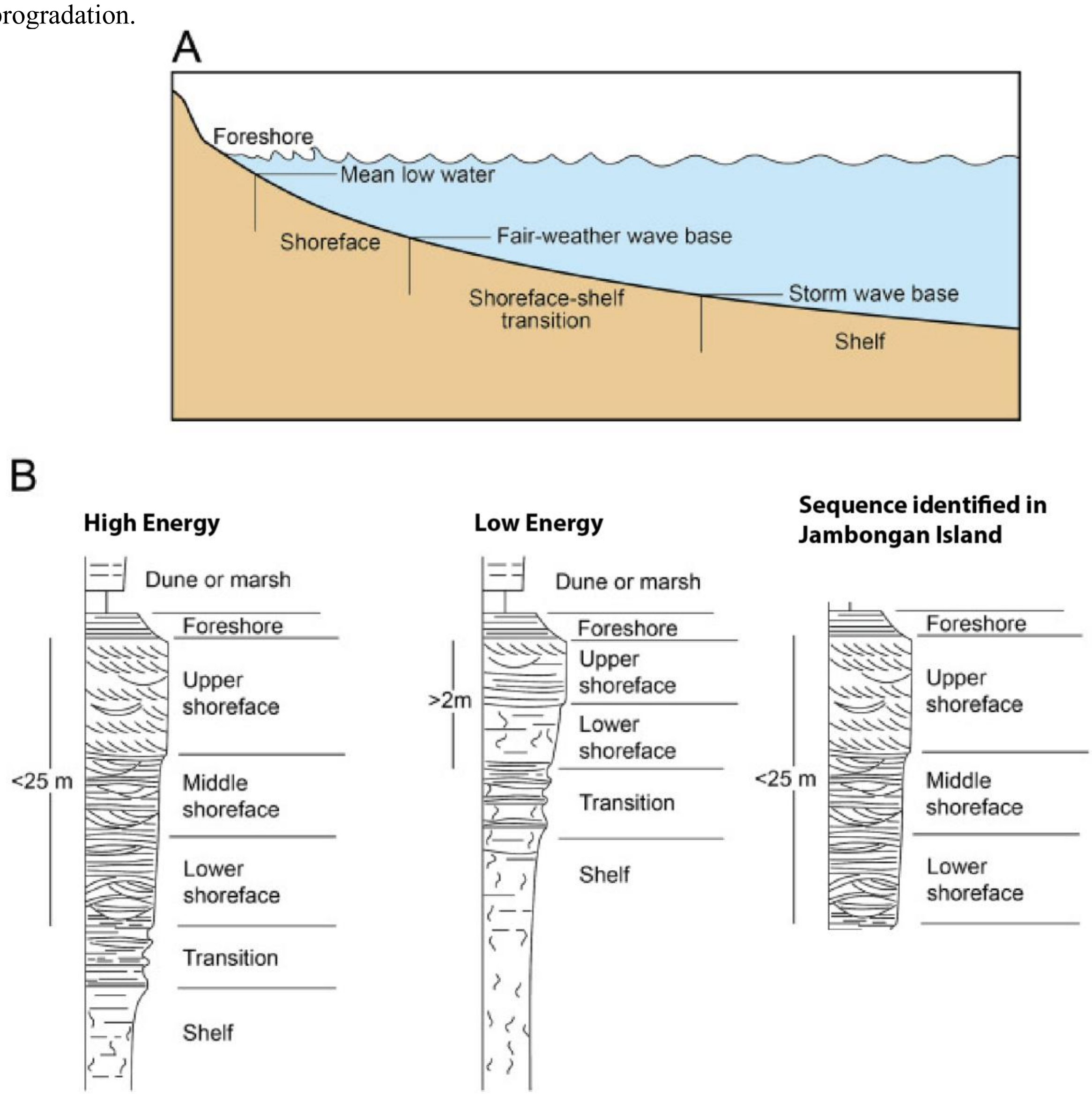

Figure 5. A) A coastal profile showing foreshore, shoreface and shelf with relation to FWWB and SWB. B) High-energy and low-energy succession with sequence identified at Jambongan Island (after Galloway and Hobday, 1996)

The energy deposition is clearly seen in the transition from the lower shoreface (FA3) up into the middle shoreface (FA2) and foreshore (FA1). FA3 consists of repeating and moderately thick HCS sandstones with thin mudstone layers. This indicates deposition below the FWWB where calm periods allowed mud to settle. As the sequence progrades into FA2, the beds thicken and coarsen into amalgamated SCS and massive sandstones (Sm), marking a shift to shallower water where constant wave action removed fine-grained sediments. The succession is then capped by the foreshore-to-backwash deposits of FA1, featuring horizontally laminated sandstone (Sh).

These findings align with the depositional model proposed by Galloway and Hobday (1996), which describes how high-energy shoreface systems produce thick and sand-dominated vertical successions. The shoreface is a seaward-sloping and wave-dominated wedge of sediment that extends from the low-tide mark down to the FWWB (Howell, 2005; Walker & Plint, 1992; Zecchin et al., 2025). In this environment, the water movement is very strong because of waves and longshore currents or storms. This environment is characterized by a high-energy hydrodynamic regime where sediment distribution is primarily governed by the interaction of oscillatory wave currents, longshore currents, and episodic storm events. In a vertical stratigraphic succession, shoreface deposits typically manifest as a coarsening-upward sequence, reflecting the progradation of shallower and higher energy facies over distal deposits (Walker and Plint, 1992).

CONCLUSION

This investigation identifies the Bongaya Formation on Jambongan Island as a high-energy, wave-dominated shoreface system deposited during the late Miocene to early Pliocene. Stratigraphic analysis reveals a distinctive coarsening-upward sequence that transitions from rhythmic, storm-deposited lower shoreface facies (FA3) into amalgamated, swaley middle shoreface sandstones (FA2), capped by high-energy foreshore deposits (FA1). The dominance of thick, amalgamated sandstone bodies-reaching up to 16m- and the lack of preserved distal transition zone mudstones support a high-energy depositional model. This research refines the geological framework of the Northeast Sabah Basin, providing a valuable foundation for future studies regarding the reservoir quality and structural evolution of North Borneo's circular pull-apart basin.

ACKNOWLEDGEMENT

The authors would like to express our profound gratitude to Universiti Malaysia Sabah (UMS), specifically through Grant SLB 2245 for funding this research. We would also like to thank UMS Geology staff for their support throughout this project. Finally. We extend our highest appreciation to the reviewers for their constructive comments, which greatly improved the manuscript.

REFERENCES

Clifton, H.E. 2006. A re-examination of facies models for clastic shorelines. *SEPM Special Publication*. https://doi.org/10.2110/pec.06.84.0293

Di Celma, C., Malinverno, E., Bosio, G. & Collareta, A. 2017. Sequence stratigraphy and paleontology of the Upper Miocene Pisco Formation along the western side of the lower Ica valley (Ica desert, Peri). *Rivista Italiana Di Paleontologia E Stratigrafia*, 123(2): 255-273. https://doi.org/10.13130/2039-4942/8373

Dumas, S. & Arnott, R.W.C. 2006. Origin of hummocky and swaley cross-stratification during the combined-flow regime. *Journal of Sedimentary Research*, 76(1): 51-69. https://doi.org/10.1130/G22930A.1

Galloway, W.E. & Hobday, D.K. 1996. Terrigenous Clastic Depositional Systems – Applications to Fossil Fuel and Groundwater Resources, second ed. Springer, New York, p. 489. http://doi.org/10.1007/978-3-642-61018-9

Howell, J. 2005. Sedimentary Environments: Shoreline and shoreface deposits. In Encyclopedia of Geology, Elsevier Inc: 570-579. https://doi.org/10.1016/B0-12-369396-9/00494-9

Lim, P. S. 1981. Wullersdorf Area, Sabah, Malaysia. Geological Survey of Malaysia. Report 15.

MacEachern, J.A. & Bann, K. L. 2008. The role of ichnology in refining shallow marine facies models. SEPM Special Publication 90, 90 – 116. https://doi.org/10.2110/jsr2020.41

Nor Aainaa Farhana Azam, Khairul Azlan Mustapha & Mohammed Hail Hakimi. 2024. Organic geochemical and petrological investigations of the upper Miocene Bongaya formation in the pitas, onshore sabah basin, and its relevance for hydrocarbon potential. *Journal of Petroleum Exploration and Production Technology*, 14: 2669-2685. https://doi.org/10.1007/s13202-024-01843-2

Pemberton, S.G. & MacEachern, J.A. 1997. The ichnological signature of storm deposits, the use of trace fossils in event stratigraphy. In: Paleontological Events, Stratigraphic, Ecology and Evolutionary Implications (Eds C.E. Brett and G.C. Baird), Columbia University Press, New York: 73-103.

Plint, A.G. 2010. Wave- and storm-dominated shoreline and shelf systems. In Facies Models *4*, edited by James, N.P. & Dalrymple, R.W. Geological Society of Canada, St. John's: 167-200.

Reading, H.G. 1996. Sedimentary Environments: Processes, Facies and Stratigraphy (3rd ed.). Blackwell Science.

Sanudin Hj. Tahir & Baba Musta. 2007. Pengenalan Kepada Stratigrafi. Penerbit UMS, Kota Kinabalu, Sabah.

Tongkul, F. 1991. Tectonic evolution of Sabah, Malaysia. In: Nichols, G. and Hall, R. (eds.) Proceedings of the Orogenesis in Action conference London 1990. *Journal of Southeast Asian Earth Sciences*. 6, pp. 395-405.

Walker, R.G. 1976. Facies Models. Geoscience Canada, 3(1), 21-24.

Walker, R.G., & Plint, A.G. 1992. Wave- and storm-dominated shallow marine systems. In Facies Models: Response to Sea Level Change (Walker, R.G. & James, N.P., Eds.), Geological Association of Canada, GeoText 1, Newfoundland: 219-238.

Zecchin, M., Catuneanu, O. & Caffau, M. 2025. Sequence stratigraphy of wave-dominated and wave-influenced shoreface deposits: Systems tracts, stratigraphy surfaces and facies contracts. *Sedimentary Geology*. https://doi.org/10.1016/j.sedgeo.2025.106980

RESEARCH ARTICLE

BORNEO SCIENCE
THE JOURNAL OF SCIENCE & TECHNOLOGY

Journal homepage: https://jurcon.ums.edu.my/ojums/index.php/borneo-science

FABRICATION AND CHARACTERIZATION OF CHITOSAN/TiO_2 MEMBRANES FOR SCENEDESMUS REMEDIATION: A PRELIMINARY STUDY

Mohamad Wafiuddin Ismail*[1], Husna Sophea Haszlihisham[2], Normawaty Mohammad Noor[3], Saiful Arifin Shafiee[4], Roziawati Mohd Razali[5] and Norazmi Ahmad[6]

[*1, 2, 4, 6] Department of Chemisty, Kulliyyah of Science, International Islamic University Malaysia, Pahang, Malaysia.
[3] Department of Marine, Kulliyyah of Science, International Islamic University Malaysia, Pahang, Malaysia
[5] Fisheries Research Institute Malaysia, Batu Maung, 11960 Bayan Lepas, Penang, Malaysia

*** Correspondence:**
wafisnj@iium.edu.my

Received: 23 February 2026
Revised: 26 May 2026
Accepted: 28 May 2026
Published online:
30 March 2026

Doi :
10.51200/bsj.v47i1.7401

Keywords:
Harmful algal blooms, chitosan, titanium dioxide, membrane, mitigation

ABSTRACT. *Excess nutrients from human activities have triggered harmful algal blooms (HABs), degrading water quality and ecosystem health. Traditional control methods like ultrasonication and chemical coagulants are limited by high costs and risks of secondary pollution. To address these challenges, this study investigates the use of polymeric membranes as a cost-effective and sustainable solution. In this preliminary study, porous chitosan/TiO_2 composite membranes were fabricated and evaluated as immobilized membrane materials for Scenedesmus removal. The purpose of the work was to establish the baseline performance of chitosan membranes containing immobilized TiO_2 and to compare the effect of TiO_2 loading on membrane-assisted algal removal. Fourier transform infrared spectroscopy (FTIR) confirmed the presence of chitosan functional groups and indicated TiO_2 incorporation through Ti-O-related absorption in the 467–457 cm^{-1} region. Thermogravimetric analysis (TGA) showed that TiO_2-containing membranes exhibited lower overall mass loss than the chitosan-only membrane, with the 1:2 chitosan/TiO_2 formulation showing the lowest reported total mass loss of 49.61%, suggesting the contribution of inorganic TiO_2 to the residual mass and thermal resistance of the composite. Scenedesmus removal was assessed by hemocytometer counting at 30 min, 1 h, 4 h, and 8 h. The processed average removal efficiencies were 37.64% for chitosan, 42.63% for 1:1 chitosan/TiO_2, and 60.56% for 1:2 chitosan/TiO_2. The observed removal is interpreted primarily as an overall membrane-assisted removal effect involving adsorption and physical entrapment within the porous chitosan scaffold, with a possible TiO_2 assisted contribution. The chitosan-based membranes demonstrated high algae removal efficiency, with chitosan alone achieving 37.64%, 1:1 chitosan/TiO_2 reaching 42.63%, and 1:2 chitosan/TiO_2 achieving the highest at 60.56%. The findings demonstrate the potential of porous chitosan/TiO_2 membranes as a preliminary platform for Scenedesmus mitigation and provide a basis for future mechanistic studies.*

INTRODUCTION

Algae, being photosynthetic organisms, are predominantly found in aquatic environments such as oceans, rivers, lakes, and ponds. They play a crucial role in oxygen production and have diverse applications in nutrition, pharmacology, and industry (Singh et al., 2023, Shabuddin et al., 2024). Algae exhibit a wide range of morphologies, from microscopic unicellular species to large multicellular forms reaching several meters in length. However, under favorable conditions, excessive algal growth can lead to the formation of harmful algal blooms (HABs) (Newton & Melaram, 2023; Khan et al., 2025).

A severe HAB event at Clear Lake, California, recorded microcystin toxin concentrations as high as 160,378 µg/L, posing serious threats to aquatic ecosystems and public health (Solomon et al., 2022). This alarming incident underscores the growing global threat of HABs, which contaminate water sources, disrupt aquatic ecosystems, and jeopardize public safety. The increasing occurrence of HABs is largely attributed to climate change, excessive nutrient loading, and other anthropogenic activities (Sarkar, 2018). One major anthropogenic driver of HAB formation is eutrophication, primarily caused by agricultural runoff, which enriches water bodies with nutrients, particularly nitrogen, thereby promoting algal overgrowth (Albou et al., 2024). These nutrients are washed into streams and rivers, creating favorable conditions for HAB proliferation (Lan et al., 2024).

According to UNESCO, approximately 300 species of microalgae are known to cause blooms, with around 75 of these producing harmful toxins. These toxins can be transmitted to humans through the consumption of contaminated seafood, resulting in health issues such as vomiting, diarrhea, and dizziness (Oh et al., 2023). Additionally, HABs contribute to widespread fish kills by depleting oxygen levels and obstructing light penetration, which hinders photosynthesis and leads to hypoxia. Such ecological disruptions also have severe economic impacts, particularly in communities reliant on fisheries. Consequently, various mitigation methods have been developed to control HABs. Conventional approaches such as ultraviolet (UV) radiation, ultrasonication, coagulant application, and the use of algicidal bacteria have demonstrated efficacy in reducing HAB levels. However, these methods face challenges including the potential release of harmful substances such as microcystins, high operational costs, and the generation of secondary contaminants in aquatic systems (Li et al., 2020).

Photocatalysis using titanium dioxide (TiO_2) nanoparticles has emerged as a promising strategy for algae mitigation due to its excellent photocatalytic activity, cost-effectiveness, and corrosion resistance (Natarajan et al., 2018). Nonetheless, practical application of TiO_2 under solar irradiation is limited by difficulties in separating the nanoparticles from treated water and concerns about their potential toxicity to aquatic life if released into the environment (He et al., 2020). These limitations can be addressed by immobilizing TiO_2 onto suitable support materials such as polymer films and porous polymers. Various polymers have been explored for this purpose in water treatment and antifouling applications. For example, poly(methyl methacrylate)-TiO_2 membranes have demonstrated significant photocatalytic activity, degrading up to 82.3% of methyl orange dye (Bhattacharyya et al., 2023), while polyethylene glycol-polyvinylidene fluoride/TiO_2 nanocomposite coatings have shown high efficiency in antifouling applications (Zhang et al., 2024).

This study investigates the effectiveness of TiO_2 immobilized on chitosan membranes for the removal of both harmful algae. To the best of our knowledge, no prior studies have examined the use of chitosan/TiO_2 composite membranes mitigation of HABs. Chitosan was selected as the membrane material due to its biocompatibility, biodegradability, and cost-effectiveness. Its porous structure has shown excellent performance in various water treatment applications, including oil/water separation (Su et al., 2017; Wang et al., 2024). The chitosan/TiO_2 composite membranes, prepared with a sponge like architecture, are hypothesized to effectively absorb harmful algae while preventing secondary contamination. In this system, the polymeric matrix absorbs the pollutants, and the embedded TiO_2 nanoparticles undergo photocatalytic reactions to generate reactive oxygen species, which degrade algal cells. The use of biodegradable polymers enhances environmental safety and sustainability, ensuring minimal ecological impact while maintaining high remediation efficiency. The present study focuses on the fabrication, characterization, and preliminary evaluation of chitosan/TiO_2 composite membranes for Scenedesmus removal.

MATERIALS AND METHODS

MATERIALS

Chitosan powder medium molecular weight was acquired from Sigma Aldrich. Titanium dioxide (TiO_2) nanopowder with particle size <100 nm, acetic acid (CH_3COOH), sodium hydroxide (NaOH) and acetic acid were obtained from Sigma Aldrich. All chemicals were used as received without further purification.

METHODS

Fabrication of Chitosan/TiO_2 Composite Membranes

Chitosan/TiO_2 composite membranes with different ratios were fabricated and the amounts of chitosan and TiO_2 used in the preparation of each composite membrane are detailed in Table 1. Various ratios were employed to investigate the optimal incorporation of the TiO_2 in the membranes for the algae mitigation.

Table 1. Amounts of polymers used for chitosan/TiO2 composite membranes

Types	**Amount used (g)**	
	Chitosan	**TiO_2**
Chitosan	1.00	-
1:1 Chitosan/TiO_2	1.00	1.00
1:2 Chitosan/TiO_2	1.00	2.00

Accurately weighed amounts of chitosan powder and TiO_2 were mixed and dissolved in 50 mL of 1% (v/v) acetic acid to form solution A, which was then stirred for 1 hour. Separately, 2 g of NaOH was dissolved in 50 mL of deionized water to produce solution B. To synthesize the chitosan membrane, solution A was added to solution B slowly at room temperature, and the mixture was stirred at 350 rpm until a precipitate formed. The resulting precipitate was collected using filter paper, transferred into a petri dish, and frozen overnight at - 40 °C. The frozen chitosan sponge was subsequently freeze-dried at - 40 °C for 24 hours to obtain the final membrane.

Preparation of Scenedesmus Culture

The procedure began with the preparation of Bold's Basal Medium (BBM) following the method described by Lyod et al. (2021), followed by the autoclaving 1-L conical flasks for sterilization. The flask was then filled with 200 mL of BBM and 200 mL of Scenedesmus stock culture. Aeration was supplied to both flasks, which were covered with cotton wool and aluminum foil to minimize the risk of contamination. The cultures were incubated undisturbed for one week to promote algal growth. Algal cell density was monitored by counting the number of cells using a hemocytometer.

Scenedesmus Removal Experiment

The algae mitigation experiment was conducted in an autoclaved 100 mL beaker containing 50 mL of Scenedesmus culture. The culture was maintained at 24 h light cycle and temperature of ± 27oC. Membrane samples were cut to a uniform size of 1.5 cm x 1.5 cm. Each membrane type was tested with three replicates (n = 3) and one control (without membrane). The experiment evaluates overall membrane-assisted Scenedesmus removal under ambient laboratory/culture-light conditions. At selected time intervals (0 minutes, 30 minutes, 1 hour, 4 hours, and 8 hours), approximately 1 mL of the cell culture was withdrawn from a depth of 2 cm below the surface. Prior to sampling, the beakers were gently swirled to ensure homogeneity. Cell concentration of Scenedesmus was determined using a hemocytometer under a light microscope. For each sample, two 1 mL aliquots were counted, and the average cell count was calculated to enhance accuracy. The removal efficiency (RE) of each membrane in mitigating algae growth was calculated using Equation 1. where RE represents the removal efficiency of Scenedesmus cells (%), C_0 represents the initial cell concentration before membrane treatment (cells/mL), and C_t represents the cell concentration after treatment at time t (cells/mL). The treatment time, t, refers to the sampling intervals of 30 min, 1 h, 4 h, and 8 h. Cell concentration was determined using a hemocytometer and reported as cells/mL

$$\text{RE (\%)} = \frac{c_0 - c_T}{c_0}\ x\ 100 \quad \text{(Equation 1)}$$

Composite Membrane Characterization

Fourier Transform Infrared Spectroscopy (FTIR)

FTIR analysis was conducted to investigate the chemical structure of the membranes and to confirm the successful incorporation of TiO_2, indicated by the presence of Ti–O stretching vibration peaks. The instrument used was a PerkinElmer Frontier FTIR spectrometer. Spectra were recorded over the range of 400–4000 cm^{-1}. Membrane samples were finely ground and mixed with potassium bromide (KBr) at a ratio of 1:20. The homogenized mixture was placed into a pellet die and subjected to a pressure of 10 tons using a hydraulic press to form a pellet. The FTIR spectrum of the sample was then recorded.

Thermogravimetric Analysis (TGA)

Thermogravimetric analysis (TGA) was performed to assess the thermal stability and decomposition behavior of the composite membranes. A Shimadzu TGA-50 Thermogravimetric Analyzer was used for the analysis. The temperature was programmed to increase from 25 °C to 700 °C at a heating rate of 10 °C/min. A constant gas flow of 50 mL/min was maintained to ensure a stable inert atmosphere during the analysis.

Scanning Electron Microscopy (SEM)

SEM analysis was used to examine the surface morphology, porosity, and dispersion of TiO_2 particles within the polymer matrix. A Carl Zeiss AG EVO 50 scanning electron microscope was employed for the imaging. Prior to analysis, the samples were coated with a thin layer of gold to enhance conductivity and image quality.

RESULTS AND DISCUSSION

Development of Porous Chitosan/TiO_2 Composite Membranes

Chitosan/TiO_2 composite membranes were prepared using the phase inversion method followed by freeze-drying to promote porosity. Initially, the chitosan solution (Solution A) was stirred for 1 hour to ensure complete dissolution. Upon adding Solution B to this acidic chitosan solution, rapid coagulation occurred due to ionic cross-linking, leading to the precipitation of chitosan. This process is driven by the deprotonation of the amino groups on chitosan upon exposure to a basic medium such as NaOH (Kou et al., 2021). The precipitated chitosan/TiO_2 coagulant was then frozen overnight and subsequently subjected to freeze-drying. Freeze-drying facilitated the formation of a porous, sponge-like architecture through the sublimation of ice crystals formed during freezing, yielding a macroporous matrix ideal for absorption applications (Guastaferro et al., 2021). This morphology is relevant for algal-removal applications because pores and internal channels can increase the opportunity for algal cells to contact the membrane and become physically retained.

The cross-sectional morphology of the resulting chitosan/TiO_2 membranes, as shown in Figure 1, revealed a layered structure with well-defined porosity, indicating enhanced surface area and potential for increased adsorption and photocatalytic activity. Notably, membranes fabricated with varying TiO_2 loadings did not exhibit significant morphological differences in terms of layer formation and thickness, which remained consistent across all formulations. This observation is in line with previous findings where TiO_2 incorporation at moderate concentrations did not significantly alter the structure of chitosan-based membranes (Xing et al., 2020).

Figure 1. Cross-sectional image of the chitosan/TiO_2 composite membrane showing the porous sponge-like architecture generated after freeze-drying.

Fourier Transform Infrared Spectroscopy (FTIR) was employed to confirm the incorporation of TiO_2 into chitosan composite membranes. The FTIR spectra of pure chitosan, 1:1 chitosan/TiO_2, and 1:2 chitosan/TiO_2 composites are presented in Figure 2. Chitosan shows characteristic absorption bands associated with its functional groups. The broad absorption peak observed at 3400–3200 cm^{-1} is assigned to the overlapping stretching vibrations of hydroxyl (–OH) and amine (–NH_2) groups. The amide I band appears at approximately 1635 cm^{-1}, while the amide II band is observed near 1401 cm^{-1}, indicating the presence of C=O stretching and N–H bending vibrations, respectively. A distinct band near 1117 cm^{-1} corresponds to asymmetric C–O–C stretching vibrations, characteristic of the polysaccharide backbone. These peaks were consistently observed in all chitosan-containing samples, indicating the retention of the polymer's primary functional groups after TiO_2 incorporation.

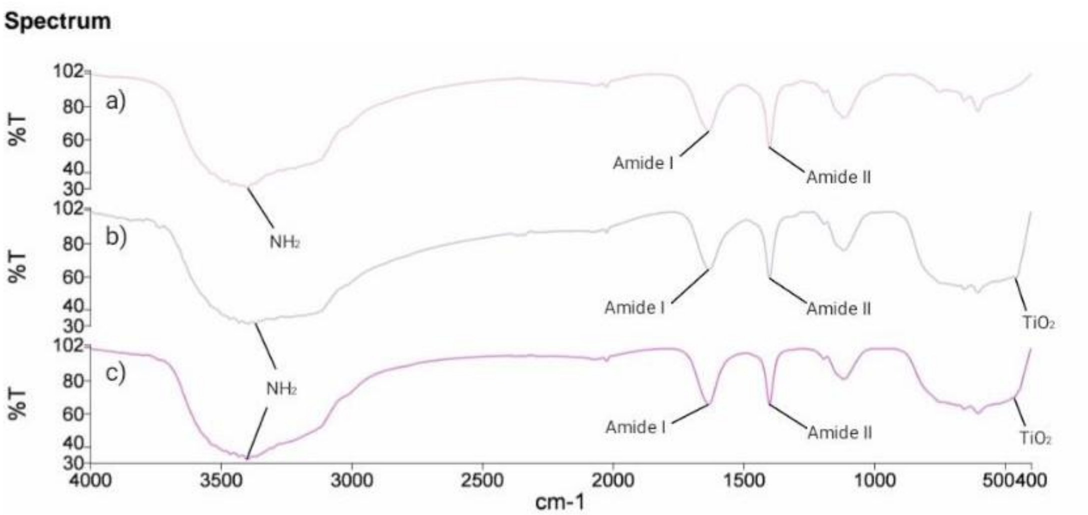

Figure 2. FTIR spectra for (a) chitosan, (b) 1:1 chitosan/TiO_2, and (c) 1:2 chitosan/TiO_2.

For the chitosan/TiO_2 composite membranes, an additional absorption feature in the 467–457 cm^{-1} region was observed and is assigned to Ti-O vibration from the TiO_2 lattice (Spoială et al., 2022). The presence of this band supports the incorporation of TiO_2 into the chitosan matrix. An increase in Ti-O band intensity with higher TiO_2 content is consistent with the greater TiO_2 loading in the 1:2 formulation. The interaction between chitosan and TiO_2 may also lead to minor shifts or changes in the intensity of the characteristic peaks due to potential hydrogen bonding or electrostatic interactions between the TiO_2 and chitosan. Previous studies have shown that the Ti–O–C or Ti–O–N bonds can be formed between TiO_2 and chitosan, further supporting their compatibility in composite formation (Habiba et al., 2019).

Thermogravimetric analysis (TGA) was performed to assess the thermal stability of pure chitosan and chitosan/TiO_2 composite membranes (Figure 3). The pristine chitosan membrane showed an initial mass-loss event beginning around 59.04 °C. This low-temperature event is attributed primarily to moisture evaporation and removal of physically adsorbed water rather than polymer backbone decomposition. Chitosan is hydrophilic because of its hydroxyl and amine groups, which can retain water through hydrogen bonding (Hussein et al., 2021). The main thermal-degradation region of chitosan occurs at higher temperature, commonly above approximately 200 °C, and is associated with degradation of the polysaccharide backbone, cleavage of glycosidic linkages, and release of volatile decomposition products (Mallakpour & Madani, 2015).

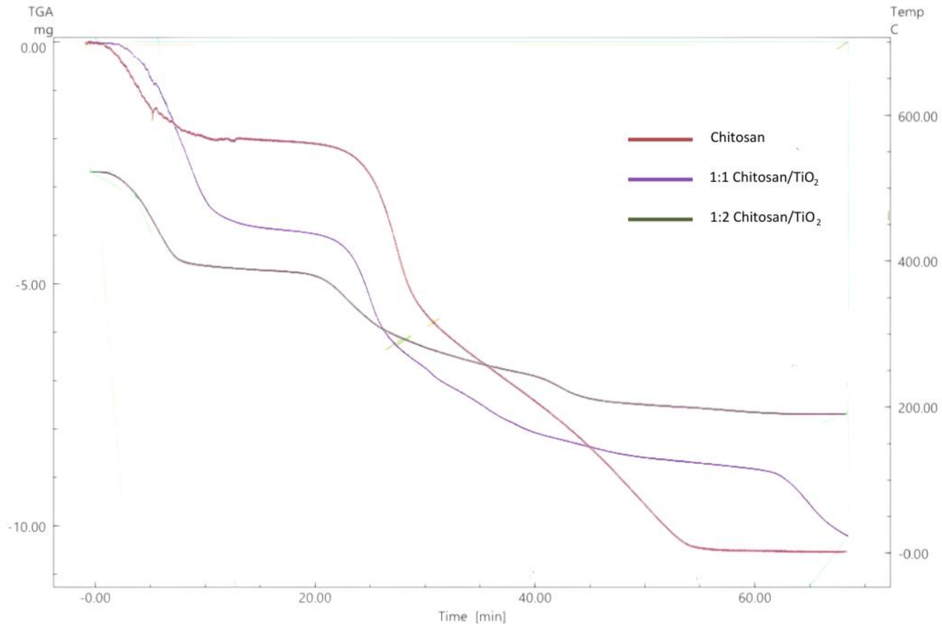

Figure 3. TGA spectra for chitosan, 1:1 chitosan/TiO_2, and 1:2 chitosan/TiO_2.

Upon incorporation of TiO_2, a notable enhancement in thermal stability was observed. The pristine chitosan membrane showed a high total mass loss of 89.36%, while the TiO_2-containing membranes showed lower total mass losses. The 1:1 chitosan/TiO_2 membrane showed a total mass loss of 57.29%, and the 1:2 chitosan/TiO_2 membrane showed the lowest total mass loss of 49.61%. The lower mass loss of the composite membranes is attributed to the inorganic TiO_2 fraction, which remains as thermally stable residue at high temperature, and to possible physical interactions between TiO_2 particles and chitosan chains. TiO_2 may restrict polymer-chain mobility and act as a heat-resistant inorganic component within the matrix (Hussein et al., 2021). The higher residual mass of the 1:2 chitosan/TiO_2 membrane is consistent with its higher TiO_2 loading. Similar trends have been reported for chitosan/TiO_2 systems, where TiO_2 incorporation increased residual mass and improved the apparent thermal resistance of the composite material (Becenan & Erdogan, 2022). TiO_2 incorporation into polymeric composites limits the volatilization of degradation products and insulates the polymer from further decomposition.

Scenedesmus Removal Performance

The Scenedesmus removal efficiencies of the chitosan, 1:1 chitosan/TiO_2, and 1:2 chitosan/TiO_2 membranes are summarized in Table 2 and illustrated in Figure 4. The data are reported as processed average removal efficiencies obtained under culture-light conditions. The pristine chitosan membrane exhibited lowest removal efficiency at an average of 37.64% compared to other membranes. This performance is attributed mainly to physical adsorption and entrapment of algal cells within the porous membrane structure. While the sponge-like morphology can retain cells through pore capture and surface adhesion, the presence of amine groups in chitosan promotes electrostatic interactions with the negatively charged algal cell membranes, enhancing retention (Park et al., 2020). The gradual increase in removal efficiency suggests that although the membrane is effective, its adsorption capacity is reached at a slower rate.

Table 2. Scenedesmus removal efficiency of chitosan/TiO_2 composite membranes.

Types	Removal Efficiency (%)				
	30 min	**1 hr**	**4 hrs**	**8 hrs**	**Average**
Chitosan	5.27±9.79	26.36±12.08	60.76±11.91	58.17±5.35	37.64
1:1 Chitosan/TiO_2	5.27±12.47	26.36±16.52	60.76±5.66	78.84±2.84	42.63
1:2 Chitosan/TiO_2	53.03±3.56	58.76±3.47	57.17±5.01	73.26±1.68	60.56

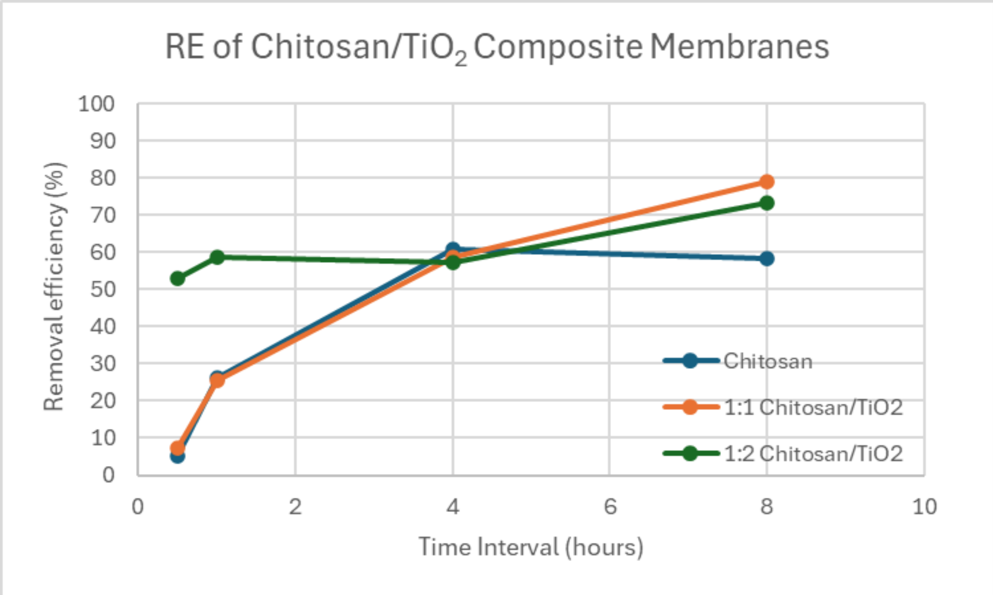

Figure 4. Scenedesmus removal efficiency of chitosan/TiO_2 composite membranes.

The incorporation of TiO_2 into the chitosan matrix significantly improved the removal performance. The 1:1 chitosan/TiO_2 membrane showed a slightly higher average removal efficiency of 42.63%, while the 1:2 chitosan/TiO_2 membrane showed the highest processed average removal efficiency of 60.56%. The improved performance of the TiO_2 containing membranes may be related to several factors, including additional inorganic surface sites, changes in membrane texture, and possible light assisted TiO_2 contribution under ambient culture light conditions. The 1:2 chitosan/TiO_2 membrane reached 53.03% removal as early as 30 min, suggesting rapid interaction between the algae suspension and the composite membrane. At later time points, the removal profile did not increase linearly at every interval, which may reflect sampling variability, cell aggregation, partial release of physically retained cells, or local differences in suspension homogeneity.

The performance of the membranes in this study can also be compared to previous work. Ibrahim et al. (2022) reported a removal efficiency of 76.1% over 72 hours using hybrid chitosan-modified TiO_2 films against Alexandrium minutum. In contrast, the 1:2 chitosan/TiO_2 membrane developed in this study achieved a comparable removal efficiency in only 8 hours, indicating a significantly faster removal rate. This difference may be attributed to differences in membrane morphology. Ibrahim et al.'s membranes, prepared via phase inversion technique, exhibited a dense and smooth structure, with TiO_2 nanoparticles embedded near the surface. Compact morphology limits active site accessibility and mass transfer. In contrast, the membranes in this study were fabricated using a freeze-drying method, resulting in a sponge-like, highly porous structure. This morphology offers a substantially larger surface area and better internal diffusion pathways, allowing greater contact between TiO_2 particles and algal cells. Furthermore, Natarajan et al. (2018) reported that a chitosan/TiO_2/Ag composite film achieved an algae viability reduction of 45.42 ± 0.36%. The 1:2 chitosan/TiO_2 membrane in the present study shows better results, likely due to its highly porous structure, which enhances algal entrapment.

Scanning Electron Microscopy (SEM) images were used to examine the morphology of the chitosan and chitosan/TiO_2 membranes (Figure 5). The images show a porous, sponge like structure with interconnected voids and layered features. This morphology is consistent with the freeze-drying process, where ice crystal formation and subsequent sublimation create pores and internal channels (Guastaferro et al., 2021).

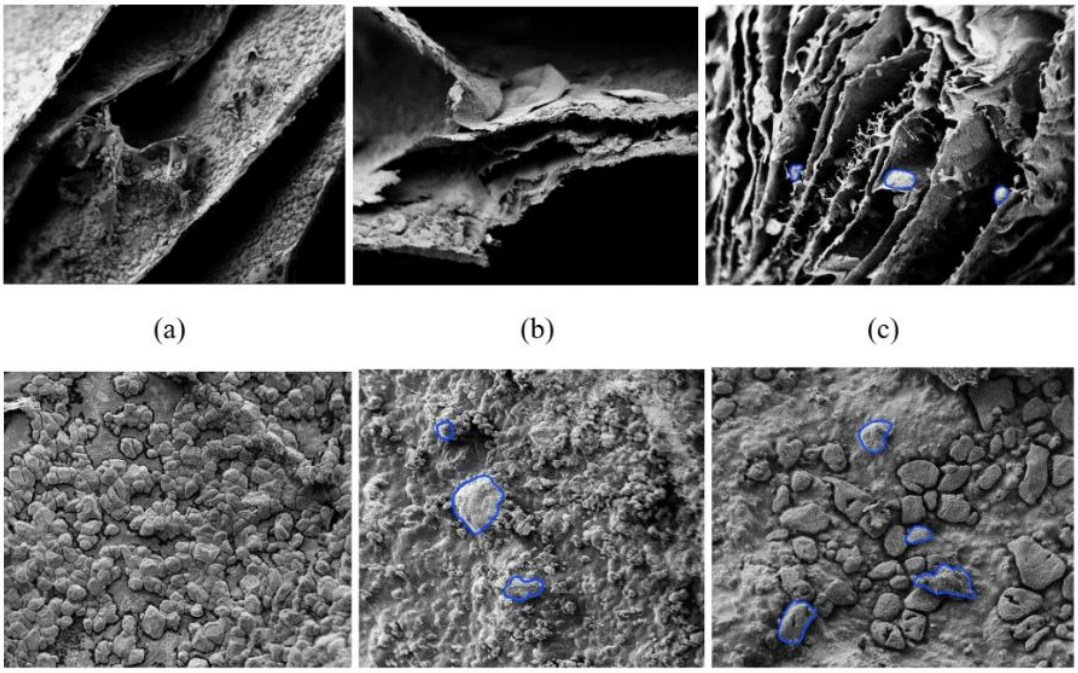

Figure 5. SEM images of (a) chitosan, (b) 1:1 chitosan/TiO2, (c) 1:2 chitosan/TiO2, above; cross-sectional at 100x magnification, bottom; surface at 300x magnification.

The resulting porous architecture is particularly advantageous for applications involving adsorption, as it promotes greater contact between the active membrane surface and target pollutants. The interconnected pore network enhances mass transport, facilitates diffusion of algal cells into the membrane structure, and improves retention capacity (Ikono et al. 2019), on the chitosan-TiO_2 composites. Particle like features are visible in the TiO_2 containing membranes, suggesting the presence of embedded inorganic particles within the chitosan matrix, which display distinct particle like features embedded within the pore walls. These features are indicative of successful TiO_2 incorporation into the biopolymeric scaffold. Uniform distribution of TiO_2 within the porous matrix is crucial, as it ensures that the potential photocatalytic sites are accessible to light and pollutants, thereby maximizing the generation of reactive oxygen species under light exposure. This incorporation is assumed to lead to improved photocatalytic efficiency and mechanical integrity of the newly developed membrane (Spoială et al., 2022; Esparza et al., 2020). Additionally, the morphology of the membrane plays a vital role in influencing not only physical adsorption but also light penetration. Open, porous structures allow deeper light penetration and more efficient utilization of embedded TiO_2, which is often a limitation in dense or non-transparent membranes

CONCLUSION

Porous chitosan/TiO_2 composite membranes were successfully fabricated using an alkaline precipitation and freeze drying approach and were preliminarily evaluated for Scenedesmus removal. FTIR analysis indicated the retention of chitosan functional groups and the incorporation of TiO_2 through Ti-O-related absorption bands. TGA showed reduced total mass loss and higher residual mass in TiO_2-containing membranes, particularly the 1:2 chitosan/TiO_2 membrane, reflecting the contribution of the thermally stable inorganic component. SEM observations confirmed a porous, sponge-like morphology that is favourable for contact and physical retention of algal cells.

The algae removal test showed that the 1:2 chitosan/TiO_2 membrane achieved the highest processed average removal efficiency of 60.56% within the 8 h evaluation period, followed by the 1:1 chitosan/TiO_2 membrane and the pristine chitosan membrane. These findings suggest that increasing TiO_2 loading may improve the overall membrane assisted removal performance. The main experimentally supported mechanism is physical entrapment/adsorption by the porous chitosan based membrane, while TiO_2 assisted effects remain possible but require further verification. Future work should focus on controlled photocatalytic testing, mechanistic controls, quantitative porosity, TiO_2 leaching, reusability, mechanical stability, kinetic modelling, and ecotoxicity assessment before practical environmental application.

ACKNOWLEDGEMENT

International Islamic University Malaysia and the Department of Fisheries for supported this research (12th Malaysia Plan Development Fund (22501-509).

REFERENCES

Albou, E.M., Abdellaoui, M., Abdaoui, A., Boughrous, A.A. 2024. Agricultural Practices and their Impact on Aquatic Ecosystems – A Mini-Review. *Ecological Engineering & Environmental Technology*, 25(1); 321-331.

Becenen, N. Erdogan S. 2022. Chitosan and nano-TiO_2 coating improves the flame retardancy of dyed and undyed denim fabrics by increasing the charring. *Journal of Industrial Textiles*, 51(1); 1252S-1278S

Bhattacharyya, S., Algieri, C., Davoli, M., Calabrò, V., Chakraborty, S. 2023. Polymer-based TiO_2 membranes: An efficient route for recalcitrant dye degradation. *Chemical Engineering Research and Design*, 193; 641–648.

Esparza, L.M., Gomez, J.M.R., Verdugo, C.I.M., Silva, N.G., Toledo, R.R., Aguirre, S.A., Larios, A.P. Gonzalez E.M. 2020. Chitosan-TiO_2: A Versatile Hybrid Composite. *Materials*, 13(4); 811.

Guastaferro, M., Baldino, L., Reverchon, E., Cardea, S. 2021. Production of Porous Agarose-Based Structures: Freeze-Drying vs. Supercritical CO_2 Drying. *Gels*, 7(4); 198.

Habiba, U., Joo, T.C., Shezan, S.K.A., Das, R., Ang, B.C. Afifi, A.M. 2019. Synthesis and characterization of chitosan/TiO_2 nanocomposite for the adsorption of Congo red. *Desalination and Water Treatment*, 164; 361-367.

He, X., Wang, A., Wu, P., Tang, S., Zhang, Y., Li, L., Ding, P. 2020. Photocatalytic degradation of microcystin-LR by modified TiO_2 photocatalysis: A review. *Science of the Total Environment*, 743.

Hussein, E.M., Desoky, W.M., Hanafy, M.F., Guirguis, O.W. 2021. Effect of TiO_2 nanoparticles on the structural configurations and thermal, mechanical, and optical properties of chitosan/TiO_2 nanoparticle composites. *Journal of Physics and Chemistry of Solids*, 152; 109983.

Ibrahim, N.H., Iqbal, A., Mohammad-Noor, N., Razali, R.M., Sreekantan, S., Yanto, D.H.Y., Mahadi, A.H., Wilson, L.D. 2022. Photocatalytic Remediation of Harmful Alexandrium minutum Bloom Using Hybrid Chitosan-Modified TiO_2 Films in Seawater: A Lab-Based Study. *Catalysts,* 12(7).

Ikono, R., Li, N., Pratama, N.H., Vibriani, A., Yuniarni, D.R., Luthfansyah, M., Bachtiar, B.M., Bachtiar, E.W., Mulia, K., Nasikin, M., Kagami, H., Li, X., Mardliyati, E., Rochman, N.T., Nagamura-Inoue, T., Tojo, A. 2019. Enhanced bone regeneration capability of chitosan sponge coated with TiO_2 nanoparticles. *Biotechnology Reports*, 24; e00350.

Khan, N., Bhowmilk, P.P., Sarker, M.S., Yang, H., Li, R. Liu, J. 2025. Impact of water quality parameters on harmful algal bloom mitigation and phosphorus removal by lab-synthesized $\gamma Fe_2O_3/TiO_2$ magnetic photocatalysts. *Algal Research*, v86; 103932.

Kou, S., Peters, L M., Mucalo, M.R. 2021. Chitosan: A review of sources and preparation methods. *International Journal of Biological Macromolecules*, 169; 85–94.

Lan, J., Liu, P., Hu, X., Zhu, S. 2024. Harmful Algal Blooms in Eutrophic Marine Environments: Causes, Monitoring, and Treatment. *Water*, 16(17), 2525.

Li, S., Tao, Y., Zhan, X. M., Dao, G. H., & Hu, H. Y. (2020). UV-C irradiation for harmful algal blooms control: A literature review on effectiveness, mechanisms, influencing factors and facilities. *Science of The Total Environment*, 723, 137986.

Lyod, C., Tan, K.H., Lim, K.L., Valu, V.G., Fun, S.M.Y, Chye, T.R., Mak, H.M., Sim, W.X., Musa, S.L., Ng, J.J., Nordin, N.S., Aidil, N.M., Eng, Z.Y.W., Manickavasagam, P. New, J.Y. 2021. Identification of microalgae cultured in Bold's Basal medium from freshwater samples, from a high-rise city. *Scientific Reports*, v11: 4474.

Mallakpour, S., Madani, M. 2015. Effect of Functionalized TiO_2 on Mechanical, Thermal and Swelling Properties of Chitosan-Based Nanocomposite Films. *Polymer-Plastics Technology and Engineering*, 54(10); 1035–1042.

Natarajan, S., Lakshmi, D.S., Thiagarajan, V., Mrudula, P., Chandrasekaran, N., Mukherjee, A. 2018. Antifouling and anti-algal effects of chitosan nanocomposite (TiO_2/Ag) and pristine (TiO_2 and Ag) films on marine microalgae Dunaliella salina. *Journal of Environmental Chemical Engineering*, 6(6); 6870–6880.

Newton, A.R. Melaram, R. 2023. Harmful algal blooms in agricultural irrigation: risks, benefits, and management. *Water*, 5:1325300.

Oh, J.W., Pushparaj, S.S.C., Muthu, M., Gopal, J. 2023. Review of Harmful Algal Blooms (HABs) Causing Marine Fish Kills: Toxicity and Mitigation. *In Plants*, 12(23).

Park, Y.H., Kim, S., Kim, H.S., Park, C., Choi, Y.E. 2020. Adsorption Strategy for Removal of Harmful Cyanobacterial Species Microcystis aeruginosa Using Chitosan Fiber. *Sustainability*, 12(11), 4587.

Sarkar, S. K. 2018. *Algal blooms: Basic concepts. In Marine algal bloom: Characteristics, causes, and climate change impacts* (pp. 1-52). Springer.

Shabuddin, S.H., Noor, M.N., Ahmad, M.N., Iqbal, A. Ismail, M.W. 2024. Development of PCL/PMMA and PCL/PEG polymeric film as potential for algae removal. *Sains Malaysiana*, 53 (6).

Singh, V.K., Jha, S., Rana, P., Mishra, S., Kumari, N., Singh, S.C., Anand, S., Upadhye, V., Sinha, R.P. 2023. Resilience and Mitigation Strategies of Cyanobacteria under Ultraviolet Radiation Stress. *International Journal of Molecular Sciences*, 24(15); 12381.

Solomon, G.M., Stanton, B., Ryan, S., Little, A., Carpenter, C., Paulukonis, S. 2022. Notes from the Field: Harmful Algal Bloom Affecting Private Drinking Water Intakes - Clear Lake, California, June–November 2021. *Morbidity and Mortality Weekly Report*; 71(41), 1306.

Su, C., Yang, H., Zhao, H., Liu, Y., Chen, R. 2017. Recyclable and biodegradable superhydrophobic and superoleophilic chitosan sponge for the effective removal of oily pollutants from water. *Chemical Engineering Journal*, 330; 423–432.

Spoială, A., Ilie, C.I., Dolete, G., Croitoru, A.M., Surdu, V.A., Trușcă, R.D., Motelica, L., Oprea, O.C., Ficai, D., Ficai, A., Andronescu, E., Dițu, L.M. 2022. Preparation and Characterization of Chitosan/TiO2 Composite Membranes as Adsorbent Materials for Water Purification. *Membranes,* 12(8).

Wang, Y., Feng, X., Ke, Y., Mo, J., Lin, J., Wang, J., Zhou, C., Gan, F., Wang, L., Ma, C. 2024. Silicone decorated polycaprolactone electrospun fibrous membranes for oil/water separation. *The Journal of The Textile Institute*, 115(5); 744–756.

Xing, Y., Li, X., Guo, X., Li, W., Chen, J., Liu, Q., Xu, Q., Wang., Yang, H., Shui, Y. Bi, X. 2020. Effects of Different TiO2 Nanoparticles Concentrations on the Physical and Antibacterial Activities of Chitosan-Based Coating Film. *Nanomaterials*, 10; 1365.

Zhang, C.M., Qiu, Y.Z., Wu, H., Guan, J., Wang, S.G., & Sun, X.F. 2024. Polyethylene glycol-polyvinylidene fluoride/TiO2 nanocomposite polymer coatings with efficient antifouling strategies: Hydrophilized defensive surface and stable capacitive deionization. *Journal of Colloid and Interface Science*, 666; 585–593.

RESEARCH ARTICLE

BORNEO SCIENCE
THE JOURNAL OF SCIENCE & TECHNOLOGY

Journal homepage: https://jurcon.ums.edu.my/ojums/index.php/borneo-science

GREEN SYNTHESIS OF COPPER OXIDE NANOPARTICLES TO HARVEST THE LIGHT FOR PHOTOCATALYTIC DEGRADATION OF DYES METHYLENE BLUE AND METHYL ORANGE

Faisal Shahzad[1*], Erum Hussain[2], Nahdia Nadeem[2,] Muhammad ikram Nabeel[3,4,5*], Muhammad Saeed[1], Collin G. Joseph[3,4], Muhammad Naseem[5], Asma Nisar[6], Muhammad Sajid[5]

[1]Department of Chemistry, Government College University Faisalabad

[2]Department of Chemistry, Government College Women University Faisalabad

[3]Industrial Chemistry Programme, Faculty of Science and Technology, Universiti Malaysia Sabah, 88400, Kota Kinabalu, Sabah, Malaysia

[4]Sonophotochemistry Research Group, Faculty of Science and Technology, Universiti Malaysia Sabah, Kota Kinabalu 88400, Sabah, Malaysia

[5]HEJ Research Institute of Chemistry, International Center for Chemical and Biological, Sciences, University of Karachi, Karachi, 75270, Pakistan

[6]Department of Pharmacy, The University of Lahore, Lahore, Punjab, Pakistan.

*** Correspondence:**
Faisal Shahzad:
faisalshahzad.chemist@gmail.com
Muhammad Ikram Nabeel;
ch.ikramnabeel802@gmail.com

Received: 13 April 2026
Revised: 16 June 2026
Accepted: 22 June 2026
Published online:
23 June 2026

Doi :
10.51200/bsj.v47i1.7565

Keywords:
Green approach, CuO NPS, *Cenetella asiatica* Extract, Direct dye Treatment, Methylene Blue, Methylene Orange, Photocatalytic degradation.

ABSTRACT. This research (preliminary study) aims to explore the green synthesis approach and characterizations of copper oxide nanoparticles, which employed to photocatalytic degradation of methylene blue (MB) and methyl orange (MO) from aqueous solution. *Centella asiatica* fresh leaves were used in the green synthesis of copper oxide (CuO) nanoparticles (NPs) because it contains multifunctional properties like reducing agent as well as stabilizing agent. The copper oxide nanoparticles were synthesized at ambient temperature and pressure, furthermore it was characterized by scanning electron microscopy (SEM) and thermal gravimetric analysis (TGA), which confirmed their thermal stability, and surface morphology. The photocatalytic efficacy of CuO was investigated against MB and MO. Experiments were conducted at different temperature with aid of Pyrex reactor where degradation efficiency was examined through UV-Visible spectrophotometer. Analysis confirmed that, it was Pseudo first order degradation whereas activation energy calculated were 26.19 kJ/mol and 32.6 kJ/mol for M.O and M.B respectively. Factors such as initial concentrations of dye, temperature, does of catalyst, and rate of agitations were optimized to determine how these factors contribute the efficiency of degradation. The CuO nanoparticles showed excellent property as heterogeneous catalyst and retained same behavior after multiple use. The results showed that the green synthesis of CuO NPs is promising due to inexpensive, greener process to decontaminate the dye-wastewater. This study explores the sustainable approach to synthesized green catalyst and addressing the removal of dye to mitigate the environmental remediation.

Graphical Abstract

INTRODUCTION

In recent few decades, metal oxide nanoparticles (NPs) emerged as one of promising type of transition metal oxide due to their superior electrical and thermal conductivities, unique physicochemical characteristics, and wide range of applications in the fields of catalysis, sensing, energy storage, and environmental remediation (Huang, He et al. 2019, Ali, Nabeel et al. 2023). Among various metal oxides, CuO is one of the most famous examples of a p-type semiconductor with a narrow bandgap (1.2 eV) that has been used in both redox and photocatalytic reactions as a highly efficient heterogeneous catalyst. Factors such crystal planes, surface oxygen lattice, and morphology influencing catalytic performance of nanostructures and for technological applications require controlled synthesis of size- and shape-specific nanostructures (Aazam, Mohamed et al. 2013). One of the most significant applications of CuO NPs lies in the photocatalytic degradation of organic pollutants, especially synthetic dyes such as methyl orange (MO) and methylene blue (MB) (Acedo-Mendoza, Infantes-Molina et al. 2020). Photocatalysis is initiated when visible or UV light promotes electrons from the valence band to the conduction band of a semiconductor catalyst, producing electron-hole pairs (Affandi, Joseph et al. , Qasim, Manzoor et al. 2026). These charge carriers further interact with molecular oxygen and water to generate highly reactive species such as hydroxyl radicals (•OH) and superoxide radicals ($O_2^{\bullet-}$) (Arif, Rasheed et al. 2026, Joseph, Anisuzzaman et al. 2026). These radical species have the potential to mineralizing organic pollutants into non-toxic end products such as H_2O and CO_2. Advanced oxidation processes (AOPs) is emerged as superior alternatives to conventional methods due to their ability to degrade a wide range of toxic compounds into less harmful or completely benign substances (Abboud, Saffaj et al. 2014, Nabeel, Hussain et al. 2025).

The industrial effluents are usually toxic and may contain heavy metals (Hg, Cr, Cd, As, Pb), nitro aromatics, phenolic derivatives, pesticides and dyes, all of them are very dangerous to the human body and aquatic environment (Qasim, Manzoor et al. 2025, Arif, Rasheed et al. 2026). Heterogeneous photocatalysis, which involves the application of semiconductor oxides (CuO, V_2O_5, TiO_2, SiO_2, CdS, Fe_2O_3, SnO_2, ZnS, BiOI, ZnO etc) has been shown to be a cost effective and efficient way of dealing with these pollutants using redox transformations (Nabeel, Hussain et al. 2025). Among these, the most appealing is CuO owing to its low cost, narrow bandgap and high catalytic properties, thus making it very effective in degradation of dyes using visible light. Sol-gel processing, hydrothermal treatment, gas-phase deposition, microwave-assisted synthesis, thermal decomposition, and combustion techniques are the conventional techniques of synthesizing CuO nanoparticles.

Although such physicochemical methods offer controlled nanostructures, they are usually expensive, energy intensive, and the processes involved come with dangerous byproducts, which restrict their application in the environment at large scale. Therefore, the green synthesis approaches are also developed with much momentum and gaining attention (Bhattacharjee, Ahmaruzzaman et al. 2018). Green synthesis strategies employ biological resources like algae, microorganisms, and especially plant extracts that also serve as reducing, stabilizing and capping agents (Arif, Rasheed et al. 2025). Plant-mediated synthesis is also useful in that it does not use toxic chemicals, less energy is required, and the nanoparticles obtained are uniform and more stable than most chemical methods (Khan, Moeid et al. 2025). The phytochemicals in the plant tissues contain alkaloids, terpenoids, flavonoids and polyphenols, which have the ability to regulating the growth of the particles as well as reducing the metal salts to nanoparticles(Dauthal, Mukhopadhyay et al. 2016, Vaseghi, Nematollahzadeh et al. 2018). In traditional medicine, *Centella asiatica (L.),* also called as Gotu kola, has been extensively known to possess medicinal properties and to contain high levels of bioactive compounds. In this experiment, the *C. asiatica* leaves extract was utilized which act as a reducing agent as well as a stabilizing agent in the synthesis of the green synthesis of CuO NPs in the presence of copper acetate [$Cu(CH_3COO)_2$] as a precursor(Chandrika, Kumara et al. 2015, Sabaragamuwa, Perera et al. 2018).

The current project (preliminary study) is planned to be engineered with the goal of designing cost-effective, an effective, and sustainable photocatalyst to decompose harmful organic dyes in water. In this respect, the synthesis of copper oxide nanoparticles was conducted in green and a simple procedure by utilizing the *Centella asiatica* leaf extract that acted both as a stabilizing and reducing agent. The objective was to develop a synthesis pathway that utilizes readily available and cheap precursor materials at standard temperature and pressure, and thus, reduces the cost of reaction. The current paper is able not only to demonstrate the benefits of plant-mediated synthesis to obtain well-defined and stable copper oxide nanoparticles, but also explore their practical use in the decolorization and degradation of model organic dyes including methylene blue (MB) and methyl orange (MO) (Chaudhary, Rohilla et al. 2019). This paper also discusses the operational parameters required to achieve the maximum degradation efficiency of MB and MO. Through environmentally sustainable processes, these types of research help to develop green technologies aimed at pollution removal. Such an approach promotes sustainable environmental management of several United Nations Sustainable Development Goals (SDGs), particularly SDG 6, SDG 9, and SDG 12 (Ibrahim, Joseph et al. 2025).

MATERIALS AND METHODS

The study was carried out at the Chemistry Department, Government College University, Faisalabad and detailed characterization was done at the National Textile University, Faisalabad. The objectives of the research were synthesis and characterization as well as photocatalytic degradation of methyl orange (MO) and methylene blue (MB) dyes by employing copper oxide (CuO) nanoparticles in aqueous solutions. The analytical grade chemicals that were used in all experiments were not further purified to ensure the reproducibility and reliability of the findings. Copper acetate [$Cu(CH_3COO)_2$] was used as the precursor material and distilled water was used in all the solutions. MB and MO dyes were purchased from Merck, Germany. Centella asiatica fresh leaves collected from Jaranwala were used to because it contains the bioactive phytochemicals such as, flavonoid, terpenoids, and polyphenols, which has natural ability to reduce and stabilize nanoparticle formation. The extract of the plant involved washing and then shade drying of the leaves over a period of thirty days. The leaves were then dried and refluxed in 700 mL of the distilled water for two hours; the leaves then separated and the filtrate then collected through standard filter paper. This aqueous extract was used directly in the green synthesis of CuO nanoparticles, which offered a new green and sustainable gateway alternative to the traditional chemical procedures.

Synthesis of CuO NPs

For the synthesis of CuO NPs, 4.57 g of copper acetate was dissolved in 250 mL distilled water to make a 0.1 M solution. Followed by this, 30 mL was transferred from this solution into another beaker, and 50 mL of the plant extract was added drop by drop into the solution under constant magnetic stirring over a period of 2 hours at ambient temperature. The dropwise addition of plant extract ensured controlled nucleation and uniform growth of nanoparticles. The attained mixture was centrifuged and then the obtained precipitate was washed with ethanol and distilled water to eliminate unreacted precursors. The dried nanoparticles were first dried at 80°C and further calcined at 600°C to produce crystalline CuO nanoparticles with intended photocatalytic characteristics. **Figure 1** shown the representation green synthesis of CuO nanoparticles using the *Centella asiatica* (used as source of stabilizing and reducing agents). These bioactive compounds in the leaves allow the process of green synthesis, which involves the reduction of copper ions to nanoparticles and capping them to avoid from agglomeration.

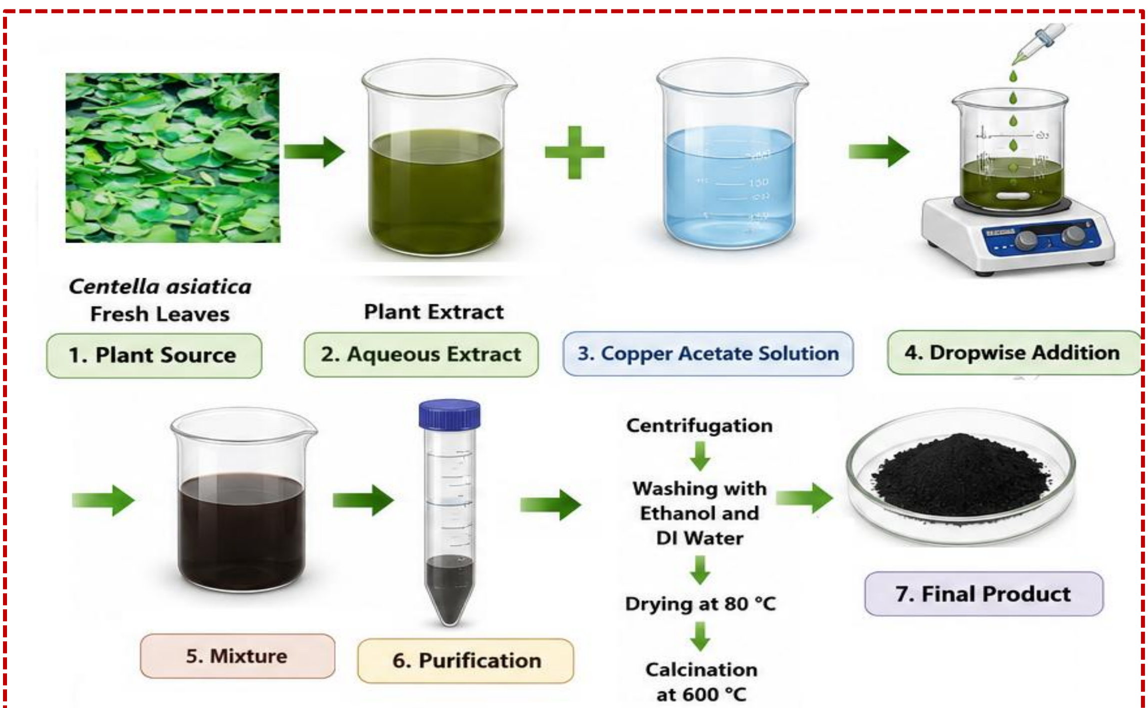

Figure 1. Schematic representation of the green synthesis of CuO nanoparticles using the Centella *asiatica* fresh leaves acted as source of a stabilizing and reducing.

Photocatalytic test:

To evaluate the catalyst efficiency, experiments of photocatalytic degradation were conducted in test beakers of 500mL using aqueous solution of MO and MB dyes at different concentration and stirring the mixture at 500rpm at different temperatures. First, 0.5 mL of the dye solution was sampled after 30 minutes of dark stirring to assess adsorption desorption equilibrium. This was followed by the addition of 0.05 g of CuO nanoparticles and stirring in the dark for more 30 minutes and then UV light was irradiated on the mixture (Ilyas and Saeed 2011, Jia, Mei et al. 2012). The photocatalytic degradation efficacy of MO and MB was check over time by taking aliquots of the reaction mixture, diluting it with 10 mL of distilled water, and measuring it by UV-Visible spectrophotometry using 1 cm path-length cuvettes. Calibration curves were used to find dye concentrations, and percentages of dye degradation were determined by using formula (Moon, Salunke et al. 2018, Mosleh, Rahimi et al. 2018).

$$\textbf{Degradation \%} = C_o - C_t / C_n \quad \times 100 \qquad (1)$$

In this equation, C_o represents the initial concentration, while C_t the concentration at time t. This systematic sampling made it possible to assess kinetic analysis and reaction rate evaluation, which would be reproducible and reliable data to determine photocatalytic efficiency.

RESULTS AND DISCUSSION

Characterization of CuO Nanoparticles

SEM Analysis: The size distribution and morphology of the prepared fabricated copper oxide (CuO) Nanoparticles was analyzed using the scanning electron microscopy (SEM). The homogeneous and almost spherical particles with low aggregation/ uneven surface is observed (indicating the successful deposition and formation of nanoparticulate clusters), are seen in the SEM images as shown in **Figure 2a-d.** The particle size was determined to be in the sub-micron (with increasing magnification,), which justified the synthesis of nanoparticles. This morphology (the development of granular and more defined nanostructures becomes evident) reflects that the green synthesis procedure with *Centella asiatica* extract is useful in regulating the particle growth and agglomeration (revealing the progressive nucleation and growth of CuO nanoparticles). This surfaces exhibit a high surface area, which is essential in the catalytic applications, increasing the number of active sites that can be used in the reactions of degrading dyes. Well-dispersed particles make sure that the maximum contact of the dye molecules takes place in the process of photocatalysis, which may boost up the degradation efficiency (Nezamzadeh-Ejhieh and Karimi-Shamsabadi 2013, Nasrollahzadeh, Sajjadi et al. 2018). The SEM analysis demonstrated that the green synthesis approach produces specific form of shape and size (nano-clusters with rough textures which is essential to the photocatalytic activity (Chowdhury, Khan et al. 2020, Aroob, Carabineiro et al. 2023)) of the CuO nanoparticles and these structural properties reflect to high catalytic performance that are consistent adsorption sites and the development of effective electron-holes generation at the UV light.

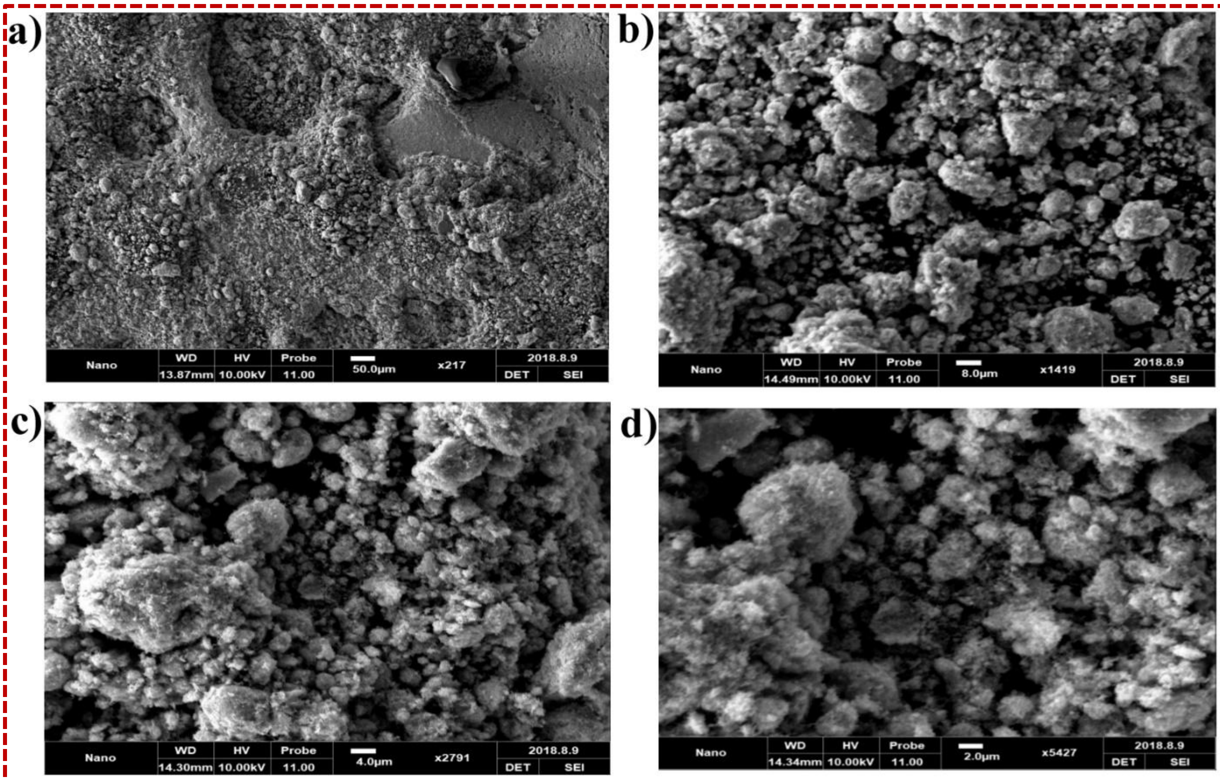

Figure 2: (a-d) SEM photographic images of fabricated copper oxide (CuO) Nanoparticles

Thermogravimetric Analysis (TGA): TGA was carried out to examine the thermal stability of fabricated copper oxide (CuO) Nanoparticles as illustrated in **Figure 3 (**exhibited a gradual weight loss of approximately 2.9% from 30 to 500°C**).** Analysis suggests that there was an initial weight loss to below 150°C, was attributed to the removal of adsorbed moisture. While the subsequent loss between 150 and 400°C was attributed to the decomposition of phytochemical residues (from the *Centella asiatica* plant extract). Above this 500°C temperature, the catalyst demonstrated remarkable stability (the mass remained nearly constant), indicating the formation of thermally stable CuO nanoparticles with minimal residual organic content and this implies its use in high temperature applications. The low weight loss at high temperatures implies that the structural integrity of the nanoparticles is not degrade during catalytic functions (Kana, Kaviyarasu et al. 2019, Saeed, Muneer et al. 2019). One important parameter of the heterogeneous catalysts is that the material is thermally stable so that it can sustain repeated heating cycles without structural deformation. TGA findings show that the nanoparticles of CuO synthesized through green procedures are thermally stable, and their excellent thermal stability at elevated temperatures helpful in photodegradation reaction in diverse environmental conditions (Sajjad, Ullah et al. 2018).

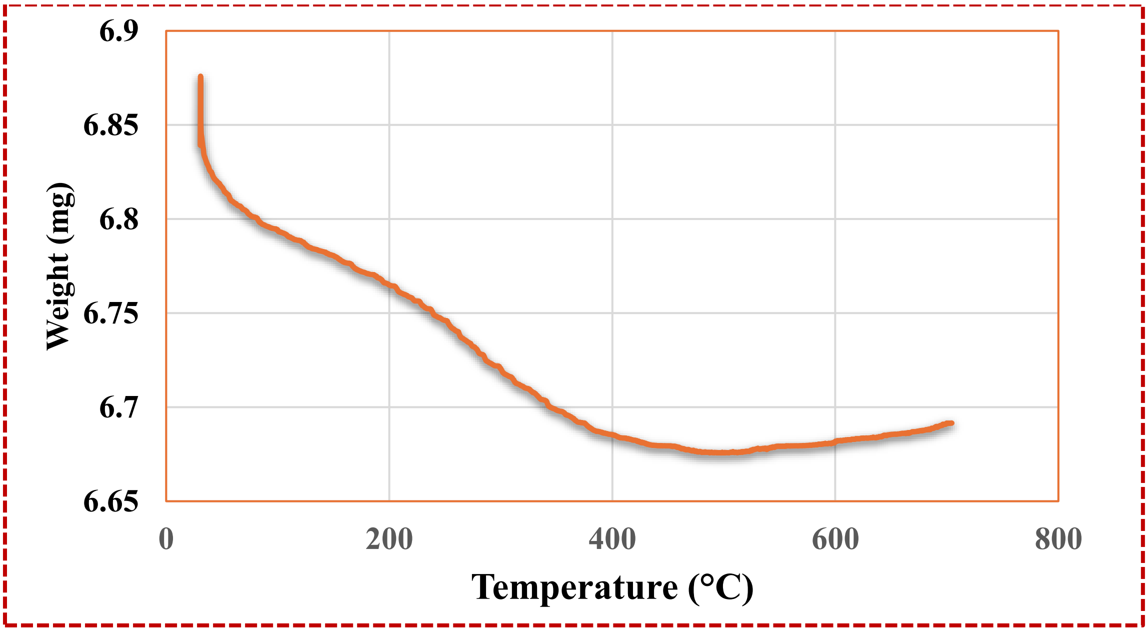

Figure 3. TGA analysis of fabricated copper oxide (CuO) Nanoparticles

Photocatalytic Degradation of Methylene Blue Dye

Analysis of Reaction Mixture: The photocatalytic experiments were conducted to determine the concentration of M.B by using UV-Vis spectroscopic analysis. Standard solutions of 10 -50 ppm were made and their absorbance spectra were measured as illustrated in **Figure 4 (a).** The peak at 505 nm represents the λmax. Therefore, all absorbance measurements during the photocatalytic degradation experiments were carried out at this 505 nm wavelength. **Figure 4 (b).** demonstrated the calibration curve that was prepared by drawing a graph between the concentration and the absorbance, which could be used to find the dye concentration at different times during the degradation process (Salavati-Niasari and Davar 2009). The calibration curve showed excellent linearity (R_2 > 0.998), which confirmed the accuracy of the absorbance measurements to quantify the sample. This method ensures that a reduction in absorbance in the course of catalytic experiments can be attributed directly to the dye degradation as opposed to experimental artifact. Calibration is important in the determination of kinetic parameters and the effective assessment of the CuO nanoparticles as photocatalyst as shown in **Figure 4 (b).**

Impact of Catalyst Dose: The effect of the loading of catalysts on the degradation of M.B was investigated by taking different dose of catalysts CuO (0.05 g to 0.25 g) per 100 ml was shown in **Fig 4(c).** The dose of the catalyst peaked the degradation efficiency to a point of 0.2 g, after which it showed a slow decline. This is because the rate of degradation was higher at lower doses may suggests that there are more active sites available to form the reactive oxygen species (ROS) and dye oxidation. The drop on higher dose is probably because of light scattering causes less absorption and weak penetration of photons through the suspension, which has an increased turbidity (Sankar, Manikandan et al. 2014). These findings suggest that there is an optimum catalyst loading at which the photocatalytic efficiency is highest. The measured trend is consistent with the heterogeneous photocatalysis mechanism, in which surface adsorption of dye molecules and electron-hole pairs formation are the key factors. High dose of catalyst may be counterproductive to light penetration thereby reducing the efficient photocatalytic reaction.

Analysis of the effect of agitation speed on degradation: The influence of stirring speed on M.B degradation was monitored in the range of 100-600 rpm at 40 °C using 0.2 g of CuO as demonstrated in **Fig 4(d).** The rate of degradation plateaued and starting at 400 rpm, then declined. The optimal stirring rate provides good dispersion of the catalyst and mass transfer of the dye molecules to the active sites of catalyst effectively. Extreme agitation can cause less time of contact between the dye molecules and the catalyst surface leading to lower degradation efficiency. The agitation studies emphasize the significance of optimization of reaction conditions in the process of efficient photocatalysis. Effective stirring is also used to increase catalyst-dye contact as well as to prevent the agglomeration of nanoparticles leading to sedimentation of a reaction. These findings are essential in the scaling up of the process to be applicable in real wastewater treatment.

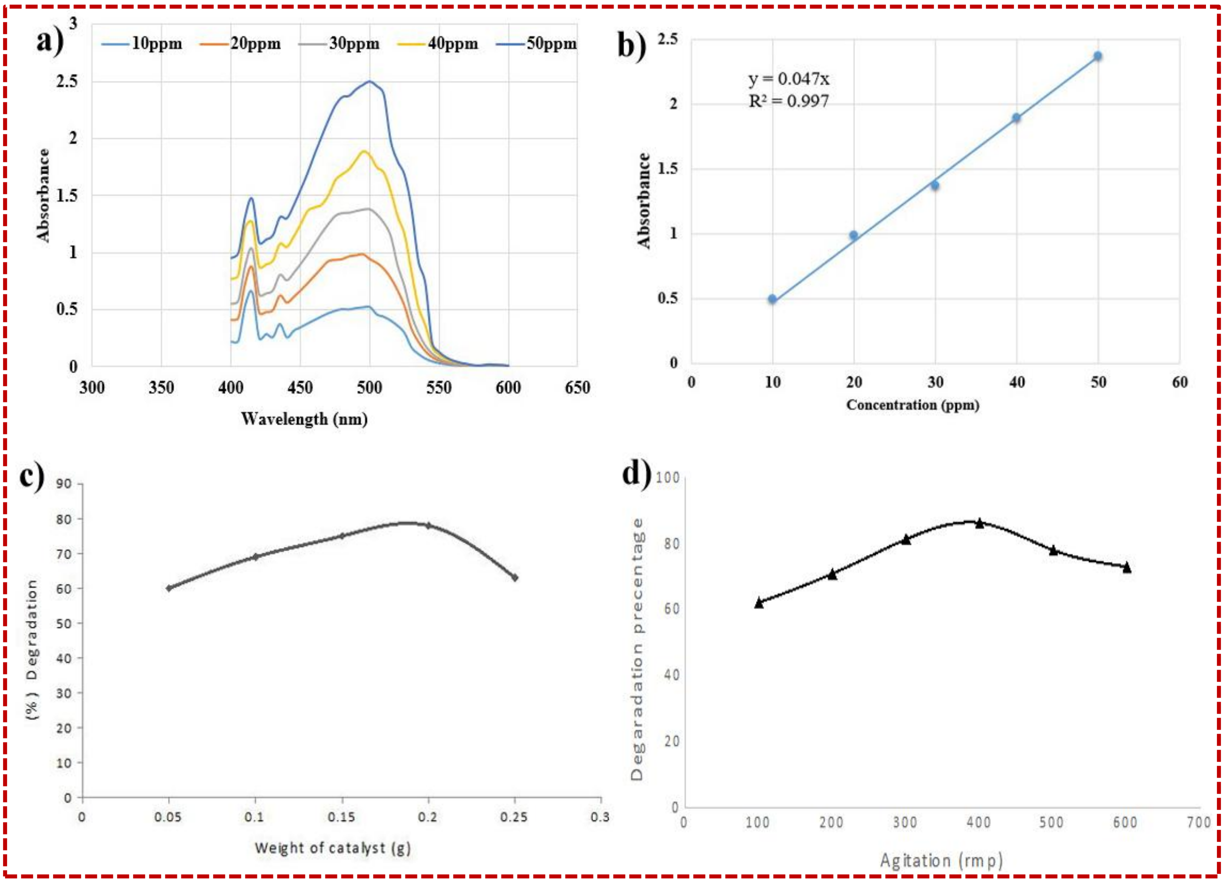

Figure 4. a) Visible range spectra of different standard solutions of M.B recorded b) Calibration curve for dye Methylene Blue (M.B) showing excellent linearity c) Impact of catalyst dose on the dye's degradation efficacy d) Impact of agitation on percentage degradation of M.B dye.

Impact of Temperature on degradation: Impact of temperature on photocatalytic degradation were tested at 30°C, 40°C and 50°C as illustrated in **Figure 5(a).** The rate of degradation was increased by rise in temperature with the degradation efficiencies reached near about 72%, 86%, and 90% at 30, 40, and 50°C, respectively .Raised in temperatures increase the number of molecular collisions therefore, the rate of production of ROS and the kinetics of dye degradation (Sathishkumar, Sweena et al. 2011, Senobari, Nezamzadeh-Ejhieh et al. 2018). Temperature-dependent behavior confirmed that the photocatalytic process is endothermic means energy need to proceed the reaction (which promote the photocatalytic oxidation of MB molecules). High temperatures not only increase the rate at which dye molecules diffuse to active sites as well as increase the mobility of charge carriers in the catalyst, thus increasing the overall reaction rate. These studies give an insight into thermal stability and the efficiency of CuO nanoparticles to perform photocatalytic reactions.

Impact of Dye Concentration: The effect of higher concentration of Methylene Blue (M.B) on degradation efficiency was investigated by the use of 100, 200, and 300 ppm solutions as illustrated in **Figure 5(b).** The analysis indicates that higher dye concentration loading leads to decrease the percentage degradation. On the catalyst surface, the active sites become saturated at higher concentrations resultantly, photon absorption is decreased, which limits the generation of ROS. In the case of 100 ppm solution, 87% degradation was observed, while only lower degradation efficiencies of about 67% and 62% were obtained for 200 and 300 ppm (Song, Zhou et al. 2008). This is a concentration dependent effect, which highlights that photocatalytic activity is highly sensitive to initial dye loading. These lower concentrations enable the photons to easily penetrate and interact more with the catalyst active sites to a greater extent resulting in higher degradation. These insights are essential in designing treatment plans of wastewater that have different loads of pollutants.

Kinetic Studies of Methylene Blue Degradation: The photocatalytic degradation efficiency of M.B was also examined (Kinetic analysis at different temperatures) by using the pseudo-first-order kinetic model. The data of time-dependent concentration at various temperatures (30, 40, 50°C) were plotted as per this equation as shown in **Figure 5(c).** The resulting linear plots ensured that the reaction is pseudo-first order in nature. The linear relationship between $\ln(C_0/C_t)$ and irradiation time confirms the applicability of the Langmuir–Hinshelwood model. The consistency in the following of pseudo-first-order behavior is confirmed by the linear correlation ($R^2 > 0.995$), which means that the degradation rate is directly proportional to the dye concentration. This kinetic study gives an understanding of the catalytic mechanism in terms of the rate-limiting step, which is the interaction of the dye molecules and the photogenerated reactive oxygen species at the catalyst surface. It is supported by the data, determined the temperature-dependent rate constants presented in **Table 1** and they are a quantitative indicator of the efficiency of the catalyst under different thermal conditions. **Figure 5(c)** and **Table 1** has been used to calculate rate constants (k) and shows that there is an evident increase in rate constant with temperature. At 30 °C, $k = 0.0221\ min^{-1}$; at 40 °C, $k = 0.0298\ min^{-1}$; and at 50 °C, $k = 0.0421\ min^{-1}$. This tendency suggests that the increased rate of reaction owing to high-speed collisions between molecules and to the high speed of charge carrier's movement in high temperatures (indicating that higher temperatures facilitate the degradation process and enhance the reaction kinetics). The temperature dependence observed is expected to be aligned with a behavior of the Arrhenius-type, which proves the fact that the photocatalytic degradation of M.B is thermally activated. This kind of kinetic data is essential to the optimization of operation parameters and process scaling when it comes to industrial wastewater treatment.

Table 1. Rate constant determined by applying to the degradation data at various temperatures.

Temperature (°C)	k= min^{-1}
30	0.0221
40	0.0298
50	0.0421

Concentration-Dependent Kinetics: M.B was also applied to the pseudo-first-order model (Kinetic analysis at different dye concentrations). **Figure 5(d)** exhibits the M.B degradation in various initial concentration (100, 200, 300 ppm) at constant temperature (30°C) in the presence of 0.1 g CuO. The model was once again confirmed by linear fits. Rate constants has opposite relationship with the dye concentration: 0.1145 min^{-1} (100 ppm), 0.0678 min^{-1} (200 ppm), and 0.0521 min^{-1} (300 ppm), with corresponding R^2 values of 0.8758, 0.9002, and 0.8052. which are summarized in **Figure 5(d)** and **Table 2.** The highest rate constant was observed for the 100 ppm solution, (faster degradation kinetics at lower dye concentrations) and suggests that excessive dye molecules hinder light absorption and occupy active catalytic sites. This behavior attributes to saturation of catalyst active sites and decreased photon penetration at high dye loads leading to a lower number of effective ROS interactions occurring per dye molecule. This demonstrates the need to optimize the pollutant concentrations in order to maximize the photocatalytic effectiveness.

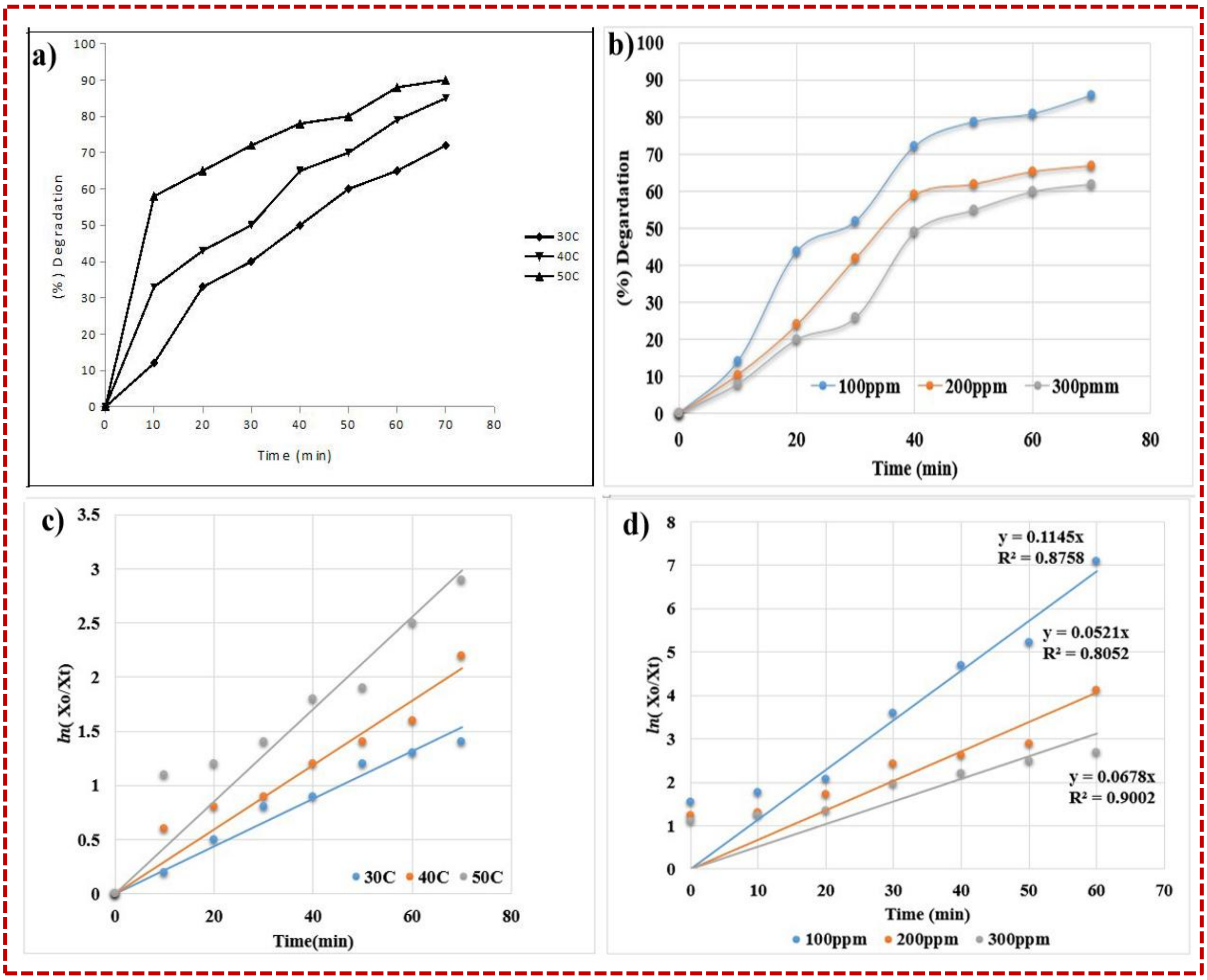

Figure 5. a) The influence of temperature on degradation efficiency of Methylene blue *Centella asiatica*-mediated CuO nanoparticles b) Impact of concentration of M.B dye on percentage degradation efficiency c) Pseudo-first-order kinetic plots at at varying temperatures. d) Pseudo-first-order kinetic plots at various dyes concentration.

Table 2: Degradation data at different concentrations was used to find the rate constant for MB.

Concentration (ppm)	K= min^{-1}
100	0.1145
200	0.0678
300	0.0521

Arrhenius Analysis:

To find the activation energy of the degradation process against temperature, the rate constants of degradation process were used to plot an Arrhenius plot as shown in **Figure 6.** Arrhenius plot of ln(k) versus 1/T, which exhibited excellent linearity with a correlation coefficient (R^2) of 0.996. The value of the activation energy, which was calculated, is 26.19 kJ mol^{-1}, implying that the energy barrier to the electron-hole generation and oxidation of the dyes with the support of ROS is moderate. The value of such is comparable to the typical semiconductor photocatalysts, and reflects the efficacy of CuO nanoparticles in UV/visible light. The kinetic and thermodynamic data both support the statement that the photocatalytic degradation of M.B by CuO nanoparticles is a first-order, temperature sensitive process, which is driven by surface interactions and generation of reactive species. Moreover, the strong linear correlation confirms that the degradation process follows Arrhenius behavior within the investigated temperature range (temperature plays a significant role in enhancing the photocatalytic performance and accelerating the degradation kinetics of methylene blue). These insights play a critical role in the systematic development and optimization of photocatalytic systems of water treatment.

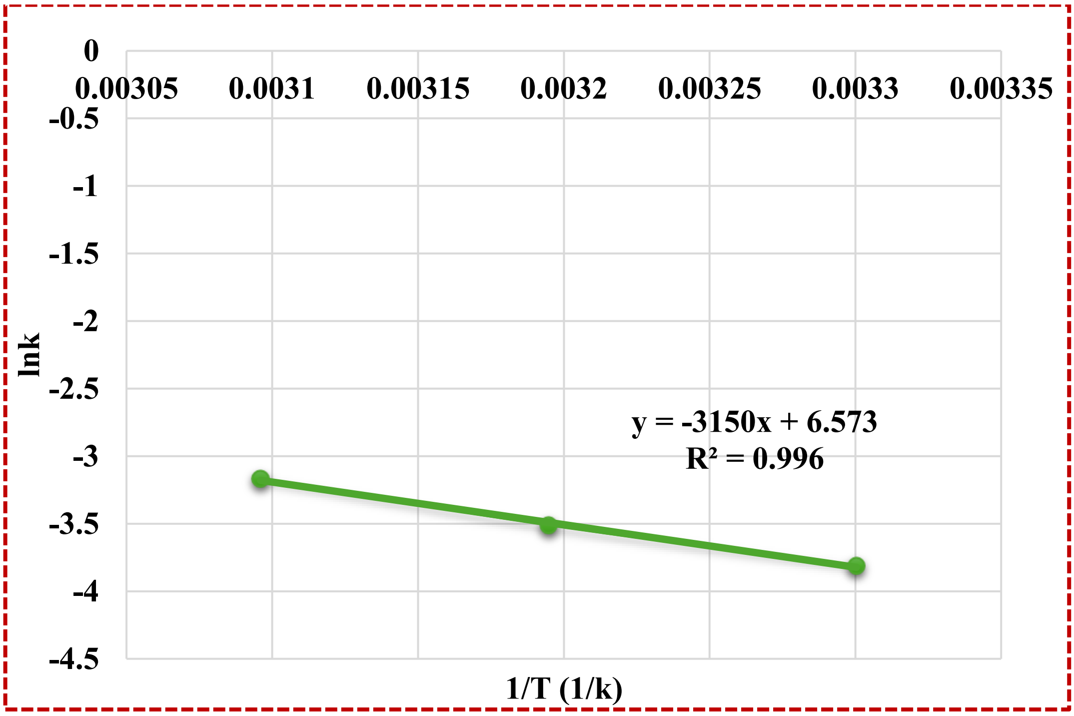

Figure 6: Arrhenius plot of ln(k) versus 1/T for the photocatalytic degradation (using *Centella asiatica*-mediated CuO nanoparticles).

Photocatalytic Degradation of Methyl Orange (M.O)

Analysis of Reaction Mixture: Firstly, the standard solutions of M.O solutions at different concentrations (10–50 ppm), and their absorbance spectra were monitored through spectrophotometer within 400–600 nm range which is known as visible range. The λ max at 475 nm was observed (indicating adherence to the Beer–Lambert law) for M.O as demonstrated in **Figure 7(a).** The resulting calibration curve, shown in **Figure 7(b)**, displayed the excellent linearity and concentration over the investigated range with the regression equation **$y = 0.0463x$** and a correlation coefficient **$R^2 = 0.9982$**, enable accurate determination of M.O concentrations at various reaction times. The UV- Vis spectra validate distinct absorption properties of M.O, justifying the analysis technique of degradation and kinetic investigations. The dye concentration at different times was determined using calibration data, which is necessary to measure photocatalytic performance.

Impact of Catalyst Dose: The impact of catalyst loading (0.05-0.25 g) on M.O having 200 ppm concentration at 40 °C were investigated which were demonstrated in **Figure 7(c)**. The optimum catalyst dose was found to be at maximum degradation when 0.2g of catalyst was used (The degradation efficiency initially decreased with increasing catalyst dose up to 0.15 g, then increased to a maximum at 0.20 g suggesting an optimum catalyst loading for effective photocatalytic degradation). An increase in catalyst amount led to reduction in performance through turbidity and saturation of active sites, which restricted penetration of photons and generation of ROS. The loading of catalysts is the key parameter to the maximum photocatalytic efficiency by employing minimum amount of catalyst use. The results confirmed that the moderate amount of catalyst give the balance of adsorption surface and light permeation.

Analysis of the Impact of agitation speed on degradation: **Figure 7(d)**, shows agitation rates effect (100-500 rpm) and degradation percentage increased from about 53% at 100 rpm to a maximum of approximately 60% at 200 rpm, followed by a gradual decrease at higher agitation speeds. Optimal degradation about 60% was observed when the agitation speed was 200 rpm. High speeds reduced degradation because there was no adequate contact time between catalyst surfaces and dye molecules. This finding justified that the mixing should be appropriate in order to achieve homogeneous dispersion of nanoparticles and the optimal contact to dye molecules. When agitation is excessive, efficiency is reducing, and therefore special attention should be paid to the regulation of the reaction parameters.

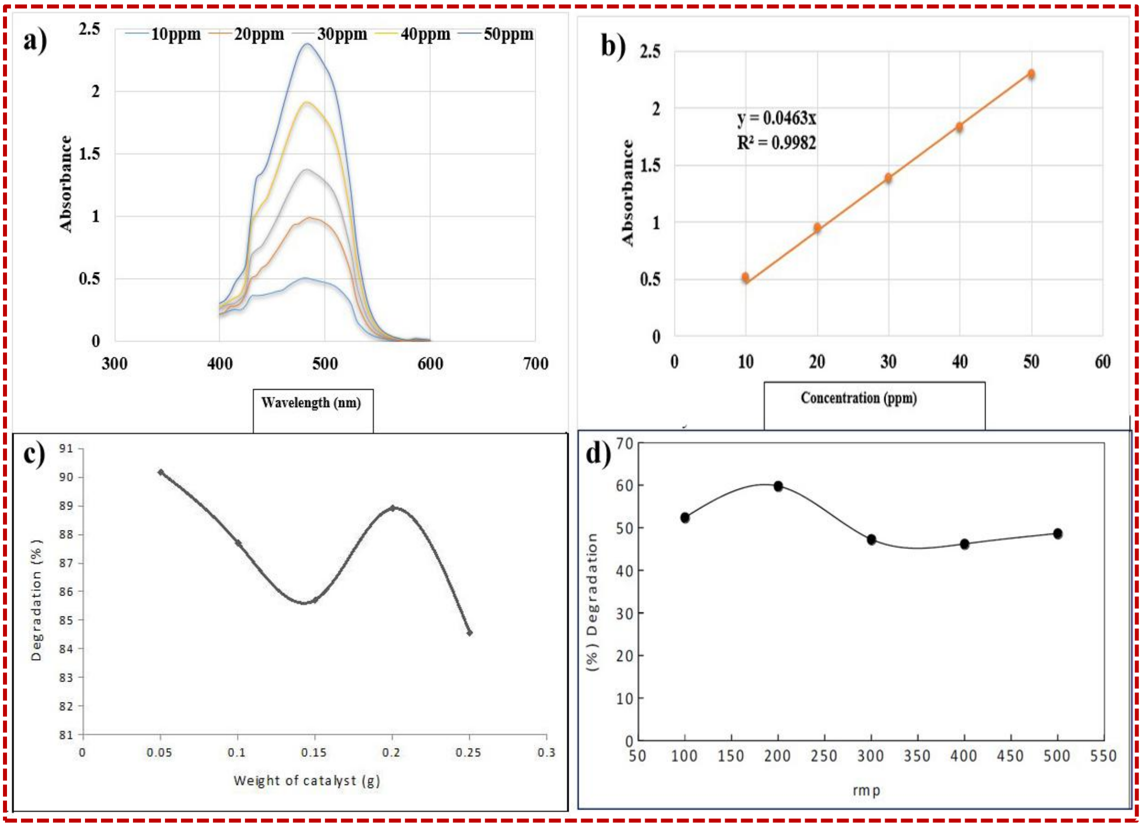

Figure 7: a) Visible region spectra of standard solutions of M.O with different concentrations, b) Calibration curve for dye Methylene Orange (M.O) showing excellent linearity c) Impact of catalyst dose on M.O degradation efficiency d) Impact of agitation on percentage degradation of M.B dye.

Temperature-Dependent Degradation: Photocatalytic studies were studied at 30, 40 and 50°C. The results in **Fig 8 (a)** showed that the rate of degradation was increased with increasing the temperature. At 30 °C, it was observed that approximately 10% of the dye was degraded after 10 minutes and it reached to 69 % after 70 minutes. At 40 °C, degradation efficiency reached 35% at 10 minutes and 83% at 60 minutes, whereas at 50 °C, it went up to 61% at 10 minutes and 92% at 60 minutes. This tendency demonstrated that the raise in temperature promotes the number of collisions between molecules and the generation of reactive oxygen species (ROS), which increases photocatalytic performance. Data of the temperature dependence can be also used to find the rate constants using pseudo-first-order kinetics, as shown in **Table 3.** The first-order behavior is confirmed by linear fits. The rate constants were observed to increase with temperature and attained 0.0185, 0.0279 and 0.0411 min $^{-1}$ at 30, 40 and 50°C respectively, **Kinetic Studies of *Methylene Orange Degradation:*** The data of time-profiles were processed in terms of pseudo-first-order kinetics in **Figure 8(b)** and **Figure 8(c)** represent the kinetic plots at different temperatures and concentrations, respectively. **Table 4** represent the Rate constant determining for the degradation at different concentrations was used to find the rate constant for MO.

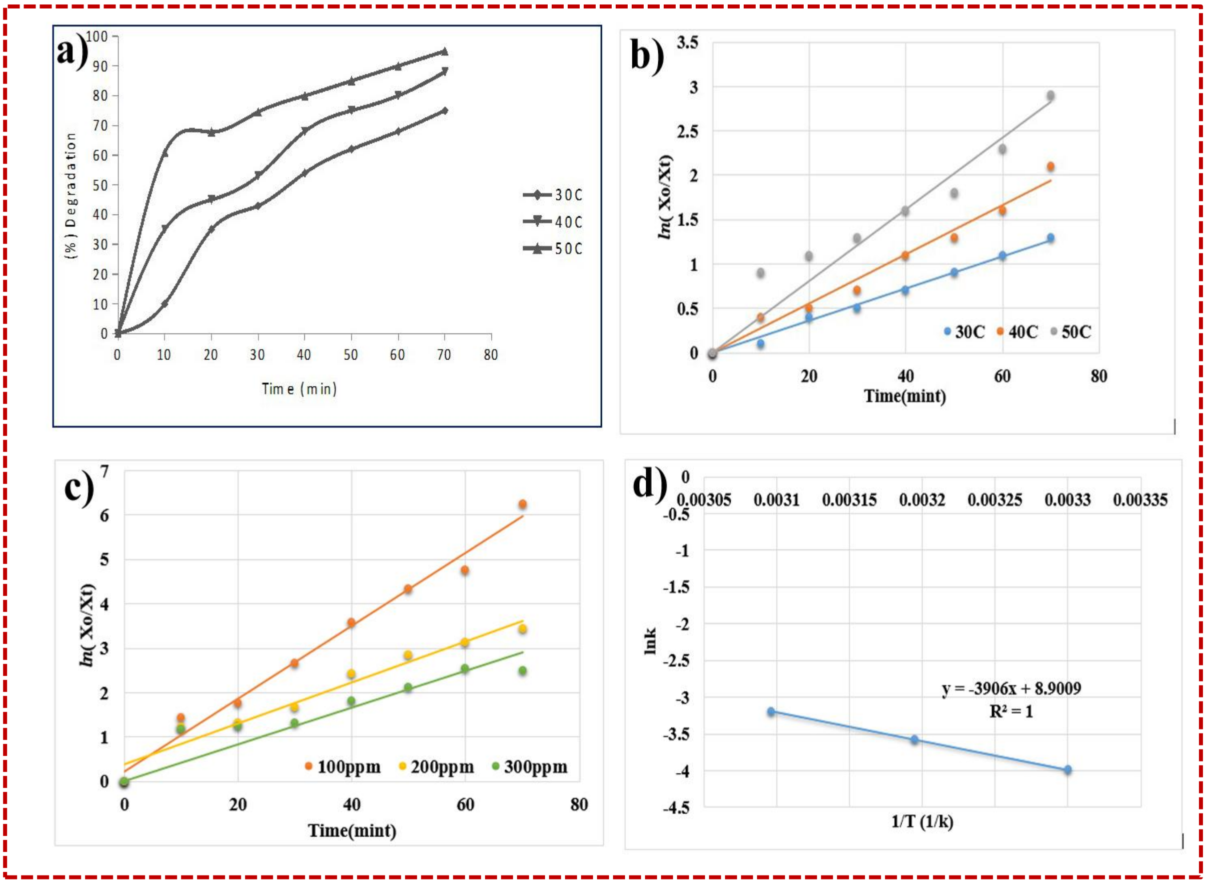

Figure 8: a) The influence of temperature on degradation efficiency of Methylene Orange by employing CuO catalyst, b) Fitted kinetic model to experimental data at various temperatures, **c)** Arrhenius Plot, d) Fitted kinetic model to experimental data at various concentration of M.O dye

Table 3. Rate constant calculated by applying on degradation data at various temperatures.

Temperature (°C)	$K = min^{-1}$
30	0.0185
40	0.0279
50	0.0411

Arrhenius analysis resulted in an activation energy of 32.6 kJ mol^{-1}, which demonstrated that moderate energy needs to generate ROS and transfer electrons and holes, which is good indicator of catalysis as shown in **Figure 8(d)**. The saturation of active sites and lower penetration of photons at higher loads of dyes leading to reduction of rate constant with increased in concentration of dye. The kinetic parameters highlighted that both dye concentration and temperature should be optimized to obtain efficient photocatalytic treatment.

Table 4. Rate constant determining for the degradation at different concentrations was used to find the rate constant for MO.

Concentration(ppm)	Rate Constant (per min)
100	0.0823
200	0.0464
300	0.0416

Limitations and Future Perspectives

This study provides an initial assessment (preliminary investigation) of green-synthesized CuO nanoparticles and their application in the photocatalytic degradation of MB and MO dyes. The primary objective of this preliminary investigation to demonstrate the feasibility of green synthesis of CuO nanoparticles as an effective photocatalyst for dyes removal. A limitation of the current work is the absence of several advanced characterization techniques (TEM, EDX, BET, UV–DRS) that could offer deeper insight into the physicochemical properties of the nanoparticles were not performed in the current study due to instrumental and resource limitations. Therefore, the findings presented herein should be regarded as preliminary findings that establish a foundation for further investigation. Future research will involve comprehensive characterization (TEM, EDX, BET, UV–DRS) together with detailed studies of recyclability, and degradation mechanisms (TOC/COD analysis, intermediate identification, LC-MS/GC-MS analysis). Additional experiments will also be conducted to assess optimization, to further validate and expand this study different operational conditions will be investigated.

CONCLUSION

This study was able to provide a green, sustainable pathway towards the synthesis of copper oxide nanoparticles by employing *Centella asiatica* leaf extract, which acted as a natural stabilizing and reducing agent. SEM and TGA were used to characterize the synthesized nanoparticles that proved their crystalline structure, thermal stability, and heterogeneous nature. CuO nanoparticles were comprehensively analyzed on based of catalytic activity to two common dyes, which are methylene blue (MB) and methylene orange (MO) in aqueous medium. The process of degradation was pseudo-first-order was confirmed and activation energies (Ea) of CuO catalyst for degradation of M.B and M.O was calculated as 26.19 kJ/mol and 32.6 kJ/mol. The effect of experimental conditions including dye concentration, temperature, catalyst dosage, and agitation rate were examined extensively and it was found that optimized experimental conditions are critical to obtain the maximum degradation efficiency. In general, this study validates the prospects of green-synthesized CuO nanoparticles as economical, greener, and reusable photocatalysts in the treatment of wastewater

REFERENCES

Aazam, E., R. J. J. o. A. Mohamed and Compounds (2013). "Environmental remediation of Direct Blue dye solutions by photocatalytic oxidation with cuprous oxide." **577**: 550-555.

Abboud, Y., T. Saffaj, A. Chagraoui, A. El Bouari, K. Brouzi, O. Tanane and B. J. A. n. Ihssane (2014). "Biosynthesis, characterization and antimicrobial activity of copper oxide nanoparticles (CONPs) produced using brown alga extract (Bifurcaria bifurcata)." **4**(5): 571-576.

Acedo-Mendoza, A., A. Infantes-Molina, D. Vargas-Hernández, C. Chávez-Sánchez, E. Rodríguez-Castellón and J. Tánori-Córdova (2020). "Photodegradation of methylene blue and methyl orange with CuO supported on ZnO photocatalysts: The effect of copper loading and reaction temperature." Materials science in semiconductor processing **119**: 105257.

Affandi, N. A., C. G. Joseph, M. I. Nabeel, M. H. Abd Majid and K. Ghazali "Photolytic and Photocatalytic Degradation of Detergent and Surfactant Solutions by Various Light Sources."

Ali, M. A., M. I. Nabeel, T. Hussain, A. Awwad, E. Ismail, A. Mustafa and N. Hassan (2023). "Radiation-induced degradation of PVA-26 by UV radiation in the presence of ZnO nanocatalyst." J Biomed Res Environ Sci **4**: 2276.

Arif, S., S. Rasheed, N. Ahmad, M. I. Nabeel, W. Ahmad, T. Alomayri, D. Hussain and S. G. Musharraf (2026). "Carbon-based materials for photocatalytic degradation of pharmaceuticals and drugs." Journal of Water Process Engineering **81**: 109274.

Arif, S., S. Rasheed, M. I. Nabeel, W. Ahmad, M. T. Riaz, S. G. Musharraf and D. Hussain (2025). "Enhanced Photocatalytic Activity of Sulfur–Nitrogen Co-Doped TiO2 Nanoparticles Synthesized using Dactylorhiza hatagirea Root Extract." ChemistrySelect **10**(34): e01568.

Aroob, S., S. A. Carabineiro, M. B. Taj, I. Bibi, A. Raheel, T. Javed, R. Yahya, W. Alelwani, F. Verpoort and K. J. C. Kamwilaisak (2023). "Green synthesis and photocatalytic dye degradation activity of CuO nanoparticles." **13**(3): 502.

Bhattacharjee, A., M. J. J. o. P. Ahmaruzzaman and P. A. Chemistry (2018). "Microwave assisted facile and green route for synthesis of CuO nanoleaves and their efficacy as a catalyst for reduction and degradation of hazardous organic compounds." **353**: 215-228.

Chandrika, U. G., P. A. P. J. A. i. f. Kumara and n. research (2015). "Gotu Kola (Centella asiatica): nutritional properties and plausible health benefits." **76**: 125-157.

Chaudhary, S., D. Rohilla, A. Umar, N. Kaur and A. J. C. I. Shanavas (2019). "Synthesis and characterizations of luminescent copper oxide nanoparticles: toxicological profiling and sensing applications." **45**(12): 15025-15035.

Chowdhury, R., A. Khan and M. H. J. R. a. Rashid (2020). "Green synthesis of CuO nanoparticles using Lantana camara flower extract and their potential catalytic activity towards the aza-Michael reaction." **10**(24): 14374-14385.

Dauthal, P., M. J. I. Mukhopadhyay and E. C. Research (2016). "Noble metal nanoparticles: plant-mediated synthesis, mechanistic aspects of synthesis, and applications." **55**(36): 9557-9577.

Huang, A., Y. He, Y. Zhou, Y. Zhou, Y. Yang, J. Zhang, L. Luo, Q. Mao, D. Hou and J. Yang (2019). "A review of recent applications of porous metals and metal oxide in energy storage, sensing and catalysis." Journal of Materials Science **54**(2): 949-973.

Ibrahim, M. N. A., C. G. Joseph, N. Surugau, M. I. Nabeel and S. S. Ismail (2025). "From waste to water cleanup: Preliminary study on sargassum-derived activated carbon (AC) for pollutant adsorption." Mater. Emerg. Technol. Sustain **1**: 2550015.

Ilyas, M. and M. J. I. J. o. C. R. E. Saeed (2011). "Synthesis and characterization of manganese oxide and investigation of its catalytic activities for oxidation of benzyl alcohol in liquid phase." **9**(1).

Jia, B., Y. Mei, L. Cheng, J. Zhou, L. J. A. a. m. Zhang and interfaces (2012). "Preparation of copper nanoparticles coated cellulose films with antibacterial properties through one-step reduction." **4**(6): 2897-2902.

Joseph, C. G., S. Anisuzzaman, N. N. D. Masjidin, D. Masjidin, A. S. Moktar, W. Nasir, M. I. Nabeel, N. Tahir and A. Bade (2026). "Removal of residual antibiotics from aquaculture wastewater using ozonation and sonochemical treatment processes: a comprehensive review." Chemical Papers: 1-34.

Kana, N., K. Kaviyarasu, T. Khamliche, C. M. Magdalane and M. J. J. o. E. C. E. Maaza (2019). "Stability and thermal conductivity of CuO nanowire for catalytic applications." **7**(4): 103255.

Khan, N. M., A. Moeid, S. Kiran, T. Gulzar, I. Pervez, R. Shahid, M. I. Nabeel and A. Ali (2025). "Prunus armeniaca assisted green synthesis of Fe2O3/NiO nanohybrids using unripened fruit extract for remediation of acid orange 7 dye: A sustainable environmental cleaner approach." Waste and Biomass Valorization **16**(2): 581-599.

Moon, S. A., B. K. Salunke, P. Saha, A. R. Deshmukh and B. S. J. K. J. o. C. E. Kim (2018). "Comparison of dye degradation potential of biosynthesized copper oxide, manganese dioxide, and silver nanoparticles using Kalopanax pictus plant extract." **35**(3): 702-708.

Mosleh, S., M. R. Rahimi, M. Ghaedi, K. Dashtian and S. J. U. s. Hajati (2018). "Sonochemical-assisted synthesis of CuO/Cu2O/Cu nanoparticles as efficient photocatalyst for simultaneous degradation of pollutant dyes in rotating packed bed reactor: LED illumination and central composite design optimization." **40**: 601-610.

Nabeel, M. I., D. Hussain, N. Ahmad, A. Saeed, K. Ali, H.-M. Xiao and S. G. Musharraf (2025). "Facile Synthesis of Robust 2D Z-scheme Ultrathin Sulfur Doped g-C3N4-Tungsten Oxide Composite by High Pressure Vacuum Filtration for 5-FU Detoxification." Surfaces and Interfaces: 108278.

Nabeel, M. I., D. Hussain, N. Ahmad, H.-M. Xiao, W. Ahmad and S. G. Musharraf (2025). "Facile one-pot synthesis of metal and non-metal doped g-C3N4 photocatalyst for rapid acetaminophen remediation." Carbon **243**: 120472.

Nasrollahzadeh, M., M. Sajjadi and S. M. J. C. J. o. C. Sajadi (2018). "Biosynthesis of copper nanoparticles supported on manganese dioxide nanoparticles using Centella asiatica L. leaf extract for the efficient catalytic reduction of organic dyes and nitroarenes." **39**(1): 109-117.

Nezamzadeh-Ejhieh, A. and M. J. C. e. j. Karimi-Shamsabadi (2013). "Decolorization of a binary azo dyes mixture using CuO incorporated nanozeolite-X as a heterogeneous catalyst and solar irradiation." **228**: 631-641.

Qasim, M., S. Manzoor, M. I. Nabeel, S. Hussain, R. Waqas, C. G. Joseph and J. Suazo-Hernández (2025). "Harnessing High-Valent Metals for Catalytic Oxidation: Next-Gen Strategies in Water Remediation and Circular Chemistry." Catalysts **15**(12): 1168.

Qasim, M., S. Manzoor, M. I. Nabeel, Q. Ullah, Y. Z. Sair, T. Khomphet, C. G. Joseph, A. Raza, J. Suazo-Hernández and T. Gulzar (2026). "Waste-derived nanocomposites as dual-function materials for water and energy sustainability." Frontiers in Sustainability **7**: 1777462.

Sabaragamuwa, R., C. O. Perera, B. J. T. i. F. S. Fedrizzi and Technology (2018). "Centella asiatica (Gotu kola) as a neuroprotectant and its potential role in healthy ageing." **79**: 88-97.

Saeed, M., M. Muneer, M. K. K. Khosa, N. Akram, S. Khalid, M. Adeel, A. Nisar, S. J. G. P. Sherazi and Synthesis (2019). "Azadirachta indica leaves extract assisted green synthesis of Ag-TiO2 for degradation of Methylene blue and Rhodamine B dyes in aqueous medium." **8**(1): 659-666.

Sajjad, M., I. Ullah, M. Khan, J. Khan, M. Y. Khan and M. T. J. R. i. P. Qureshi (2018). "Structural and optical properties of pure and copper doped zinc oxide nanoparticles." **9**: 1301-1309.

Salavati-Niasari, M. and F. J. M. L. Davar (2009). "Synthesis of copper and copper (I) oxide nanoparticles by thermal decomposition of a new precursor." **63**(3-4): 441-443.

Sankar, R., P. Manikandan, V. Malarvizhi, T. Fathima, K. S. Shivashangari, V. J. S. A. P. A. M. Ravikumar and B. Spectroscopy (2014). "Green synthesis of colloidal copper oxide nanoparticles using Carica papaya and its application in photocatalytic dye degradation." **121**: 746-750.

Sathishkumar, P., R. Sweena, J. J. Wu and S. J. C. E. J. Anandan (2011). "Synthesis of CuO-ZnO nanophotocatalyst for visible light assisted degradation of a textile dye in aqueous solution." **171**(1): 136-140.

Senobari, S., A. J. S. A. P. A. M. Nezamzadeh-Ejhieh and B. Spectroscopy (2018). "A comprehensive study on the photocatalytic activity of coupled copper oxide-cadmium sulfide nanoparticles." **196**: 334-343.

Song, K., J. Zhou, J. Bao and Y. J. J. o. t. A. C. S. Feng (2008). "Photocatalytic activity of (copper, nitrogen)-codoped titanium dioxide nanoparticles." **91**(4): 1369-1371.

Vaseghi, Z., A. Nematollahzadeh and O. J. R. i. C. E. Tavakoli (2018). "Green methods for the synthesis of metal nanoparticles using biogenic reducing agents: a review." **34**(4): 529-559.

RESEARCH ARTICLE

BORNEO SCIENCE
THE JOURNAL OF SCIENCE & TECHNOLOGY

Journal homepage: https://jurcon.ums.edu.my/ojums/index.php/borneo-science

EFFECTS OF CO-ADSORBENT SILANE COUPLING AGENT STRUCTURE ON THE PERFORMANCE OF N719-BASED DYE-SENSITIZED SOLAR CELLS: AN EXPERIMENTAL AND DENSITY FUNCTIONAL THEORY INVESTIGATION

Cornellia Geoffrey[1], Edmund Engilip[1], Ivan Giggs Bin Florence[1], Jefany Joel Dapanis[1], Rachel Fran Mansa[2], Jedol Dayou[1], Alvie Lo Sin Voi*[1]

[1] Faculty of Science and Technology, Universiti Malaysia Sabah, Jalan UMS, 88400 Kota Kinabalu, Sabah, Malaysia.

[2] Faculty of Engineering and Technology, Universiti Malaysia Sabah, Jalan UMS, 88400 Kota Kinabalu, Sabah, Malaysia.

*** Correspondence:**
lv@ums.edu.my

Received: 08 May2026
Revised: 26 June 2026
Accepted: 26 June 2026
Published online:
26 June 2026

Doi :
10.51200/bsj.v47i1.6582

Keywords:
Dye-sensitized Solar Cells; Silane Coupling Agent; Co-adsorbant; Density Functional Theory.

ABSTRACT. *Charge recombination at the TiO_2–electrolyte interface remains a major limitation to the efficiency of dye-sensitized solar cells (DSSCs). In this work, the effect of silane coupling agents as co-adsorbents in N719-based DSSCs was systematically investigated. Eight silane derivatives with different molecular structures—TESF, 14BTEP, 13BTEP, B3TEP, TEVS, MPTS, IZPES, and BTEBP—were incorporated alongside the N719 dye, and their photovoltaic performance was compared with a control device prepared without silane. The control cell exhibited a power conversion efficiency (η) of 7.1%. Among the silane-modified devices, BTEBP achieved the highest efficiency of 7.4%, followed closely by IZPES at 7.3%, while 13BTEP and B3TEP showed reduced efficiencies of 6.7% and 6.8%. Density functional theory (DFT) calculations at the B3LYP/6-31G(d) level on isolated silane molecules provided molecular thickness (h) and chain size (d) descriptors. A clear structure–performance relationship emerged: an optimal silane thickness of ~8–13 Å combined with bulky chain geometry was most effective for TiO_2 surface passivation. These results demonstrate that silane co-adsorbent influence on DSSC performance strongly depends on molecular structure.*

INTRODUCTION

Dye-sensitized solar cells (DSSCs) are widely regarded as a promising third-generation photovoltaic technology due to their low fabrication cost, simple processing techniques, and good performance under diffuse and low-light conditions (O'Regan & Grätzel, 1991; Hagfeldt et al., 2010; Abdulsalami et al., 2026). Despite these advantages, the power conversion efficiency of DSSCs remains limited by interfacial charge recombination, particularly at the TiO_2/dye/electrolyte interface. Recombination between electrons injected into the TiO_2 conduction band and oxidized species in the electrolyte significantly reduces photocurrent density and overall device efficiency (Rühle et al., 2005; Zaine et al., 2020; Ashrafuzzaman et al., 2025; Arkan et al., 2024).

To address recombination losses, various interfacial engineering strategies have been developed, including surface passivation layers, surface doping, and the use of co-adsorbents. Co-adsorbents are typically small molecules introduced alongside sensitizing dyes to passivate uncovered TiO_2 surface sites, suppress electron–electrolyte recombination, and regulate dye adsorption to reduce aggregation (Liang et al., 2010; Gierszewski et al., 2019; Ren et al., 2022; Dissanayake et al., 2025). Surface passivation using organic, inorganic, or hybrid layers has been shown to prolong electron lifetime and improve open-circuit voltage in DSSCs (Park et al., 2012b; Tehare et al., 2018; Suresh et al., 2018).

Among the various surface modifiers investigated, silane-based compounds have attracted increasing attention due to their strong affinity for metal oxide surfaces and their ability to form stable Si–O–Ti bonds. Silane coupling agents can chemically anchor to TiO_2 surfaces, effectively passivating surface defects and limiting direct electrolyte contact with the semiconductor (Sewvandi et al., 2014). Experimental studies have demonstrated that silane modification of TiO_2 photoanodes can suppress charge recombination, enhance dye coverage, and improve device efficiency (Sewvandi et al., 2014; Neo & Ouyang, 2011; Dissanayake et al., 2025).

In addition to passivation, silane modification has been shown to influence dye organization and interfacial properties. Molecular-scale surface treatments can affect dye packing density, aggregation behavior, and interfacial energetics, thereby impacting short-circuit current density and fill factor (Rühle et al., 2005; Sobuś et al., 2018). The effectiveness of silanes as back-electron blocking agents has been suggested to depend on their molecular structure (Jung et al., 2014; Sewvandi et al., 2014). Despite these promising findings, systematic experimental investigations comparing different silane molecular structures on DSSC performance remain limited.

In this study, a series of silane derivatives are employed as co-adsorbents together with N719 dye on TiO_2 photoanodes. DFT calculations on isolated silane molecules provide molecular thickness (h) and chain size (d) descriptors correlated with experimental performance to establish structure–performance relationships (Arkan et al., 2024). This work aims to provide experimental and computational insight into the role of silane chemistry in interfacial passivation and to establish molecular design principles for optimizing dye-sensitized solar cells.

MATERIALS AND METHODS

Materials

All chemicals were used as received. Anatase-phase TiO_2 paste (Ti-Nanoxide T/SP, ~20 nm), N719 dye (Ruthenizer 535-bisTBA), iodide/triiodide electrolyte (Iodolyte Z-50), platinum paste (Platisol T/SP), and fluorine-doped tin oxide (FTO) glass substrates (TCO Glass-22, 8–12 $\Omega\ cm^{-1}$, 2.2 mm thickness) were purchased from Solaronix. Surlyn® thermoplastic film (25 µm, Meltonix 1170-25) was used as spacer and sealant. Silane coupling agents were obtained from Sigma-Aldrich (≥97%): 3-(triethoxysilyl)furan (TESF), 1,4-bis(triethoxysilyl)benzene (14BTEP), 1,3-bis(triethoxysilyl)benzene (13BTEP), bis[3-(triethoxysilyl)propyl]tetrasulfide (B3TEP), triethoxyvinylsilane (TEVS), 3-mercaptopropyltriethoxysilane (MPTS), triethoxy-3-(2-imidazolin-1-yl)propylsilane (IZPES), and 4,4′-bis(triethoxysilyl)-1,1′-biphenyl (BTEBP).

DSSCs Fabrication

TiO_2 photoanodes were prepared on pre-cleaned FTO glass substrates. The nanoporous TiO_2 electrode consisted of two layers deposited by the doctor-blade method: a first layer of 20 nm TiO_2 nanoparticles (Ti-Nanoxide T/SP) and a second scattering layer of 100 nm particles (Ti-Nanoxide R/SP). After printing the first layer, the glass was sintered at 300 °C for 10 min; following deposition of the second layer, the electrode was sintered at 500 °C for 1 h to crystallize both layers (total film thickness ~10–12 µm).

N719 dye was dissolved in anhydrous acetonitrile to a concentration of 0.3 mM and magnetically stirred for 30 min at room temperature. Dye solutions were stored in aluminium foil-covered containers below 25 °C. Eight silane stock solutions were prepared by dissolving each silane in anhydrous acetonitrile at mass concentrations equivalent to the N719 dye solution. Equal volumes of dye and silane solutions were combined (1:1, v:v) under gentle stirring, maintaining a constant N719 concentration of 0.3 mM and a dye-to-silane weight ratio of 1:1.

Interfacial modification was carried out via a sequential protocol (Sewvandi et al., 2014). TiO_2 electrodes were first immersed in the control dye solution for 24 h at room temperature, then transferred to the respective dye–silane pre-mixed solutions for 2 h. Electrodes were rinsed with anhydrous ethanol and dried under inert atmosphere. Platinum counter electrodes were prepared by doctor-blading Pt paste onto FTO glass and sintering at 400 °C for 15 min. Cells were assembled using a 25 µm Surlyn spacer. The electrolyte (0.5 M 1-methyl-3-propylimidazolium iodide, 0.05 M I_2, 0.1 M TBP in acetonitrile) was introduced by vacuum backfilling. Assembled cells were stored in the dark for 12 h prior to measurement.

Photovoltaic Performance

Current–voltage (J–V) measurements were performed using a Class AAA solar simulator (YOHA YHCT-AAA) under simulated AM 1.5G illumination (100 mW cm^{-2}). Spectral mismatch was below 2% and spatial uniformity exceeded 95% over a 2 × 2 cm^2 active area. Voltage scans were conducted from −0.1 to 0.8 V with a step size of 0.01 V and a delay time of 50 ms at 25 ± 1 °C and 40 ± 5% relative humidity. Light intensity was calibrated using an NREL-certified silicon reference cell. Each device was measured three times; reported parameters (Jsc, Voc, FF, η) represent averaged values with standard deviations below 3%.

Computational Method

DFT calculations were performed using Gaussian 09 at the B3LYP/6-31G(d) level (Arkan et al., 2024) on isolated silane molecules in the vacuo. Each silane molecule was subjected to full geometry optimization without symmetry constraints. Two molecular descriptors were computed from the optimized ground-state geometries: (i) molecular thickness h (Å), the maximum vertical extent of the silane molecule, representing the effective length of the passivation layer when adsorbed on TiO_2; and (ii) chain size d (Å), the maximum lateral spatial extent of the silane molecule, representing molecular bulkiness and the surface area potentially shielded by each silane upon TiO_2 adsorption.

RESULTS AND DISCUSSION

DSSCs performance

The prepared selected DSSCs is shown in Figure 1. The J–V characteristics are shown in Figure 3 and the corresponding parameters are compiled in Table 1. The control DSSC (N719, without silane) showed Jsc = 17.3 mA cm^{-2}, Voc = 0.73 V, FF = 0.56, and η = 7.1%.

Three devices demonstrated enhanced PCE compared to the control. BTEBP achieved the highest PCE of 7.4% (~4.2% relative improvement), attributable to increased FF (0.58) and slightly higher Jsc (17.4 mA cm^{-2}). IZPES exhibited the second-highest PCE of 7.3%, driven by the highest Jsc among all silanes (17.7 mA cm^{-2}) and improved FF of 0.58. The 14BTEP sample also reached 7.3% efficiency, matching IZPES but with higher Voc (0.73 V). These results are consistent with recent findings that appropriately chosen co-adsorbents can substantially enhance DSSC performance (Dissanayake et al., 2025).

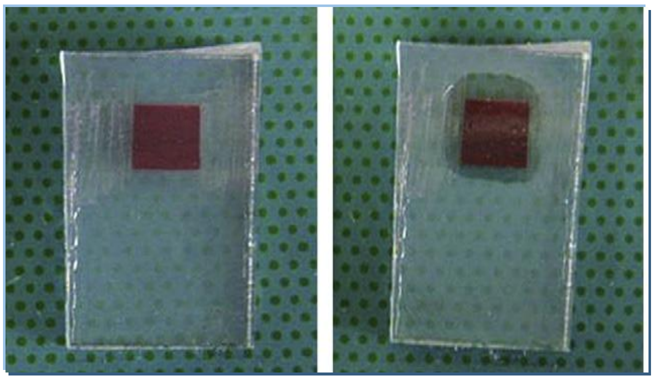

Figure 1. Fabricated silane co-adsorbs N719 base DSSCs using doctor blade method.

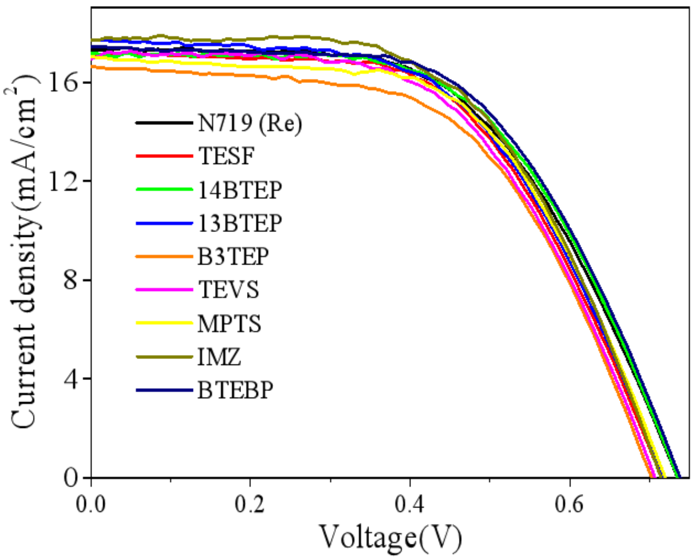

Figure 2. J–V characteristics of N719 base DSSCs incorporating different silane co-adsorbents under AM 1.5G illumination (100 mW cm^{-2}).

Table 1. Photovoltaic parameters of N719 base DSSCs with different silane co-adsorbents under AM 1.5G illumination (100 mW cm^{-2}).

Sample	Jsc (mA cm^{-2})	Voc (V)	FF	η (%)
N719 (control)	17.3	0.73	0.56	7.1
TESF	17.2	0.72	0.57	7.0
14BTEP	17.2	0.73	0.56	7.3
13BTEP	16.6	0.71	0.57	6.7
B3TEP	17.0	0.71	0.56	6.8
TEVS	17.4	0.73	0.58	7.4
MPTS	17.3	0.73	0.57	7.1
IZPES	17.7	0.71	0.58	7.3
BTEBP	17.4	0.74	0.58	7.4

Devices with 13BTEP and B3TEP underperformed relative to the reference cells. The 13BTEP-modified device recorded the lowest PCE of 6.7% (Jsc = 16.6 mA cm^{-2}, Voc = 0.71 V). B3TEP yielded 6.8% (Jsc = 17.0 mA cm^{-2}, Voc = 0.71 V). The remaining silanes (TESF, MPTS) produced parameters comparable to the control.

A notable observation is that all silane-treated cells matched or exceeded the control FF of 0.56, with BTEBP, IZPES, and TEVS reaching 0.58. This universal FF enhancement is attributed to Si–O–Si siloxane network formation within the TiO_2 film during co-adsorption, which bridges adjacent nanoparticles and improves inter-particle electronic connectivity (Park et al., 2012a). The variation in Voc was relatively modest across all devices (0.70–0.74 V), consistent with a physical surface blocking mechanism.

Silane Structure–Performance Correlations

Optimized geometry of the silane molecule obtained from the DFT calculations at the B3LYP/6-31G(d) are shown in Figure provided molecular thickness (h) and chain size (d) descriptors. Table 2 summarizes the computed h and d values alongside experimental efficiency.

Table 2. DFT-computed molecular thickness (h) and chain size (d) at the B3LYP/6-31G(d) level on isolated silane molecules, with corresponding experimental efficiency.

Silane	h (Å)	d (Å)	η (%)
N719 (control)	—	—	7.1
TESF	5.0	3.6	7.0
14BTEP	9.3	8.8	7.3
13BTEP	9.3	8.8	6.7
B3TEP	18.0	9.2	6.8
TEVS	3.3	1.4	7.4
MPTS	5.8	1.0	7.1
IZPES	7.8	3.4	7.3
BTEBP	13.3	9.3	7.4

The combined experimental and DFT dataset reveals clear structure–performance relationships governing silane effectiveness as co-adsorbents in N719-based DSSCs. Molecular thickness (h) — optimal range ~8–13 Å. Silanes with thickness in this range — 14BTEP (h = 9.3 Å, η = 7.3%), IZPES (h = 7.8 Å, η = 7.3%), and BTEBP (h = 13.3 Å, η = 7.4%) — all outperformed the control device. This thickness range corresponds approximately to the estimated thickness of the N719 sensitizer layer (~12 Å), suggesting that effective passivation requires the silane to be of comparable height to the dye molecules. Silanes that are substantially shorter, such as TESF (h = 5.0 Å) and TEVS (h = 3.3 Å), provide insufficient physical blocking. Conversely, B3TEP (h = 18.0 Å, η = 6.8%) may form a barrier so thick that it hinders I^- access for dye regeneration.

The shielding effect provided by the modifier is heavily influenced by its chain size. Bulkier geometries are inherently better suited to passivate the surface; accordingly, the highest-performing molecules, BTEBP (d = 9.3 Å) and 14BTEP (d = 8.8 Å), feature the largest overall chain sizes. The necessity of this steric bulk is further proven by MPTS; with the smallest chain size evaluated (d = 1.0 Å), it demonstrated a baseline performance on par with the control, reinforcing that nominal chain sizes lack the capacity for effective surface shielding (Dissanayake et al., 2025).

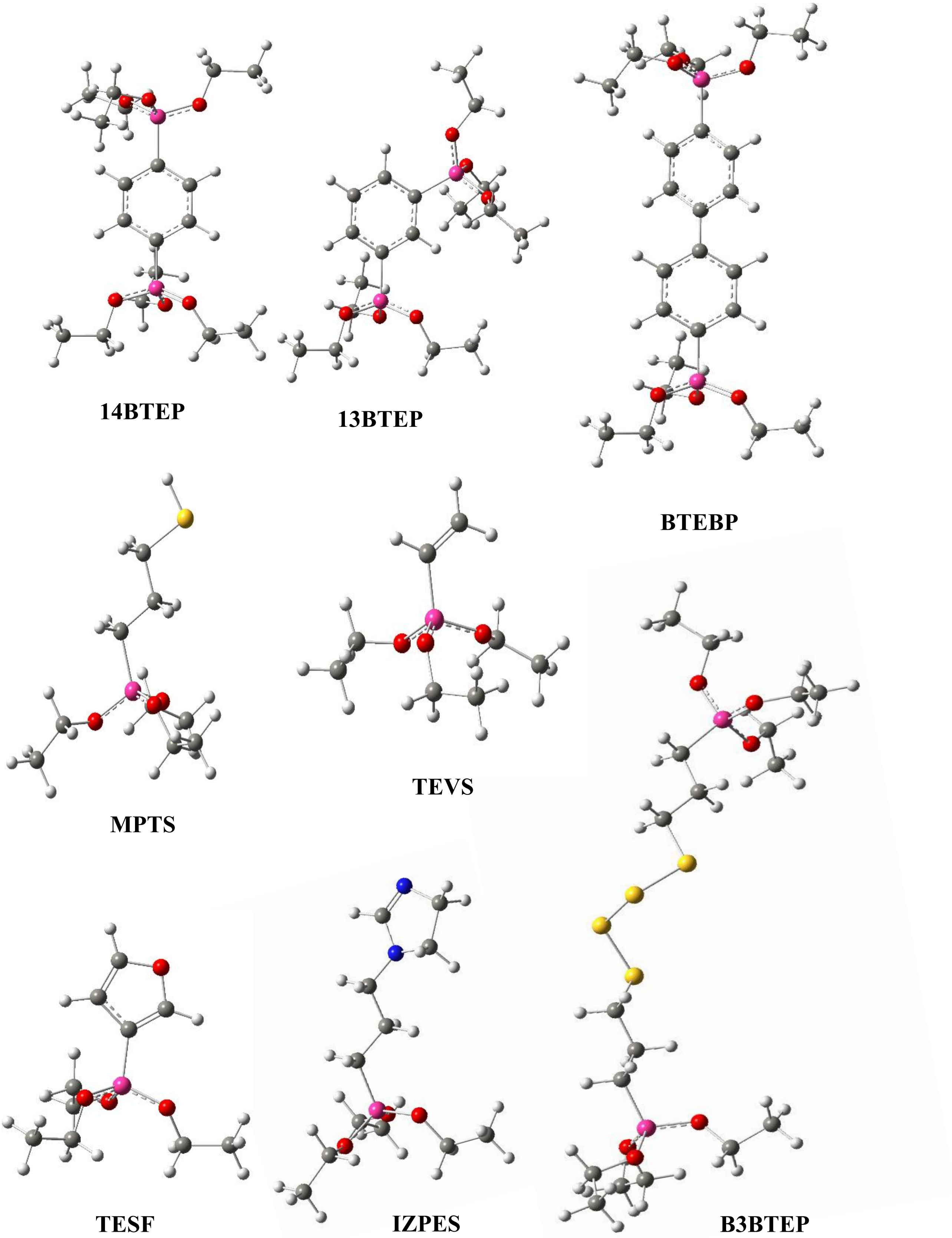

Figure 3. Optimize geometry of Silanes Molecule using B3LYP/6-31G(d) level of theory.

The case of TEVS (h = 3.3 Å, d = 1.4 Å) which is the smallest silane investigated yet achieves the highest efficiency (7.4%) alongside BTEBP. Under the sequential fabrication protocol, the compact TEVS molecules may preferentially adsorb into narrow interstitial spaces between pre-adsorbed dye molecules "interstitial filling" enabling targeted passivation of the most critically exposed TiO_2 sites. The high FF (0.58) supports efficient electron transport via siloxane networks (Park et al., 2012a).

CONCLUSION

The influence of silane co-adsorbents with different molecular structures on the photovoltaic performance of N719-based DSSCs was systematically investigated through combined experimental measurements and DFT calculations on isolated silane molecules. Among the eight silane derivatives tested, BTEBP and TEVS achieved the highest PCE of 7.4%, while IZPES and 14BTEP reached 7.3%, all exceeding the control device (7.1%). In contrast, 13BTEP (6.7%) and B3TEP (6.8%) reduced device performance.

DFT calculations on isolated silane molecules identified an optimal molecular thickness of approximately 8–13 Å corresponding to the N719 sensitizer layer thickness. Silanes that are too short provided insufficient blocking, while those excessively long hindered dye regeneration. Bulkier chain geometries enhanced surface shielding efficiency. All silane-treated devices exhibited fill factors equal to or higher than the control, attributed to improved inter-particle connectivity via Si–O–Si siloxane network formation. Molecular orientation governed by substitution pattern was shown to be as important as gross molecular dimensions.

These findings demonstrate that silane co-adsorbent performance strongly depends on molecular structure. The structure–performance relationships established herein provide design guidelines for rational selection and computational screening of silane co-adsorbents for DSSCs.

ACKNOWLEDGEMENT

The author would like to thank Malaysian Ministry of Higher Education for the financial support to the research through Fundamental Research Grant Scheme [FRG0593-1/2022].

REFERENCES

Abdulsalami, I. O., Omobhude, I. A., Abdulsalami, B. A., Younas, M., Semire, B., & Bello, I. A. (2026). Dye-sensitized solar cells: A systematic review of progress, challenges, and future perspectives. Discover Chemistry, 3, 87.

Arkan, F., Pakravesh, F., Barati Darband, F., Sabagh, S., & Izadyar, M. (2024). Recent progress toward high-performance dye-sensitized solar cells: A review. Journal of the Iranian Chemical Society, 21, 577–638.

Ashrafuzzaman, M., Ismail, M., Ali, A. K. M., Bhargava, S. K., Alam, M. K., & Anower, M. S. (2025). Impact of TiO_2 compact layer on the performance of dye-sensitized solar cells. Journal of Power Sources, 638, 236636.

Dissanayake, M. A. K. L., Sandunika, P. U., Senadeera, G. K. R., Kumari, J. M. K. W., Hettiarachchi, M. S. H., Subasinghe, J. L., Karunaratne, A. K., & Sandamali, W. I. (2025). Exploring linoleic acid as a novel co-adsorbent to enhance dye-sensitized solar cell efficiency through surface engineering of TiO_2 at the photoanode/electrolyte interface. Journal of Applied Electrochemistry, 55, 2947–2964.

Gierszewski, M., Falkowski, M., Sobuś, J., Stolarski, M., Popenda, L., Lijewski, S., Wicher, B., Burdzinski, G., Karolczak, J., Jurga, S., Graczyk, A., Marszalek, T., Zakeeruddin, S. M., Grätzel, M., & Ziolek, M. (2019). Porphyrin-based symmetrical and unsymmetrical donor–acceptor dyes for DSSCs: The role of anchoring groups on photovoltaic performance. ACS Applied Materials & Interfaces, 11(3), 240–252.

Hagfeldt, A., Boschloo, G., Sun, L., Kloo, L., & Pettersson, H. (2010). Dye-sensitized solar cells. Chemical Reviews, 110(11), 6595–6663.

Jung, Y. S., Yoo, Y., Park, J. H., & Kim, H. K. (2014). Silane coupling agents for improving the photovoltaic performance of dye-sensitized solar cells. Bulletin of the Korean Chemical Society, 35(2), 415–420.

Liang, M., Zhong, X., & Ge, Z. (2010). Effect of co-adsorbents on TiO_2 interface and photovoltaic performance of dye-sensitized solar cells. Journal of Physical Chemistry C, 114(24), 10993–10998.

Neo, C. Y., & Ouyang, J. (2011). Functionalized carbon nanotubes with covalently attached silane for dye-sensitized solar cells. Journal of Power Sources, 196(23), 10538–10542.

O'Regan, B., & Grätzel, M. (1991). A low-cost, high-efficiency solar cell based on dye-sensitized colloidal TiO_2 films. Nature, 353(6346), 737–740.

Park, J. T., Prosser, J. H., Ahn, D. J., Kim, J. H., & Lee, D. (2012a). Enhancing the performance of solid-state dye-sensitized solar cells using a silane-based interfacial layer with controlled pore morphology. Electrochimica Acta, 59, 32–38.

Park, J. T., Chi, W. S., Roh, D. K., Ahn, S. H., & Kim, J. H. (2012b). Enhanced performance of dye-sensitized solar cells using silane-modified TiO_2 electrodes. Journal of Power Sources, 216, 36–41.

Ren, Y., Cao, Y., Zhang, D., Zakeeruddin, S. M., Hagfeldt, A., Wang, P., & Grätzel, M. (2022). A blue photosensitizer realizing efficient and stable green solar cells via color tuning by electrolyte. Nature, 613(7942), 60–65.

Rühle, S., Greenshtein, M., Chen, S. G., Merson, A., Pizem, H., Sukenik, C. S., Cahen, D., & Zaban, A. (2005). Molecular adjustment of the electronic properties of nanoporous electrodes in dye-sensitized solar cells. Journal of Physical Chemistry B, 109(40), 18907–18913.

Sewvandi, G. A., Tao, Z., Kusunose, T., Tanaka, Y., Nakanishi, S., & Feng, Q. (2014). Modification of TiO_2 electrode with organic silane interposed layer for high-performance of dye-sensitized solar cells. ACS Applied Materials & Interfaces, 6(8), 5818–5826.

Sobuś, J., Kubicki, J., Burdziński, G., & Ziółek, M. (2018). Carboxyl and amino groups in the structure of dye-sensitized solar cells: A femtosecond to nanosecond study of electron injection dynamics. Angewandte Chemie International Edition, 57(5), 1307–1311.

Suresh, R., Pandiaraj, K., Sankaralingam, M., & Giribabu, L. (2018). Graphene–TiO_2 composite photoanode for dye-sensitized solar cells. Electrochimica Acta, 289, 591–598.

Tehare, K. K., Bhande, S. S., Mutkule, S. U., Stadler, F. J., Ao, J. P., Mane, R. S., & Liu, X. (2018). Low-temperature chemical synthesis of ruthenium oxide and its TiO_2 based dye-sensitized solar cells. Materials Research Bulletin, 97, 351–360.

Zaine, S. N. A., Mohamed, N. M., Khatani, M., & Shadid, A. A. (2020). Nanoparticle size effects on TiO_2-based dye-sensitized solar cells. Coatings, 10(3), 28